9-26-2023 12:30 PM

# Thermal and Fluid Evolution of the Clearwater West Impact-Generated Hydrothermal System, Quebec, and Associated Astrobiological Implications

Daliah R. Bibas, *Western University*

Supervisor: Osinski, Gordon, *The University of Western Ontario*
Co-Supervisor: Nigel, Blamey, *The University of Western Ontario*
A thesis submitted in partial fulfillment of the requirements for the Master of Science degree in Geology

# Abstract

Impact-generated hydrothermal systems result from interactions between a permeable substrate, an impact-generated heat source, and fluids (e.g., $H_2O$). A comprehensive understanding of the evolution of these terrestrial features has significant implications in the search for habitable environments on Mars, a focus in the emerging field of astrobiology. This thesis presents a detailed case study of the impact-generated hydrothermal alteration of impactites at the Clearwater West impact structure, Quebec, focusing on hydrothermally precipitated quartz vugs in crater-fill impact melt rocks. Sample analysis included optical microscopy, electron microprobe analysis, mass spectrometry, and fluid inclusion microthermometry. Results show three main quartz mineralization stages: 1) > 384°C, 2) 382 to 246°C, and 3) 243 to 120°C. Gas analysis indicated volatile sources were primarily atmospheric, with some mixing of local magmatic and crustal sources. This research provides insight into water preservation on Mars and the significance of impact-generated hydrothermal systems for extraterrestrial microbial life.

# Keywords

Clearwater West Lake impact structure, impact cratering, impact-generated hydrothermal systems, electron microprobe analysis (EMPA), cathodoluminescence, gas analysis, quadrupole mass spectrometry (QMS), fluid inclusion microthermometry, fluid evolution, thermal evolution, quartz vugs, quartz mineralization, analogue, hydrothermal alteration, Mars, astrobiology.

# Summary for Lay Audience

Hydrothermal systems that form in large impact craters (impact-generated hydrothermal systems), through a process involving heat and water, can produce conditions suitable for life. The required heat and rock fracture networks that allow for fluid flow are produced during the initial collision and the water is sourced from the surrounding area (e.g., groundwater, permafrost, lakes, oceans). As hot water circulates through the fractured rocks, many minerals begin to crystalize, trapping small amounts of local water and volatiles present. These pockets of fluids, known as fluid inclusions, are essentially small time-capsules of the conditions in which they formed. Fluid inclusions can therefore be used to study temperature, salinity, and volatile content of their parent fluid and assess the habitability of this environment for resilient microbes, such as thermophiles and hyperthermophiles. Investigating such environments on water-bearing rocky bodies, such as Mars, poses a significant challenge. Consequently, studying and using impact-generated hydrothermal systems on Earth as analogues for extraterrestrial surfaces is currently the only avenue for scientific investigation. This thesis provides a case study on the impact-generated hydrothermal system located in the 286-million-year-old Clearwater West impact crater, Quebec, Canada. This impact structure stands as one of the most well-preserved large complex impact structures on Earth. Samples of hydrothermal quartz vugs and associated fluid inclusions were analyzed to contribute to the understanding of: 1) the thermal and fluid evolution of impact-generated hydrothermal systems, 2) their implications for past Mars environments, and 3) their potential role in fostering habitable environments for life. This research provides insight into the preservation and characteristics of water on Mars and the significance of impact-generated hydrothermal systems for extraterrestrial microbial life. Quartz minerals from such systems can, and should, be used in our search for extinct, and perhaps extant, extraterrestrial life across the solar system.

# Co-Authorship Statement

Chapter 1 is an introduction to the thesis alongside a comprehensive literature review and was written by Daliah Raquel Bibas with comments and editing provided by Dr. Gordon Osinski and Dr. Nigel Blamey.

Chapter 2 is presented in manuscript format. Data collection, processing, and interpretation was performed by Daliah Raquel Bibas. Insights, comments, and editing were provided by Dr. Gordon Osinski and Dr. Nigel Blamey. Dr. Nigel Blamey provided training and guidance on mass spectrometry and fluid inclusion microthermometry data collection methods and subsequent interpretations. Samples were collected by Dr. Gordon Osinski and the 2014 Canadian-US-UK expedition team. This collaborative expedition was conducted as part of the Field Investigations to Enable Solar System Science Exploration (FINESSE) project, affiliated with NASA's Solar System Exploration Research Virtual Institute (SSERVI).

Chapter 3 is an overall discussion of the thesis and its conclusions. The chapter was written by Daliah Raquel Bibas, with comments and editing provided by Dr. Gordon Osinski and Dr. Nigel Blamey.

# Acknowledgments

I would like to thank my co-supervisors, Dr. Gordon “Oz” Osinski and Dr. Nigel Blamey for their guidance and support throughout the last 2 years of my graduate studies.

I would also like to thank Steven Wood, Liane Loiselle, Dr. Joshua Laughton for their help and training with the sample preparation, microscopes, and electron microprobe. Again, I would like to thank Dr. Nigel Blamey for his help and training with the residual-gas quadrupole mass spectrometry (QMS) and fluid inclusion microthermometry.

I am so grateful for all the friends I have made at Western University through graduate courses and seminars, lab groups, the Geology Graduate Society, the Western Space Graduate Council, and the Institute for Earth and Space Exploration. I would also like to give a special shoutout to Thomas Henley from Brock University for his help, guidance, and friendship over the last 2 years.

A big thank you to my parents, Shlomo and Heather, to my siblings, Elan and Tal, and to my rabbit, Lily. Your love and support is the reason I am where I am today.

# Table of Contents

# List of Tables

# List of Figures

# List of Appendices

# List of Acronyms

ASW – Air saturated water

BSE – Backscattered electron

CFS – Crush-fast scan

CL – Cathodoluminescence

EDS – Energy dispersive X-ray spectroscopy

EMPA – Electron microprobe analysis

EPMA – Earth and Planetary Material Analysis

ESA – European Space Agency

FINESSE – Field Investigations to Enable Solar System Science Exploration

NASA – National Aeronautics and Space Administration

PDF – Planar deformation features

QMS – Two quadrupole mass spectrometer

SE – Secondary electron

SSERVI – Solar System Exploration Research Virtual Institute

$T_f$ – Freezing temperature

$T_h$ – Homogenization temperature

$T_m$ – Ice-melting temperature

WDS – Wavelength dispersive X-ray spectroscopy

# Glossary

Alkalinophile – A microorganism that thrives in pH levels between 8.5 and 11.

Autotrophs – Microorganisms capable of producing their own nutritional organic substances from simple inorganic substances.

Chemolithotrophs – Microorganisms that obtain energy by oxidizing inorganic compounds, such as minerals or inorganic chemicals.

Endolithic habitat – A geological environment within rocks, minerals, or other solid substrates that provides a living space for microorganisms and other life forms.

Euhedral – Well-defined, fully formed crystal shape or structure of a mineral or crystal.

Fluid inclusion – Tiny pockets or cavities in minerals that contain a combination of fluids and gaseous or solid materials.

Growth zone – A specific area or layer within a mineral or rock where new material, typically mineral crystals, has formed or grown over time.

Heterotrophs – Organism that rely on consuming organic matter as their source of energy and carbon, as they cannot produce their own nutritional organic substances.

Impact-generated hydrothermal system – Geological system formed when a high-velocity impact generates intense heat and pressure that drives the circulation of hot fluids through that Earth's crust.

Impactite – A type of rock formed from the intense pressures, temperatures, and shockwaves resulting from hypervelocity impact events.

Homogenization – Refers to the process in fluid inclusion studies where all phases within an inclusion equilibrate to a uniform composition, typically involving the transition from a two-phase (liquid and gas) to a single-phase state.

Hydrothermal alteration – Process by which rocks are chemically and mineralogically modified due to interaction with hot, aqueous fluids.

Hyperthermophile – A microorganism that thrives in temperatures between 80 to 120°C.

Meteoric fluid – Water derived from atmospheric sources, such as rainfall or snow.

Neutrophile – A microorganism that thrives in pH levels between 6.5 to 7.5.

Photoautotrophs – Microorganisms that obtain energy from light and carbon dioxide via the process of photosynthesis.

Pseudotachylite – A type of fine-grained, dark-coloured, glassy rock occurring as veins that form through frictional melting and subsequent quenching of rocks during an earthquake, landslide, or impact event.

Quartz vug – A cavity or void in a rock that is lined or filled with quartz crystals.

Shock metamorphism – Alteration and deformation of rocks due to the sudden application of high-pressure and high-temperature conditions.

Subhedral – Crystal shape that displays some external faces characteristic of its crystal form but is not perfectly formed.

Suevite – A type of rock consisting partly of melted material, typically forming a breccia containing glass and crystal or lithic fragments, formed during an impact event.

Thermophile – A microorganism that thrives in temperatures between 45 to 80°C.

Volatiles – Substances or elements that have a tendency to vaporize or evaporate at relatively low temperatures, typically found in a gaseous or liquid state at Earth's surface conditions.

# Chapter 1

# 1 Literature Review and Thesis Introduction

## 1.1 Introduction

Impact events into target materials with abundant $H_2O$ (e.g., sea cover, groundwater, or permafrost/ice) have the ability to produce hydrothermal systems (Kirsimäe & Osinski, 2012; Osinski et al., 2013). Despite the initial disastrous effects caused by hypervelocity impacts, impact-generated hydrothermal systems can create transient conditions and habitats suitable for microbial life. These systems provide reactive surfaces where prebiotic chemistry can become concentrated (Cockell, 2006; Naumov, 2005; Pontefract et al., 2014), offering diverse ecological conditions for life during and long after their activity (Cockell et al., 2005; Cockell & Lee, 2002; Osinski et al., 2020). Due to their extensive occurrence across the solid surfaces of planets and moons within our solar system, impact craters are ideal candidates for the investigation of ancient water and potential life on Mars (Osinski et al., 2020; Osinski & Pierazzo, 2012).

There are three phases in the formation and evolution of impact craters: 1) the thermobaric phase, 2) the hydrothermal phase, and 3) the succession phase (Osinski et al., 2020). The thermobaric phase includes the initial contact and compression, excavation, and modification, while the hydrothermal phase includes the subsequent cooling of the crust and the circulation of liquid water. The longest-lasting phase, the succession phase, includes the gradual ecological change over time, shaped by the resulting crater surface expressions modified by erosion, subduction, and/or burying (Cockell & Lee, 2002). Although these geological processes alter terrestrial craters over time on Earth, investigating impact-generated hydrothermal systems on other planetary surfaces poses a significant challenge. Consequently, utilizing such systems found on Earth as analogues for extraterrestrial surfaces, such as Mars, is currently the only avenue for scientific investigation. However, with the advancement of the first Mars sample return missions, including the NASA and ESA collaborative sample return mission from Jezero Crater

expected to arrive back on Earth in 2033, our understanding of these processes may take a significant leap forward (Dirri et al., 2021; Meyer et al., 2022).

The primary objectives of this thesis are to contribute to the understanding of: 1) the formation and evolution of impact-generated hydrothermal systems, 2) their implications for past Mars environments, and 3) their potential role in fostering environments conducive to life. This thesis presents a case study on the impact-generated hydrothermal system developed within the Clearwater West Lake impact structure, located in northern Quebec, Canada. The impact structure is centered at 56°08′N; 74°18′W. This structure is approximately 36 km in diameter, and 286.2 ± 2.2 million years old (Schmieder et al., 2015). More specifically, this thesis characterizes the fluid and thermal evolution of the associated impact-generated hydrothermal system using optical microscopy, electron microprobe analysis (EMPA), mass spectrometry, and fluid inclusion microthermometry on surface samples collected in 2014.

## 1.2 Thermobaric Phase

The thermobaric phase represents the initial stage of high pressure and high temperature during impact crater formation (Osinski et al., 2020). This phase includes three stages: 1) contact and compression; 2) excavation; and 3) modification (Figure 1.1), and lasts between seconds to hours (Dence, 1968; Gault et al., 1968; Melosh, 1989). The impactor size and target material composition ultimately determine the course of the thermobaric phase (Kenkmann et al., 2014). Hypervelocity impact craters are formed when an asteroidal or cometary projectile of a size significant enough to traverse the atmosphere with minimal to no deceleration and impact on the planetary surface happens at or near its original cosmic velocity (French, 1998). Such hypervelocity impacts trigger the propagation of a powerful shock wave, leading to the formation of distinctive shock metamorphism features in the target material (Dence, 1968; Melosh, 1989). It is during this phase that the hydrosphere or cryosphere is disrupted, and significant changes occur to the surface area through fracturing, shock metamorphism, and melting (Osinski et al., 2020). The minimum velocity required to create a hypervelocity impact crater depends on the density of the impacted planetary body. On Earth, a minimum velocity of 11.2 km/s is

necessary, and to date, a total of 188 hypervelocity impact craters have been documented (Melosh, 1989; Osinski et al., 2022).

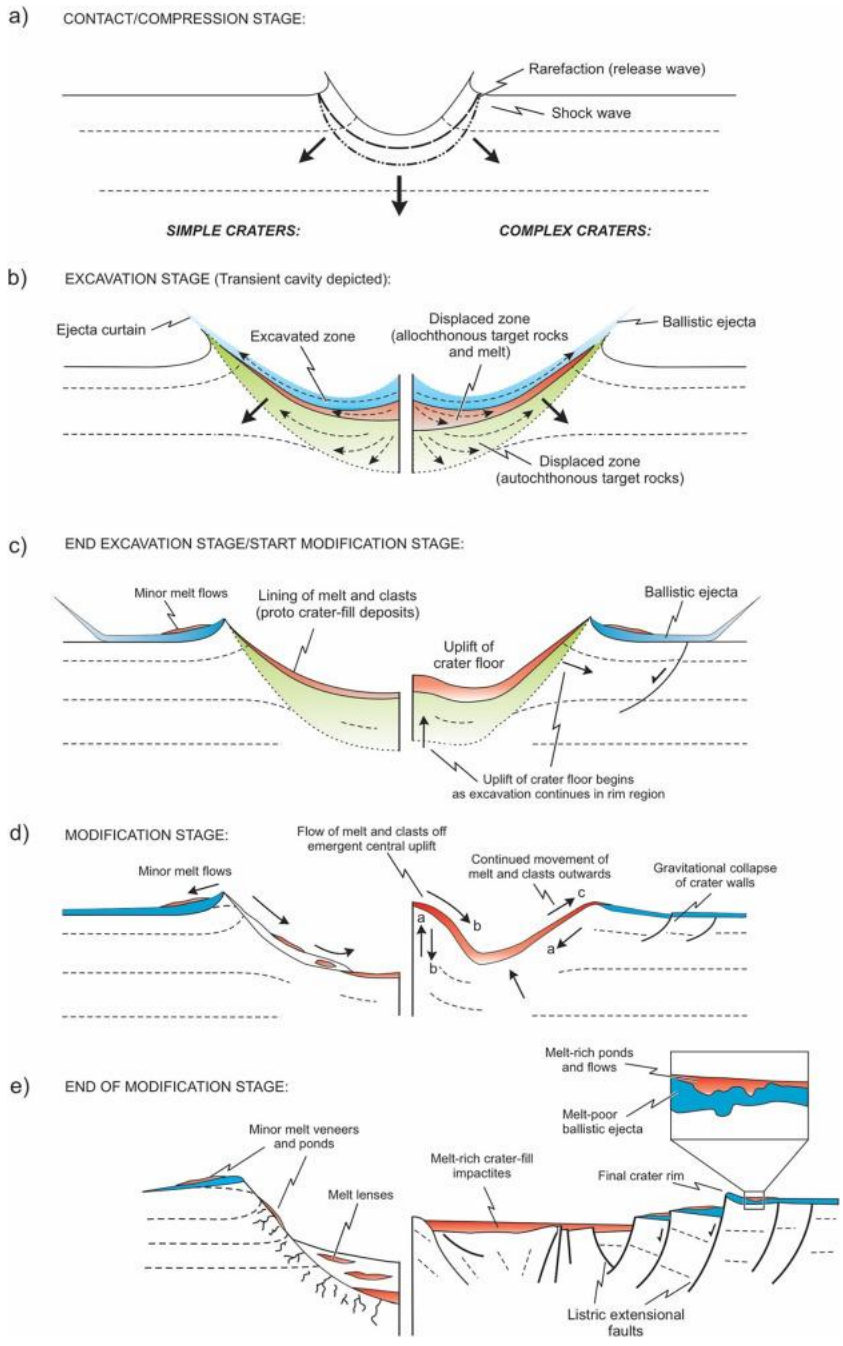


**Figure 1.1 Model illustration of the stages in the formation of simple (left) and complex (right) hypervelocity impact craters into terrestrial (non-marine) environments. a) Contact/compression stage. b) Excavation stage. c, d, and e) Modification stage (Osinski et al., 2022).**

### 1.2.1 Contact and Compression

This stage involves the initial impact of the projectile (either an asteroid or comet) into the target surface and the compression of the target material (Figure 1.1a) (Osinski et al., 2022). This process converts the kinetic energy of the projectile into internal and kinetic energies in both the projectile and target material, and produces pressures exceeding 100 GPa (Kenkmann et al., 2014; Melosh, 1989; Shoemaker, 1960). The conversion of energy generates shock waves that begin at the centre of the impact, then propagate outwards into the nearby crust (while decreasing shock pressures over distances). The compressing and acceleration of the engulfed material results in irreversible deformation of the target material, known as shock metamorphism (Abramov & Kring, 2005; French, 1998; French & Koeberl, 2010; Kenkmann et al., 2014). The shock amplitude decays as the shock distance increases and the degree of alteration is material-dependent (i.e., shock wave magnitudes decay faster in porous rocks than in low-porosity rocks) (Holsapple, 1987; Kenkmann et al., 2014). The passage of shock waves and high pressures through the planetary crust increases the target material temperature (internal energy and entropy) and residual particle velocity, leading to shock metamorphism in the target rocks, as well as melting and/or vaporization of a substantial portion or the entirety of the projectile (French, 1998; French & Koeberl, 2010; Melosh, 1989). The duration of the contact and compression stage depends on the projectile's size and the shock wave's speed, but typically lasts no more than a few seconds, even for the largest events (Kenkmann et al., 2014; Osinski et al., 2020). This stage is completed when the projectile has completely melted and/or vaporized (Melosh, 1989).

### 1.2.2 Excavation

The excavation stage involves the expansion and dissipation of the shock wave and the enlargement of the crater cavity via excavation and displacement of target materials (Figure 1.1b) (Osinski et al., 2022). The initial compressed and accelerated material does not decelerate completely and a residual velocity remains, playing a crucial role in the excavation of the target material (Kenkmann et al., 2014; Melosh, 1989). The interaction between the downward-directed rarefaction waves and the outward-directed shock waves causes a reduced pressure gradient towards the surface, releasing the compressed material

from its high-pressure state, setting the target material into motion, and producing a parabolic-shaped cavity opening (Kenkmann et al., 2014; Osinski et al., 2020). Deeper portions of the cavity material are moved downward into the ground and do not exit the crater, while the upper one-third to one-half of the material is deposited as allochthonous ejecta during the excavation process (Melosh, 1989; Osinski et al., 2022; Osinski & Pierazzo, 2012). The continuous ejecta blanket can stretch to 1 to 3 times the radius of the crater and the discontinuous deposits can stretch up to 5 times the radius of the crater, allowing for the distribution of distal ejecta deposits over thousands of kilometers (Osinski et al., 2020). At the end of the excavation stage, the unstable transient cavity is lined with an ejecta blanket consisting of a mix of melt and clastic material with varying levels of shock effects (Osinski et al., 2011). This material, called impactites, ranges from melt-free to glass-bearing breccias to massive kilometer-thick consolidated sheets of igneous-textured impact melt rocks (Figure 1.2) (Osinski et al., 2018).

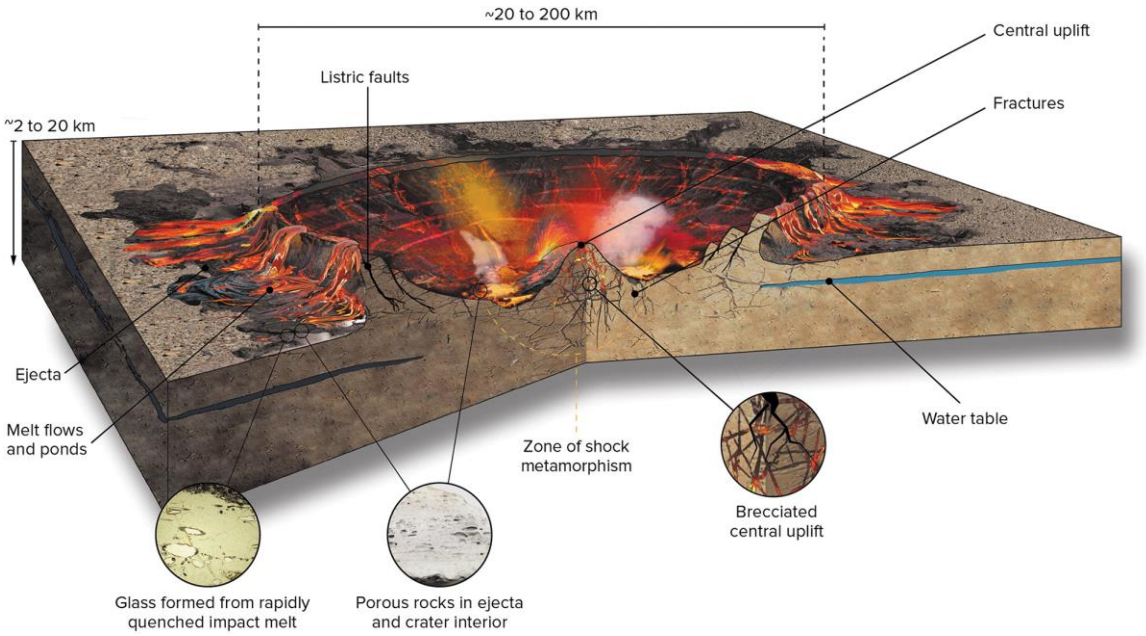


**Figure 1.2 Visual representation of a typical complex impact crater during the final stage of the thermobaric phase. Melt flows and pools occur in scattered areas on top of ballistic impact eject deposits around the crater. Rocks within the crater exhibit significant fracturing and undergo shock metamorphism, with shock pressures intensifying towards the center (Osinski et al., 2020).**

### 1.2.3 Modification

The modification stage entails the modification of the transient cavity and its subsequent collapse (Figure 1.1c, d, e). This stage begins when the excavation flow stops, and the transient cavity widens. Gravity is the main force that drives the collapse of the transient cavity (Kenkmann et al., 2014). Depending on the shape of the final crater, it can be defined as a simple, complex, or transitional morphological structure (Figure 1.1e) (Osinski et al., 2011). A simple crater is formed after an impact event with a relatively small-scale projectile (less than 2-4 km diameter on Earth, around 10 km on Mars, and up to approximately 20 km on the Moon) and comprises a relatively deep crater fill (Figure 1.3a) (Osinski et al., 2020). The transient cavity undergoes minimal modification, including cavity wall inward collapse and slumping, resulting in the formation of a simple crater with a bowl-like shape encircled by minor melt flows and ejecta (Figure 1.1e) (Osinski & Pierazzo, 2012). The rim of the crater is uplifted and overturned, with the resulting final diameter closely resembling that of the transient cavity.

When the diameter of the transient cavity surpasses a certain threshold (on Earth, this transition is approximately 2.8 km for sedimentary targets and 3.2 km for crystalline targets), it gives rise to the formation of a complex crater (Osinski et al., 2022). This is attributed to the increased instability of the depression, resulting in more extensive modifications (Kenkmann et al., 2014). Heated material is brought up closer to the surface as the material under the central region of the crater floor is uplifted, and terraced rims are formed around a shallow depth-to-diameter crater (Figure 1.3b) (Abramov & Kring, 2005). The morphology of the uplifted rocks in complex craters can be categorized into a central peak, peak-ring craters, and multi-ring basins, with increasing crater size, respectively (Kenkmann et al., 2014; Osinski et al., 2020).

Transitional craters emerge when their diameters align closely with the transient cavity diameter threshold of the planetary body of which the impact occurs. These craters share similarities with complex craters, featuring a flat crater floor and the potential presence of terraces, but they lack a central uplift (Osinski et al., 2022; Osinski & Pierazzo, 2012). On Earth, a total of 43 simple, 3 transitional, and 143 complex hypervelocity impact craters have been documented (Osinski et al., 2022). The modification stage is complete

when the target's significant motion has stopped. The duration of this stage depends on the energy of the impact, gravity of the target body, and strength of the target material (Melosh & Ivanov, 1999). The timescale increases with higher impact energy, less gravity, and lower target strength (Kenkmann et al., 2014).

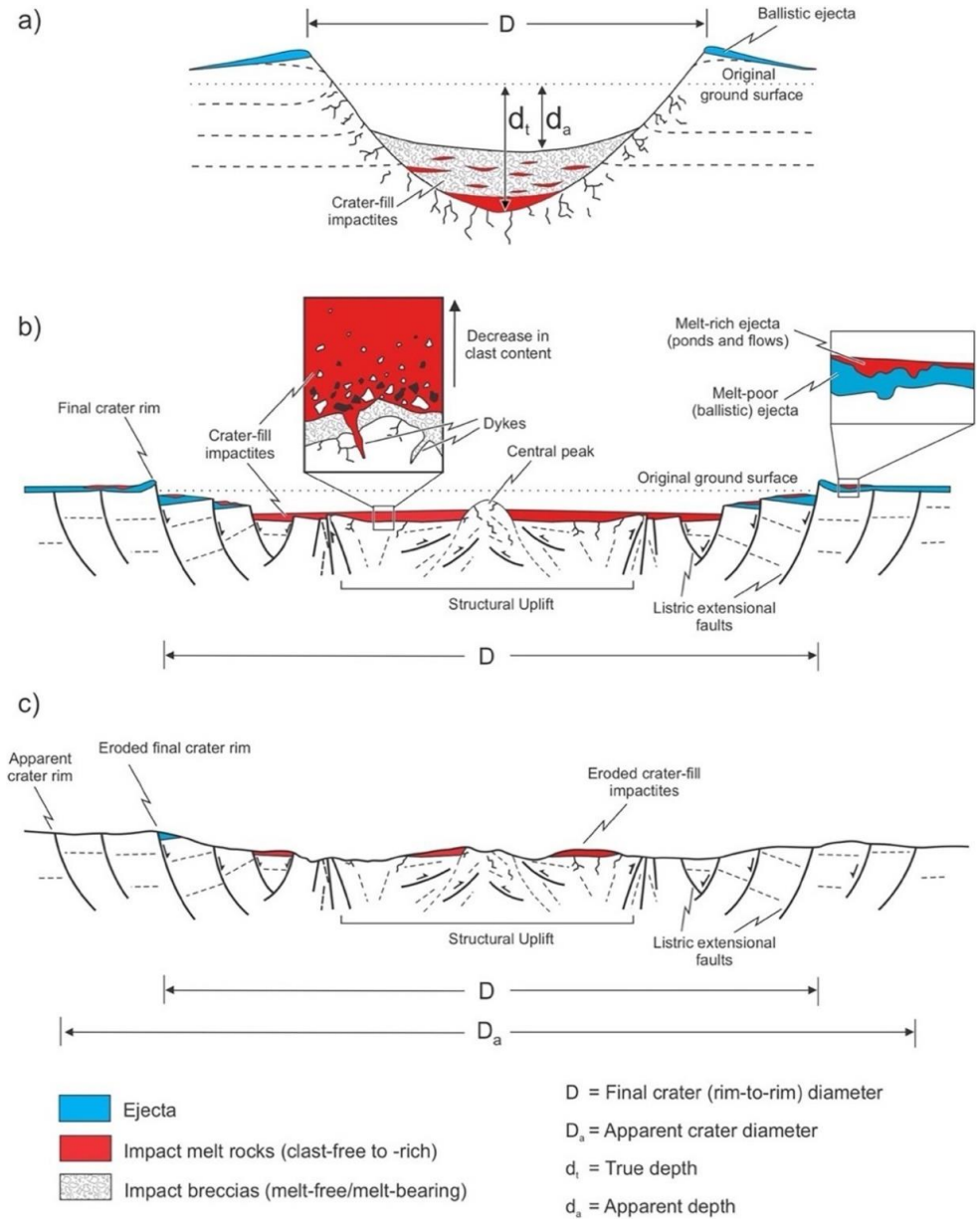


**Figure 1.3 Model illustration of cross sections of simple and complex hypervelocity impact craters formed in crystalline target rocks (continental and non-marine setting). a) Simple impact crater. b) Complex impact structure in pristine condition. c) Complex crater after erosion has occurred (Osinski et al., 2011).**

## 1.3 Hydrothermal Phase

Hydrothermal systems involve the redistribution of mass and energy via thermal, chemical, and mechanical processes driven by molecular diffusion and the circulation of $H_2O$ fluids (Norton, 1984). The kinetic energy generated by the impact produces a difference in entropy between the heat source and its cooler surroundings, creating a thermal driver for the movement of water, steam, and other volatiles in the target material (Abramov & Kring, 2005). The formation of a hydrothermal system is contingent upon several factors: there must be sufficient heat generated through uplifted geothermal gradients and/or impact melt-bearing rocks, a sustained permeability (i.e., rock fracturing) to facilitate fluid circulation, and an adequate supply of volatiles such as liquid water, ice, or water produced by the dehydration and degassing of minerals (Abramov & Kring, 2004, 2007; Naumov, 2005; Osinski et al., 2013; Parnell et al., 2010). Most impact craters on Earth over a few km in diameter have generated hydrothermal systems (Kirsimäe & Osinski, 2012; Naumov, 2005; Osinski, Tornabene, et al., 2012; Osinski et al., 2020). Out of the 188 hypervelocity impact craters documented on Earth, hydrothermal systems have been identified in 70 of them (Naumov, 2002, 2005; Osinski et al., 2013). However, due to the limited preservation and accessibility of impact-generated hydrothermal systems on Earth, their detailed study remains relatively scarce.

The physical, chemical, and even biological characteristics of a hypervelocity impact crater are shaped by the presence of a hydrothermal system. The structure of the impact-generated hydrothermal system and the extent of hydrothermal alteration is ultimately determined by the thermobaric phase (Osinski et al., 2020). The formation of these systems in small-to-medium and large complex impact structures differ in their structural formation, cooling records, and resulting hydrothermal system complexities (Kirsimäe & Osinski, 2012). Six settings within and around hypervelocity impact craters have the potential for hydrothermal system development including crater-fill impactites, the interior and margins of central uplifts, proximal ejecta deposits, the crater rim, and post-impact crater lake sediments (Figure 1.4) (Osinski et al., 2013). Once the impact structure

cools down—which depends largely upon size of the impact and the surrounding geological characteristics—life can colonize the area (Osinski et al., 2020).

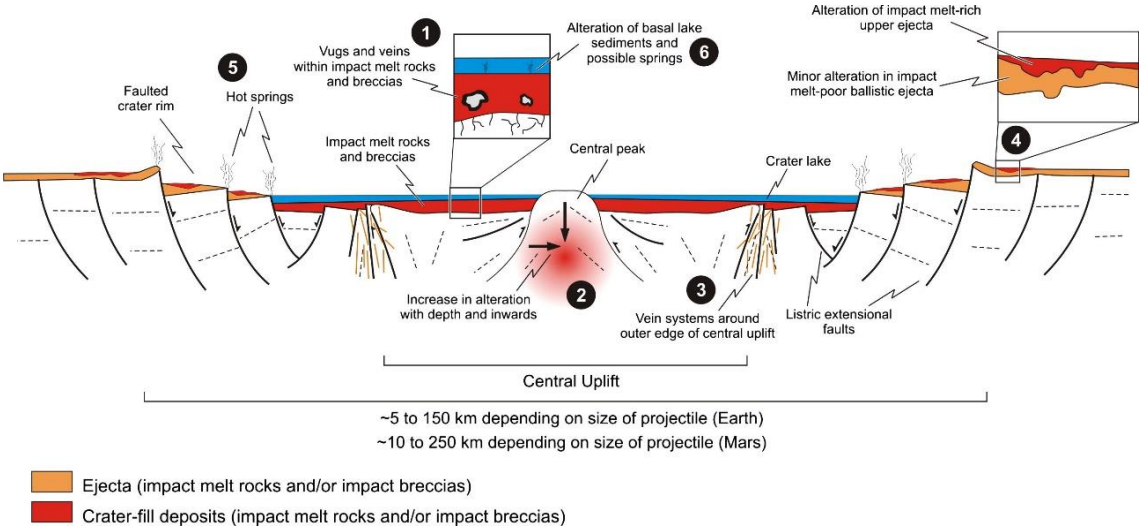


**Figure 1.4 Model illustration of impact-generated hydrothermal deposits found at complex impact craters on Earth and Mars (Osinski et al., 2013).**

### 1.3.1 Heat Sources

Impact melt-bearing impactites are the major heat source within the crater and are what primarily drives the impact-generated hydrothermal activity, as well as the central uplift due to the energy from the shock wave and the high geothermal gradient (Kirsimäe & Osinski, 2012; Osinski et al., 2005, 2013; Osinski & Pierazzo, 2012). In small to mid-sized impact craters, impact melt rocks and impact melt-bearing breccias are the main driver of hydrothermal systems, while in larger impact craters, the increased heat input from the uplifted geothermal gradient within the central uplift is the primary driver (Osinski et al., 2020). Heat transfer during impact cooling occurs through conductive and radiative processes for large complex craters with massive peak-ring structures or multi-ring basins due to the large initial impermeable hot melt sheet within the crater (Kirsimäe & Osinski, 2012). Within smaller structures, a simple convective system typically arises within the most heated central part of the crater (Abramov & Kring, 2007). There are several different heat sources in large impact structures that are accessible at varying time periods. Initially, heat is supplied by melt-bearing breccias above the central melt sheet in

the annular trough, the fractured modification zone, and often the peak-ring area, while after cooling and solidification of the melt sheet, heat is supplied mainly by the central uplift area (Abramov & Kring, 2007).

Although the duration of the thermobaric phase typically only lasts a few minutes, impact modelling and crater dating studies show that the thermal effects of impact events carry on over a long duration (Kenkmann et al., 2014; Kirsimäe & Osinski, 2012). Heat generated from an impact event can melt surface and subsurface ice deposits, which can then interact with hot impact-generated and impact-altered rocks to generate transient hydrothermal systems (Osinski et al., 2020). Temperatures within these systems can range from approximately 500°C during the early stages under magmatic-hydrothermal conditions, to as low as 50°C during the later cooling stages (Naumov, 2005; Pirajno, 2009). An impact event can create several long-lasting heat sources permitting hydrothermal systems to thrive for long periods of time (Abramov & Kring, 2005; Osinski et al., 2020). The duration of active impact-generated hydrothermal systems varies depending on the size of the impactor and subsequent crater, and the properties of the target rock and associated mechanisms of heat transport (Abramov & Kring, 2004; Kirsimäe & Osinski, 2012; Osinski et al., 2020; Schmieder & Jourdan, 2013). These systems can persist for a few thousand years for craters around 5 km in diameter, hundreds of thousands of years for craters ranging from 20-30 km in diameter, and up to 6 million years for craters with diameters exceeding 200 km (Abramov & Kring, 2004; Jõeleht et al., 2005; Pickersgill et al., 2019; Schmieder & Jourdan, 2013). Heat takes much longer to dissipate in more enormous impacts, while temperatures decrease faster for smaller impacts. This is because larger impacts produce higher temperatures over a larger surface area and rapid convective heat transport only takes place near the surface, while slower conductive heat transport is more dominant in the deeper parts of the crater due to the presence of impermeable rocks (Kirsimäe & Osinski, 2012).

### 1.3.2 Porosity and Permeability

Porosity and permeability characterize the flow of fluid through interconnected fracture networks, an environment required for the development of impact-generated hydrothermal systems (Norton, 1984; Parnell et al., 2010). As the level of shock

intensifies (i.e., as pressure increases), there is a notable increase in porosity and permeability of the target material (Singleton et al., 2011). During the formation of a crater, fragmentation and displacement of target rocks results in increased porosity in the allochthonous impact melt-bearing and lithic breccias (Pilkington & Grieve, 1992). Beneath these deposits, shock-induced fracturing in the autochthonous (in-situ) target material results in increased porosity, therefore producing lower densities than the undisturbed regional rocks. Fracturing near the target rock surface also occurs, extending beyond the crater rim by a distance equivalent to one crater diameter (Pilkington & Grieve, 1992). In complex craters with massive peak-ring structure or multi-ring basins, hydrothermal circulation develops initially in the annular trough around the central uplift and vents through faults in the modification zone within the basin (Abramov & Kring, 2004; Osinski et al., 2001). Immediately after impact, heat dissipation in complex structures is primarily influenced by the low permeability of heated rock and melt because impermeable material can only release heat through conduction. In smaller impact structures, the lifetime of convective systems and the activation of hydrothermal circulation are primarily contingent on the permeability of the area (Kirsimäe & Osinski, 2012; Osinski et al., 2020).

### 1.3.3 Fluid Sources

A fundamental determinant of the magnitude of impact-generated hydrothermal processes is the target region’s water availability (Naumov, 2005). The fluid reservoirs sustaining hydrothermal circulation commonly comprise a combination of local, accessible sources blended with basinal brines (Naumov, 2005; Osinski et al., 2013). Meteoric water acts as the primary source for hydrothermal fluid for continental impacts, while seawater serves as the primary source for shallow marine impacts. Throughout the duration of the system, the chemical composition of the fluids evolves and undergoes several changes (Naumov, 2005). In hydrothermal systems dominated by meteoric water, the initial chemistry of the fluid tends to be undersaturated in silicon and low in pH, resulting in H+ metasomatism (chemical alteration of the contacting rocks) (Naumov, 2005; Osinski et al., 2013; Pirajno, 2009). As fluid-rock interactions progress, the composition shifts towards near-neutral or alkaline conditions. In systems dominated by

seawater or basinal brines, the initial chemistry of the fluid tends to be saline and near neutral or alkaline (Simpson, 2020). These fluids can contain high concentrations of calcium, magnesium, and/or sulphate, which can influence the intensity of hydrothermal alteration (Naumov, 2005).

### 1.3.4 Mineral Alteration

The presence of impact-generated hydrothermal activity is evident through the occurrences of secondary mineral assemblages, chemical alterations of local rocks, and the presence of fluid inclusions within hydrothermal mineral phases (Naumov, 2005; Osinski et al., 2013). The fluid sources and the composition of rocks within the target material primarily govern the types of secondary mineral assemblages that can be produced within a specific impact crater (Naumov, 2005). Commonly encountered hydrothermally-altered minerals in terrestrial craters include quartz, calcite, pyrite, cristobalite, smectites, chlorites, and zeolites (Naumov, 2002; Osinski et al., 2013; Pirajno, 2009). The sequence of such secondary mineralization follows a specific order: silica minerals (e.g., quartz) are the first to form, followed by clay minerals (e.g., smectite), then zeolites (e.g., mordenite) and carbonates (e.g., calcite) (Naumov, 2005). Mineralization of melt rocks and melt-bearing breccias occurs predominantly within porous regions of the target material and brings about a range of features, from discrete cavity and fracture fillings (i.e., veins, vugs, and amygdules) to extensive integration within the target material (i.e., replacing other minerals) (Osinski et al., 2013, 2020). These features can be distributed throughout shocked, faulted, and fractured rocks beneath the crater (authigenic breccias), at the rim of the crater, within the central uplift and its outer margin, within layers of impact-melt rocks and lithic breccias filling the crater, in sediment deposits of crater lakes, and in impact ejecta deposits outside the crater (Naumov, 2005; Osinski et al., 2013, 2020).

As depth increases and distance to the crater center decreases (resulting in higher temperatures), there is an increase in intensity of hydrothermal alteration (Naumov, 2002). Hydrothermal alteration can be further amplified by the presence of glasses and highly shocked materials as they are more susceptible to alteration, as well as the existence of an overlying crater lake (Osinski et al., 2013, 2020). The highest amount of

alteration occurs in craters with impact melt rocks dominated by suevites, shocked polymict breccia consisting partly of melted material, glass, and crystal or lithic fragments (Osinski et al., 2020). In such craters, secondary minerals can account for up to 10-25% of the top portion of the authigenic breccias and the overlying impact breccias and suevites (Naumov, 2005).

## 1.4 Succession Phase

Succession refers to the gradual process of ecological colonization and transformation that occurs in a particular area over time (Cockell & Lee, 2002). The succession of impact-generated hydrothermal systems is driven by factors such as temperature, chemical composition, availability of nutrients, and interactions between different organisms (Cockell & Lee, 2002; Osinski et al., 2020; Versh et al., 2006). Geological processes, such as tectonic activity, erosion, deposition, and weathering, can degrade, bury, or completely remodel the resulting crater, also influencing the process of succession (Cockell & Lee, 2002). This is the longest phase in the formation and evolution of impact craters and can last between 100,000 to millions of years (Figure 1.5) since nutrients and habitats for life can be provided by hydrothermally altered and precipitated rocks for an extended period of time (Jébrak, 2015; Osinski et al., 2020; Osinski, Grieve, et al., 2012). In addition, the shock, heat, and pressure from the thermobaric phase produce glass, porous rocks, and fractured rocks, which can also be used as habitats once cooled (Cockell et al., 2003, 2005; Osinski et al., 2020).

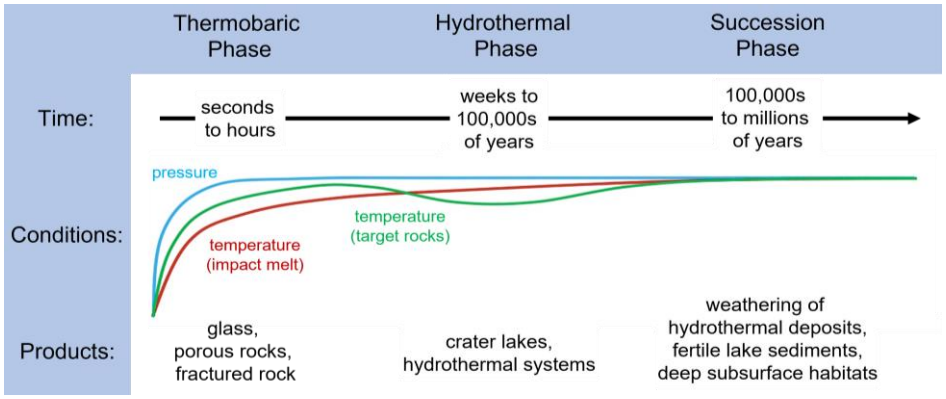


**Figure 1.5 Changing pressures and temperatures of an impact crater, showcasing various products formed during each phase (modified from Osinski et al., 2020).**

### 1.4.1 Primary succession

Hypervelocity impact events cause the formation of primary succession habitats, the biological colonization of a barren environment completely devoid of life (Cockell & Lee, 2002). Initially, temperatures are too high to foster life, but after the dissipation of the heat generated by the impact, surface temperatures in the crater gradually return to their pre-impact levels, marking the start of primary succession. At this stage, ecosystems can establish themselves on various substrates associated with the impact-generated hydrothermal system and this process continues until an ecologically stable environment is reached (Cockell & Lee, 2002; Osinski et al., 2020). The first organisms to populate a cooling system are various autotrophic thermophiles and hyperthermophiles (extremophilic microorganisms that have optimum growth temperatures between 45-80°C and 80-120°C, respectively) (Cockell, 2006; Cockell et al., 2005; Merino et al., 2019; Stetter, 2007; Versh et al., 2006; Wang et al., 2015). The growth and expansion of microbial communities is often enhanced by the persistent heat resulting from the impact event and hydrothermal circulation (Cockell & Lee, 2002). Elevated temperatures typically coincide with neutral to alkaline pH levels, which are favourable for neutrophiles and alkalinophiles (microorganisms that thrive between pHs of 6.5-7.5 and 8.5-11, respectively), however, localized areas with acidic conditions is also possible (Cockell, 2006; Naumov, 2005).

Hydrothermal habitats, made of hydrothermally altered and precipitated rocks, can form in six different locations in complex impact craters: 1) crater-fill impact melt rocks and melt-bearing breccias; 2) inside of central uplifts; 3) central uplift outer edges; 4) crater rim; 5) impact ejecta deposits; and 6) post-impact crater lake sediments (Osinski et al., 2013). Impact craters may periodically host lakes over geological timescales, offering relatively stable habitats as long as the topographic expression of the crater is preserved (Figure 1.6) (Osinski et al., 2013, 2020). Furthermore, glasses and highly shocked materials formed during the thermobaric phase also represent some of the major habitats (Fig. 1.6) colonized by microbial life in impact craters on Earth due to the presence of mobilized essential nutrients (Cockell & Lee, 2002; Osinski et al., 2020; Pontefract et al., 2014). Near-surface habitats with sufficient porosity and light transmission can be

colonized by photoautotrophs, heterotrophs, and chemolithotrophs, while endolithic habitats, such as impact-shocked rocks, subsurface fractures, and deep hydrothermal pipes, will only be colonized by heterotrophs and chemolithotrophs (Cockell, 2006; Cockell et al., 2005; Cockell & Lee, 2002). Endolithic habitats act as nutrient reservoirs in environments with limited resources, evidenced by the domination of heterotrophic bacteria in shocked crystalline lithologies (Pontefract et al., 2016).

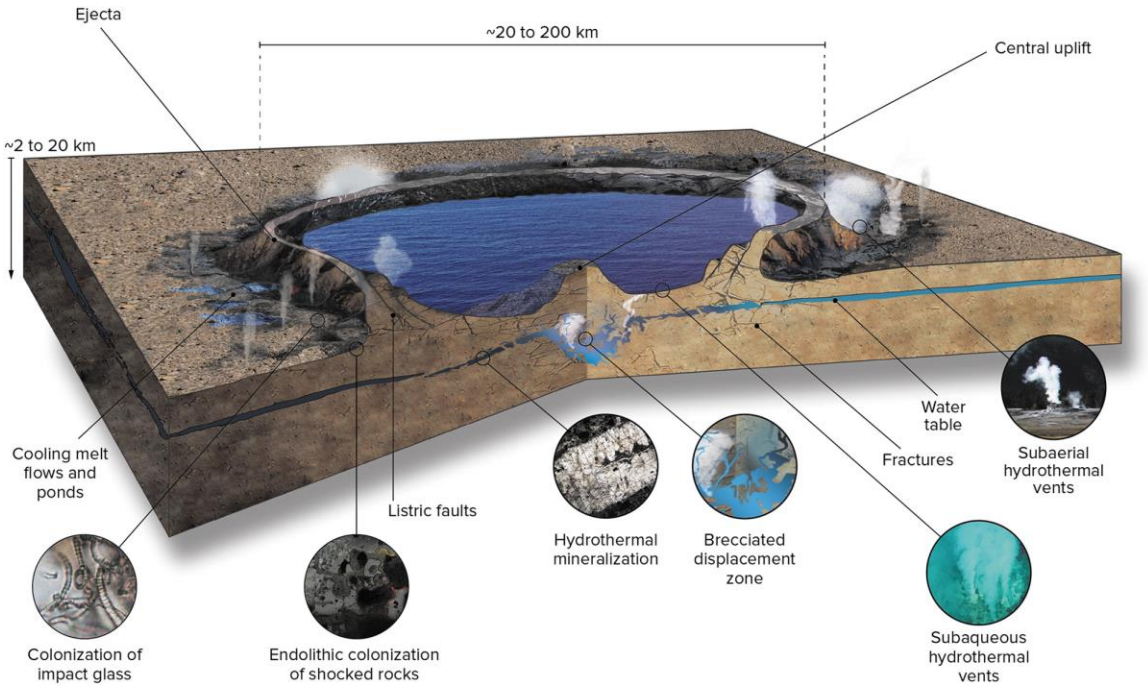


**Figure 1.6 Visual representation of a typical complex impact crater during the hydrothermal phase. Under favourable conditions, the thermobaric phase can give rise to a hydrothermal phase which can foster the emergence of various habitats within the crater, including a crater lake (Osinski et al., 2020).**

## 1.4.2 Ecological assimilation

Ecological assimilation represents the point at which the ecological characteristics of the impact crater site blend with those of the surrounding biome, resulting in a loss of ecological distinctiveness as the geological features gradually diminish (Cockell et al., 2012; Cockell & Lee, 2002). The erosion, subduction, and burying of craters over time, mostly driven by plate tectonics and biotic processes on Earth, make the site's surface

geology unrecognizable from the surrounding environment (Osinski et al., 2020). This thriving environment can now support higher trophic levels, such as plants and animals, because of its high primary productivity (Cockell & Lee, 2002). Approximately 50% of terrestrial impact structures have undergone assimilation, while the remaining 50% contain a distinct climax ecosystem that distinguishes them from the surrounding biota. Ecological assimilation is likely to occur more rapidly for impacts in shallow aquatic environments (marine or freshwater) compared to continental impacts (Cockell & Lee, 2002). In aquatic environment impacts, the cavity is partially or completely filled by water and sediment from the surrounding environment, leading to a relatively stable benthic habitat over the local impact breccia where aquatic organisms can quickly establish themselves. In cases where craters do not contain lakes, assimilation occurs when the structure is eroded or infilled to a point where the depression no longer exhibits distinct vegetational differences (Cockell & Lee, 2002). If a crater lake forms and the rim is breached, the lake may merge with external water bodies, resulting in the loss of its biological isolation. However, sometimes geological characteristics unique to the impact structure may still contribute to the specific characteristics of the lake, even if it is connected to surrounding water bodies (Cockell & Lee, 2002).

## 1.5 Clearwater West Lake Impact Structure

Situated in northern Quebec, Canada, Clearwater West Lake impact structure is a complex crater with a diameter of approximately 36 km, centered at 56°08′N 74°18′W, around 125 km East of Hudson Bay (Figure 1.7) (Dence et al., 1965; Simonds et al., 1978). The structure was originally thought to have a volcanic origin based on observations of “red breccia” and “grey dacite” (Krank & Sinclair, 1963); however, evidence supporting an impact-related origin surfaced around the same time, including shock-generated mineral phases, shatter cones, allochthonous breccias, and thin veinlets of melt rock (Beals et al., 1956; Dence, 1964; Dence et al., 1965). Subsequent petrographic and chemical examinations of impact and target lithologies, alongside field geology and structural relations analysis, highlighting impact-induced shock metamorphism, reinforced the impact origin hypothesis (Bunch, 1968; McIntyre, 1968; Phinney et al., 1978; Robertson et al., 1968; Simonds et al., 1978).

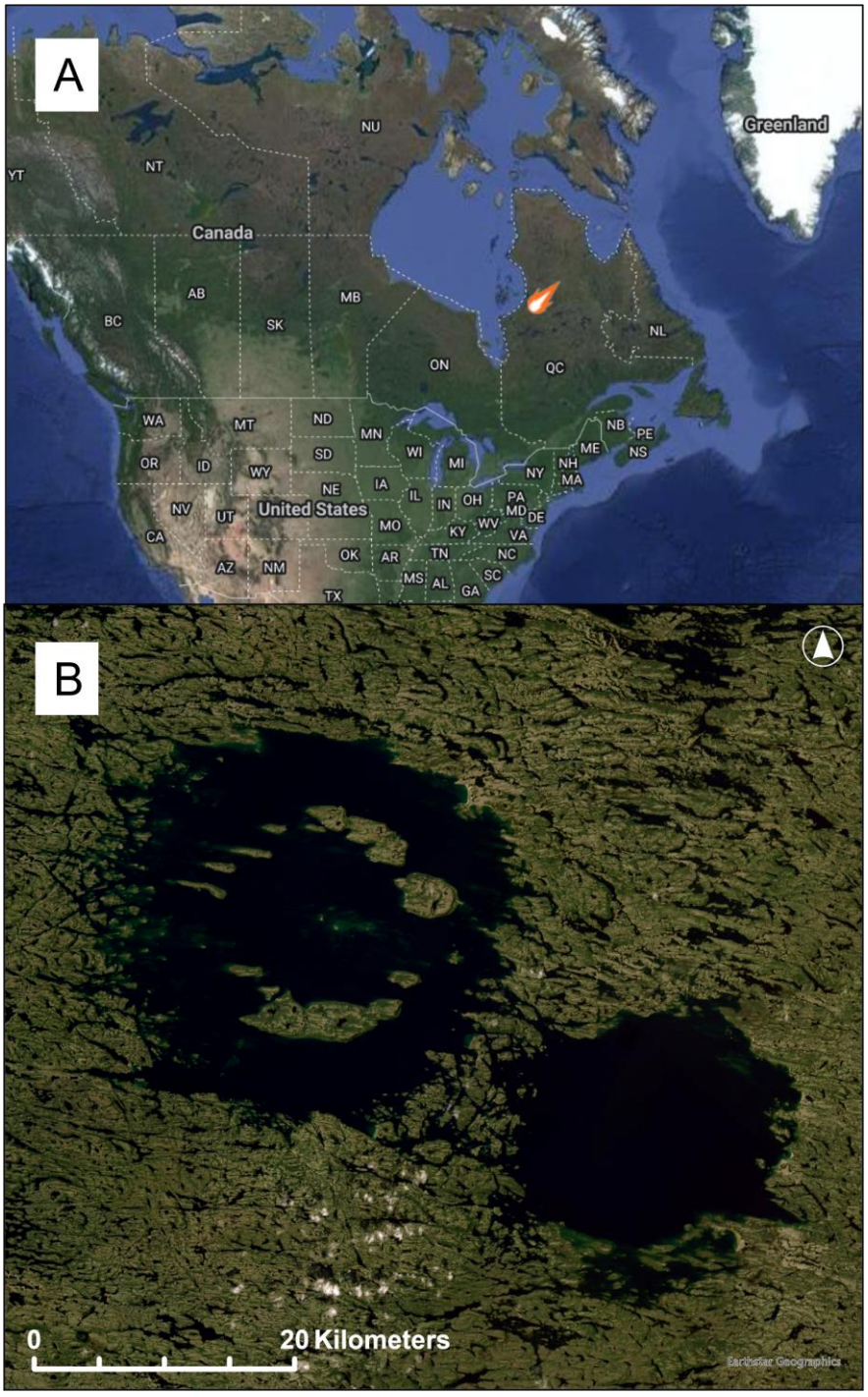


**Figure 1.7 Regional geographic context of Clearwater West impact structure. A) Location of Clearwater West impact structure, depicted by the fireball (Source: Impact Earth Database). B) Satellite image of both the East and West Clearwater lakes (Source: Earthstar Geographics SIO).**

The Clearwater West impact structure was initially believed to be the result of a binary impact event due to its proximity to the Clearwater East impact structure (Figure 1.7B), which lies only 30 km away from each crater centre (Dence et al., 1965). However, recent $^{40}Ar/^{39}Ar$ dating of melt rocks revealed that the Clearwater West impact structure formed during the Early Permian, approximately 286 ± 2.2 million years ago, while the older Clearwater East impact structure dates back to the Middle Ordovician, around 460-470 million years ago (Schmieder et al., 2015). These findings, together with paleographic reconstructions, confirm that the Clearwater West impact structure formed within the single continent of Pangea (Figure 1.8).

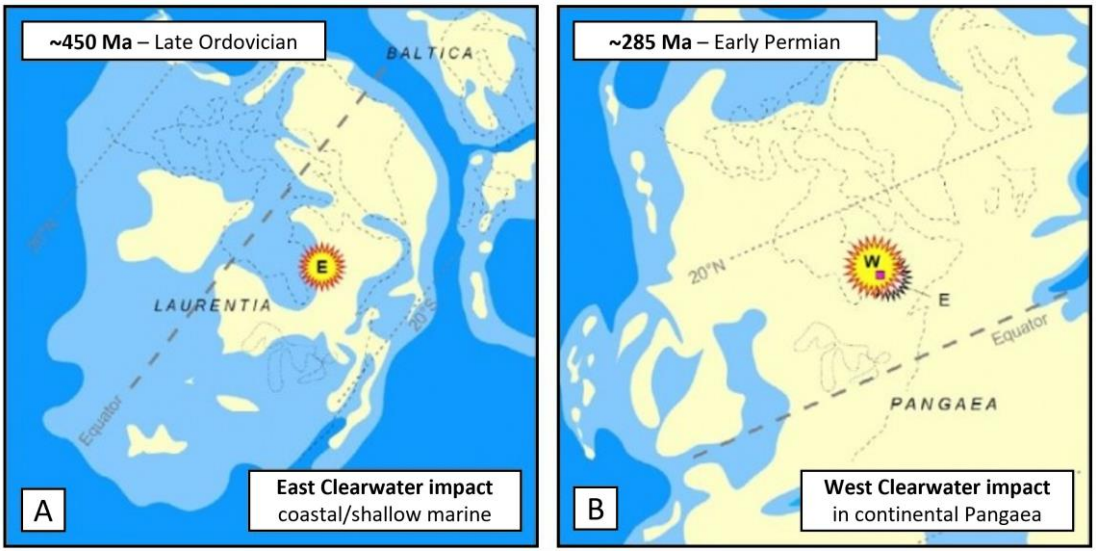


**Figure 1.8 North America (Laurentia) paleogeographic reconstructions. A) Clearwater East impact likely occurred under near-coastal to shallow-marine conditions. B) Clearwater West impact likely occurred in continental Pangaea (modified from Schmieder et al., 2015).**

The Clearwater East impact structure remains relatively understudied, due to its submerged features in the overlying lake and limited surface exposure. However, the Clearwater West impact structure boasts a higher degree of preservation, characterized by a ring of islands around 16 km in diameter within the roughly 30 km-diameter lake (Osinski et al., 2015). The islands form part of the impact structure's peak ring, and a cluster of small islands, less than 100 m across, situated in the center, constitute the

central peak (Figure 1.7B) (Grieve, 2006). The structure comprises two troughs, one with depths exceeding 100 m between the shoreline and the peak ring, and the other with a maximum depth of 50 m between the peak ring and central peak. The hypervelocity impact that formed the Clearwater West impact structure occurred in the northern section of the Bienville Domain within the Minto Subprovince of the Canadian Shield's Superior Province (Simard et al., 2004, 2008). The area is characterized by local Archean plutonic rocks, primarily granodiorite, quartz monzonite, granite, and amphibolite, intruded by Proterozoic age diabase dikes (Bostock, 1969; Schmieder et al., 2015). The impact melt contains limestone outcrops from the Ordovician age, likely around 130 m thick at the time of impact (Hische, 1995; Simonds et al., 1978).

### 1.5.1 Clearwater West Impact-Generated Hydrothermal System

Prior research has documented hydrothermal alteration at the Clearwater West impact structure, evidenced by the replacement of glasses and pyroxenes with various clays and the presence of abundant hematite within the impact breccias and impact melt rocks (Bostock, 1969). Clays identified within the melt-bearing breccias were classified as magnesium-rich, calcium-, aluminium-, and potassium-poor saponites, resulting from the alteration of sub-micron glass clasts (Allen et al., 1982; Phinney et al., 1978). Eberl et al., (1978) demonstrated that these varieties of clays have the potential to undergo mixed layering with talc as temperatures approach around 500°C, thus offering an estimate of the upper limit for the formation temperature of these clays. Moreover, four types of micrometer-sized hematite, associated with hydrothermal alteration, were observed in the matrix of fine-grained impact melt rocks, contributing to the distinct reddish coloration of these rocks (Allen et al., 1982; Jaimes Bermudez, 2023; Phinney et al., 1978). Sub-solidus oxidation processes of primary titanomagnetite have been associated with the formation of hematite and ilmenite displaying diverse textures (Rosa, 2011). Additionally, fractures filled with titanium-free hematite were reported. Investigations have revealed quartz-filled vugs, some up to 20 cm in diameter, and amygdaloidal structures filled with quartz and clays, between 1 mm to 5 cm in diameter, with quartz crystals growing from the rims to the center of these cavities (Jaimes Bermudez, 2023; Kerrigan & Osinski, 2015). Notably, a unique outcrop within the central islands

displayed approximately 1 mm-sized pyrite-filled cavities and a yellow fibrous iron-oxide covering the surface of the basement rocks (Kerrigan & Osinski, 2015).

A recent investigation by Jaimes Bermudez (2023) provided initial constraints on the evolution of the hydrothermal system. Their results showed three distinct alteration stages at the Clearwater West impact-generated hydrothermal system. First, there was a high-temperature stage (over 500°C) in which there was oxidation of primary igneous titanomagnetite and initial precipitation of pervasive acicular hematite crystals within the fine-grained impact melt rocks. The second stage entails the main alteration stage (cooling from 300°C to 100°C) where amygdules containing talc, saponite, quartz, and hematite formed, colloform bands of hematite and quartz developed within veins, and the precipitation of pervasive acicular hematite crystals continued. Lastly, there was a late alteration stage (below 100°C) characterized by the precipitation of goethite and quartz after the formation of colloform hematite bands (Jaimes Bermudez, 2023). Despite being addressed in earlier studies, specific details concerning hydrothermal alteration at the Clearwater West impact structure remain relatively unknown and warrant further exploration. A comprehensive investigation involving textural and geochemical data is necessary to fully characterize the origin, extent, distribution, and evolution of the impact-generated hydrothermal system within the impact structure.

## 1.6 Methods Background

### 1.6.1 Optical Microscopy

Optical microscopy involves using a microscope equipped with visible light and a series of lenses to observe and analyze objects at microscopic levels. Optical microscopes direct sourced light onto the specimen through a set of lenses, gather the transmitted or reflected light from the sample through another series of lenses, then direct it towards the eyepiece or camera. It is a non-destructive analysis method that utilizes the properties of light to magnify and illuminate specimens, allowing for identification and characterization of geological material based on structures, compositions, and properties. Colour, transparency, refractive index, and grain size, shape, and arrangement all provide

descriptive information about the formation, composition, and history of rocks and minerals.

### 1.6.2 Electron Microprobe Analysis

Electron microprobe analyzers (EMPA) can be used for a wide range of purposes including descriptive petrology, mineral identification, geothermobarometry, and zoning analysis (Reed, 2005a). In this study, an EMPA was used to gather three types of images: cathodoluminescence (CL), backscattered electron (BSE), secondary electron (SE). Elemental compositions of quartz were obtained by energy dispersive X-ray spectrometry (EDS) and wavelength dispersive X-ray spectrometry (WDS). EMPA involves electron detectors capturing specific signals produced by directing a focused beam of energetic electrons onto the sample of interest (Reed, 2005a). CL imaging focuses on the light emitted by the sample after being excited by the high-energy electron beam, BSE imaging focuses on the electrons in the beam that are scattered back from the sample surface, and SE imaging focuses on the secondary electrons that are emitted from the surface of the sample due to interactions with the high-energy electron beam (Ionescu & Hoeck, 2017). EDS elemental mapping imaging focuses on the X-rays of all energies emitted from the sample when the high energy electron beam interacts with the intrinsic electron structure (Reed, 2005b). WDS elemental mapping imaging focuses on X-rays of defined wavelengths, dictated by the orbital structure of each element, produced by the excitation and relaxation of electrons within the sample. All images are produced by converting the specific signals captured by electron detectors into electrical signals which are then processed and translated into visual images (Reed, 2005a). These images provide valuable information regarding a sample's elemental composition, structure, optical properties, and surface morphology at a micro- to nanoscopic level.

### 1.6.3 Fluid Inclusion Microthermometry

When a crystal forms in the presence of a fluid, it can trap some of the fluid within its structure, creating what is known as fluid inclusions (Bodnar, 2003). These inclusions can contain various forms of fluid, such as liquid, vapour, or supercritical fluid, with compositions ranging from pure water to brines of different salinity, as well as gas or gas-

bearing liquids. Fluid inclusions are commonly found in minerals, and it is more common to discover crystals with visible fluid inclusions (equal to or larger than 1 micrometer) than with no visible fluid inclusions (Bodnar, 2003). While there is no upper limit to the size of natural fluid inclusions, those larger than a few millimeters are uncommon. There are a few different kinds of fluid inclusions including primary, secondary, and pseudosecondary. Primary fluid inclusions form during the growth of the host crystal and therefore reflect conditions at the time of crystal formation, while secondary fluid inclusions are trapped after crystal growth is complete, often as a result of fracturing and subsequent healing, and therefore reflect conditions after crystal formation (Bodnar, 2003; Goldstein, 2003). Pseudosecondary fluid inclusions are technically primary inclusions since they also form during crystal growth, however, they resemble secondary inclusions due to simultaneous fracturing. The presence of one or a few fluid inclusions randomly distributed within the core of a crystal is indicative of a primary origin, particularly if the inclusions are relatively large compared to the crystal itself (Goldstein, 2003; Roedder, 1984). Secondary fluid inclusions can be easily identified by searching along fractures that cut across the entire crystal.

Fluid inclusion microthermometry allows for the collection of temperature data to determine the context of an ancient geological event. The data can detail the pressure, temperature, and composition of past circulating fluids, as well as timing of fluid entrapment (Goldstein, 2003). In this study, large enough (typically over 5 micrometers) primary two-phase (liquid-vapour) fluid inclusions (Figure 1.8) were the focus for microthermometry analysis, a heating and freezing technique used to analyze the fluids within the inclusions. Upon identification of a suitable fluid inclusions within each quartz sample, the stage was heated to find homogenization temperatures ($T_h$), cooled to find freezing temperatures ($T_f$), and then reheated again to find ice-melting temperatures ($T_m$). A 1°C/min heating rate was implemented to all heating and cooling experiments for observation precision. The heating-freezing stage was calibrated by measuring the ice-melting temperature of synthetic inclusions entrapped in quartz of pure $H_2O$ ($T_m = 0$°C) and $H_2O$–$CO_2$ inclusions ($T_m = -56.6$°C), with an error of +/- 0.1°C. The critical point of water (374.1°C) was selected as the upper calibration temperature.

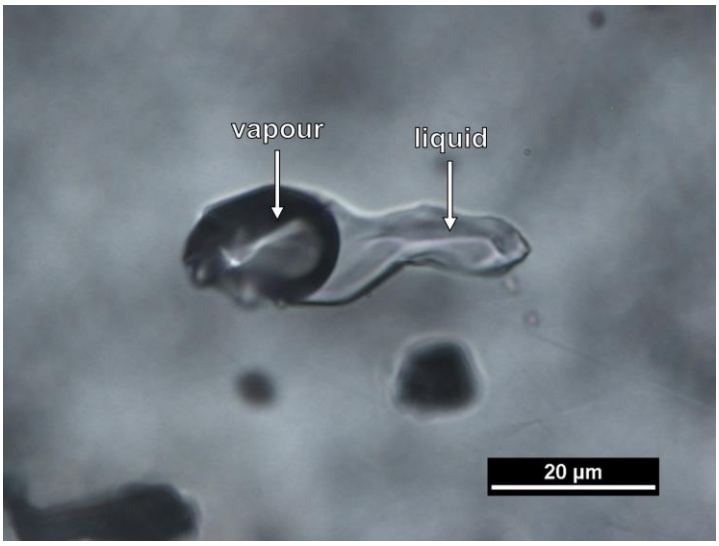


**Figure 1.9 Example of a quartz-hosted two-phase fluid inclusion (liquid and vapour present) from Clearwater West impact structure. Viewed with 100x lens in transmitted light under the microscope.**

### 1.6.4 Mass Spectrometry

A residual-gas quadrupole mass spectrometer system (QMS) (Figure 1.4) was used to quantitively analyze the composition of gases trapped within fluid inclusions. This study's methods for conducting quantitative fluid inclusion gas analysis by mass spectrometry are described by Blamey et al., 2015; Jones & Kesler, 1992; Norman & Blamey, 2001; Norman & Sawkins, 1987; and Parry & Blamey, 2010. The crush-fast scan (CFS) method, described by Norman et al., 2002; Norman & Blamey, 2001; Norman & Moore, 1997; Parry & Blamey, 2010, was utilized for the extraction and analysis of volatiles, enabling the high sensitivity detection of trace amounts (Blamey, 2012; Blamey et al., 2015). The incremental crushing procedure liberated bursts of mixed volatiles that were independently detected by the mass spectrometer. The released nonaqueous volatiles within the vacuum chamber endured 8 to 10 scans (approximately 2 seconds) administered by the analyzer before being withdrawn by the vacuum pump. The selected method does not necessitate the usage of a carrier gas, and the volatiles are not separated from one another, but are instead released into the chamber simultaneously. A Pfeiffer Prisma residual-gas quadrupole mass spectrometer (QMS) operating in fast-scan, peak-hopping mode at room temperature was used to investigate the volatiles.

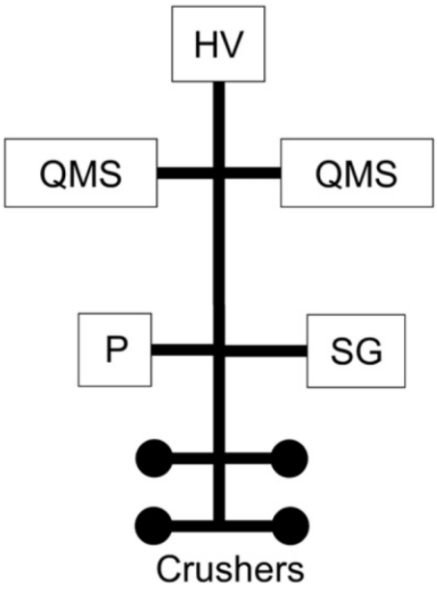


**Figure 1.10 Basic diagram of the residual-gas quadrupole mass spectrometer system showing all major components. The black circles represent the four chambers where the samples are placed for crushing. As the samples are incrementally crushed, the released gases pass through a pressure gauge (P) and the inlet for standard gases (SG) before being detected by two quadrupole mass spectrometers (QMS). The gases are then evacuated by a high vacuum (HV) system (Blamey, 2012).**

A matrix inversion was utilized to convert the current detected at each mass into a quantitative analysis (Isenhour & Jurs, 1979; Norman & Sawkins, 1987). This matrix considers the sensitivity factors for each gas as measured by Dr. Blamey. The gas to water ratio used for calibration is based on the Hansonburg fluorite standard, HF-1, which is 99.5% water and 0.5% gas as reported by Norman et al., (1985). During calibration, Praxair standards gas mixtures were employed for $H_2$, He, $CH_4$, and $CO_2$ gases, with the manufacturer specifying a 2% uncertainty. Using the same mass spectrometry system, Blamey et al., (2015) conducted 400 acquisitions, determining standard deviations of 0.061% for $CH_4$, 0.062% for $CO_2$, and 0.043% for $N_2$ regarding their composition measurements. $N_2$, $O_2$, and Ar gases were sourced from the atmosphere, with no assigned uncertainty. To establish the background instrument noise,

dry run measurements were taken when no sample was being analyzed. The signal was recorded while the sample was exposed to the main chamber, encompassing all residual gases that constitute the background while the turbo pump was operating at a maximum speed of 90,000 revolutions per minute. The mass spectrometer began recording and cycled through the selected masses associated with the gases under analysis. Approximately 30 seconds later, the incremental crush took place. The background was measured for 10 cycles, stopping 1 second before the gas burst. Both the mean and standard deviation of the background signal were documented. To simulate a crush absent of mineral-hosted inclusion gases, blanks of inclusion-free quartz cuvettes were used.

Although it is customary for geochemists to consider $2\sigma$ as the confidence limit, corresponding to a 95% confidence limit, the detection limit for this study employed a 99% confidence limit, roughly equating to a $3\sigma$ value (a quarter of a ppm), to verify that the gas bursts contained a concentration greater than zero (Blamey et al., 2015). The $2\sigma$ detection limit for the mass spectrometer in its current setup ranges from 0.8 to 1.2 femtomole ($10^{-15}$ mol), but also depends on noise within the mass spectrometer. Total errors were calculated using the following components: blank compositions, background instrument noise; interferences in measuring gas species; analytical errors in measuring current; error in linear range; uncertainty in gas composition; and the conversion of the mass spectrometer current into mols which applies only to the summary data tables (Appendix A) (Blamey et al., 2015).

Interferences were identified as potentially relevant in the measurement of gas species. Firstly, analysts often consider the analysis of $CH_4$ at $m/e$ = 16, which is the major peak. However, this mass corresponds to a minor interference caused by a fragmented water ion. In this study, $m/e$ = 15 was utilized instead of 16 for methane analysis. The $m/e$ = 15 peak ($CH_3^+$) represents approximately 90% of the $m/e$ = 16 peak and avoids interference corrections from water. Although there is a trade-off of a 10% increased error at $m/e$ = 15, it proves more advantageous for methane analysis by eliminating interference with water. In addition, a very minor interference of 0.032% due to $CO_2$ can be detected at $m/e$ = 32, which is the principal mass for oxygen. Given its low value, no adjustment was

made for this interference. The principal interference encountered involves the fragmentation of $CO_2$, producing $CO^+$ ion, which correspond to the analysis of $N_2$ at *m/e* = 28. Approximately 8.2% of the total $CO_2$ signal is attributed to $CO^+$ at *m/e* = 28. However, considering that the $CO_2$ content is typically less than half that of $N_2$ in the Clearwater West samples, the contribution of $CO^+$ to the *m/e* = 28 signal is less than 4%. The $CO_2$ content at *m/e* = 44 is used to subtract this contribution from the $N_2$ value. The relative error onto $N_2$ incorporates a square function, resulting in $CO_2$ contributing approximately 0.16% to the relative $N_2$ error.

## 1.7 Thesis Structure and Objectives

As previously stated, hypervelocity impact events into rocky planetary bodies containing water can form hydrothermal systems in which life can thrive. These sites hold significant importance for future space exploration missions, especially to Mars, as they have the ability to preserve evidence of extraterrestrial life. The following provides an outline of the structure of this thesis:

Chapter 2 examines the alteration mineralogy and geochemistry of quartz at the Clearwater West impact-generated hydrothermal system. This chapter utilizes the methods of optical microscopy, electron microprobe analysis (EMPA), fluid inclusion microthermometry, and residual gas quadrupole mass spectrometry (QMS) to characterize quartz vugs. Quartz microtextures, fluid inclusion homogenization, freezing, and ice-melting temperatures, and fluid inclusion volatile chemistries are used to constrain the fluid sources and thermochronology of the system. In addition, the results are compared with other impact-generated hydrothermal systems on Earth.

Chapter 3 summarizes the results from the previous chapter and includes implications of the conclusions reached within the context of the search for past or present habitable environments on Mars.

## 1.8 References

Abramov, O., & Kring, D. A. (2004). Numerical modeling of an impact-induced hydrothermal system at the Sudbury crater. *Journal of Geophysical Research*, *109*, E10007. https://doi.org/10.1029/2003je002213

Abramov, O., & Kring, D. A. (2005). Impact-induced hydrothermal activity on early Mars. *Journal of Geophysical Research*, *110*, E12S09. https://doi.org/10.1029/2005je002453

Abramov, O., & Kring, D. A. (2007). Numerical modeling of impact-induced hydrothermal activity at the Chicxulub crater. *Meteoritics and Planetary Science*, *42*, 93–112. https://doi.org/10.1111/j.1945-5100.2007.tb00220.x

Allen, C. C., Gooding, J. L., & Keil, K. (1982). Hydrothermally altered impact melt rock and breccia: Contributions to the soil of Mars. *Journal of Geophysical Research: Solid Earth*, *87*(B12), 10083–10101. https://doi.org/10.1029/jb087ib12p10083

Beals, C. S., Ferguson, G. M., & Landau, A. (1956). Canadian scientists report (II. A search for analogies between lunar and terrestrial topography on photographs of the Canadian Shield, Part I). *Journal of the Royal Astronomical Society of Canada*, *50*, 203–261.

Blamey, N. J. F. (2012). Composition and evolution of crustal, geothermal and hydrothermal fluids interpreted using quantitative fluid inclusion gas analysis. *Journal of Geochemical Exploration*, *116–117*, 17–27. https://doi.org/10.1016/j.gexpl.2012.03.001

Blamey, N. J. F., Parnell, J., McMahon, S., Mark, D. F., Tomkinson, T., Lee, M. R., Shivak, J., Izawa, M. R. M., Banerjee, N. R., & Flemming, R. L. (2015). Evidence for methane in Martian meteorites. *Nature Communications*, *6*(1), 7399. https://doi.org/10.1038/ncomms8399

Bodnar, R. J. (2003). Introduction to fluid inclusions. In I. Samson, A. Anderson, & D. Marshall (Eds.), *Fluid Inclusions: Analysis and Interpretation* (32nd ed., pp. 1–8). Mineralogical Association of Canada. https://doi.org/10.3749/9780921294672.ch01

Bostock, H. H. (1969). The Clearwater Complex, New Quebec. *Geological Survey of Canada*, *178*.

Bunch, T. E. (1968). Some characteristics of selected minerals from craters. In B. M. French & N. M. Short (Eds.), *Shock Metamorphism of Natural Materials* (pp. 413–432). Mono Book Corporation.

Cockell, C. S. (2006). The origin and emergence of life under impact bombardment. *Philosophical Transactions of the Royal Society of London. Series B, Biological Sciences*, *361*(1474), 1845–1856. https://doi.org/10.1098/rstb.2006.1908

Cockell, C. S., & Lee, P. (2002). The biology of impact craters - A review. *Biological Reviews of the Cambridge Philosophical Society*, *77*(3), 279–310. https://doi.org/10.1017/s146479310100584x

Cockell, C. S., Lee, P., Broady, P., Lim, D. S. S., Osinski, G. R., Parnell, J., Koeberl, C., Pesonen, L., & Salminen, J. (2005). Effects of asteroid and comet impacts on habitats for lithophytic organisms—A synthesis. *Meteoritics and Planetary Science*, *40*(12), 1901–1914. https://doi.org/10.1111/j.1945-5100.2005.tb00153.x

Cockell, C. S., Osinski, G. R., & Lee, P. (2003). The impact crater as a habitat: Effects of impact processing of target materials. *Astrobiology*, *3*(1), 181–191. https://doi.org/10.1089/153110703321632507

Cockell, C. S., Osinski, G. R., & Voytek, M. A. (2012). The geomicrobiology of impact structures. In G. R. Osinski & E. Pierazzo (Eds.), *Impact Cratering: Processes and Products* (pp. 157–176). Wiley-Blackwell. https://doi.org/10.1002/9781118447307.ch11

Dence, M. R. (1964). A comparative structural and petrographic study of probable Canadian meteorite craters. *Metoritics*, *2*(3), 249. https://doi.org/10.1111/j.1945-5100.1964.tb01432.x

Dence, M. R. (1968). Shock zoning at Canadian craters: Petrography and structural implications. In B. M. French & N. M. Short (Eds.), *Shock Metamorphism of Natural Materials* (pp. 169–184). Mono Book Corporation.

Dence, M. R., Innes, M. J. S., & Beals, C. S. (1965). On the probable meteorite origin of the Clearwater Lakes, Quebec. *Journal of the Royal Astronomical Society of Canada*, *59*, 13–22.

Dirri, F., Longobardo, A., Palomba, E., Berthoud, L., Hutzler, A., Smith, C. L., & Russell, S. S. (2021). Recovery and transport of samples. In A. Longobardo (Ed.), *Sample Return Missions: The Last Frontier of Solar System Exploration* (pp. 297–314). Elsevier. https://doi.org/10.1016/b978-0-12-818330-4.00015-x

French, B. M. (1998). Traces of catastrophe: A handbook of shock-metamorphic effects in terrestrial meteorite impact structures. *29th Lunar and Planetary Science Conference*, Contribution No. 954.

French, B. M., & Koeberl, C. (2010). The convincing identification of terrestrial meteorite impact structures: What works, what doesn't, and why. *Earth-Science Reviews*, *98*(1–2), 123–170. https://doi.org/10.1016/j.earscirev.2009.10.009

Gault, D. E., Oberbeck, V. R., & Quaide, W. L. (1968). Impact cratering mechanics and structures. In B. M. French & N. M. Short (Eds.), *Shock Metamorphism of Natural Materials* (pp. 87–99). Mono Book Corporation.

Goldstein, R. H. (2003). Petrographic analysis of fluid inclusions. In I. Samson, A. Anderson, & D. Marshall (Eds.), *Fluid Inclusions: Analysis and Interpretation* (32nd ed., pp. 9–53). Mineralogical Association of Canada. https://doi.org/10.3749/9780921294672.ch02

Grieve, R. A. F. (2006). Impact structures of Canada. *GEOtext 5, Geological Association of Canada*.

Hische, R. (1995). *Geologie der Clearwater-Impaktstruktur / Quebec [Geology of the Clearwater impact structure / Quebec]*. Westfälische Wilhelms-Universität Münster.

Holsapple, K. A. (1987). The scaling of impact phenomena. *International Journal of Impact Engineering*, *5*(1–4), 343–355. https://doi.org/10.1016/0734-743x(87)90051-0

Ionescu, C., & Hoeck, V. (2017). Electron microprobe analysis (EMPA). In A. M. W. Hunt (Ed.), *The Oxford Handbook of Archaeological Ceramic Analysis* (pp. 288–304). Oxford University Press. https://doi.org/10.1093/oxfordhb/9780199681532.013.17

Isenhour, T. L., & Jurs, P. C. (1979). *Introduction to computer programming for chemists*. Allyn & Baco.

Jaimes Bermudez, J. (2023). *Investigation of the impact-generated hydrothermal system at the West Clearwater Lake impact structure, Quebec, Canada*. University of Western Ontario.

Jébrak, M. (2015). Hydrothermal Alteration. In M. Gargaud, W. M. Irvine, R. Amils, H. J. Cleaves, D. L. Pinti, J. C. Quintanilla, D. Rouan, T. Spohn, S. Tirard, & M. Viso (Eds.), *Encyclopedia of Astrobiology* (pp. 1156–1157). Springer, Berlin, Heidelberg. https://doi.org/10.1007/978-3-662-44185-5_5150

Jõeleht, A., Kirsimäe, K., Plado, J., Versh, E., & Ivanov, B. A. (2005). Cooling of the Kärdla impact crater: II. Impact and geothermal modeling. *Meteoritics and Planetary Science*, *40*(1), 21–33. https://doi.org/10.1111/j.1945-5100.2005.tb00362.x

Jones, H. D., & Kesler, S. E. (1992). Fluid inclusion gas chemistry in East Tennessee Mississippi Valley-type districts: Evidence for immiscibility and implications for depositional mechanisms. *Geochimica et Cosmochimica Acta*, *56*, 137–154.

Kenkmann, T., Poelchau, M. H., & Wulf, G. (2014). Structural geology of impact craters. *Journal of Structural Geology*, *62*, 156–182. https://doi.org/10.1016/j.jsg.2014.01.015

Kerrigan, M. C., & Osinski, G. R. (2015). Overview of impact-generated hydrothermal activity at the West Clearwater Lake impact structure, Canada. *46th Lunar and Planetary Science Conference*.

Kirsimäe, K., & Osinski, G. R. (2012). Impact-induced hydrothermal activity. In G. R. Osinski & E. Pierazzo (Eds.), *Impact Cratering: Processes and Products* (pp. 76–89). Wiley-Blackwell. https://doi.org/10.1002/9781118447307.ch6

Krank, S. H., & Sinclair, G. W. (1963). Clearwater Lake, New Quebec. *Geological Survey of Canada, B.*

McIntyre, D. B. (1968). Impact metamorphism at Clearwater Lake, Quebec. In B. M. French & N. M. Short (Eds.), *Shock Metamorphism of Natural Materials* (pp. 363–366). Mono Book Corporation.

Melosh, H. J. (1989). *Impact cratering: A geologic process*. Oxford University Press.

Melosh, H. J., & Ivanov, B. A. (1999). Impact crater collapse. *Annual Review of Earth and Planetary Sciences*, *27*, 385–415. https://doi.org/10.1146/annurev.earth.27.1.385

Merino, N., Aronson, H. S., Bojanova, D. P., Feyhl-Buska, J., Wong, M. L., Zhang, S., & Giovannelli, D. (2019). Living at the extremes: Extremophiles and the limits of life in a planetary context. *Frontiers in Microbiology*, *10*, Article 780. https://doi.org/10.3389/fmicb.2019.00780

Meyer, M. A., Kminek, G., Beaty, D. W., Carrier, B. L., Haltigin, T., Hays, L. E., Agree, C. B., Busemann, H., Cavalazzi, B., Cockell, C. S., Debaille, V., Glavin, D. P., Grady, M. M., Hauber, E., Hutzler, A., Marty, B., McCubbin, F. M., Pratt, L. M., Regberg, A. B., … Zorzano, M. P. (2022). Final report of the Mars sample return science planning group 2 (MSPG2). *Astrobiology*, *22*(S1), S5–S26. https://doi.org/10.1089/ast.2021.0121

Naumov, M. V. (2002). Impact-generated hydrothermal systems: Data from Popigai, Kara, and Puchezh-Katunki impact structures. In *Impacts in Precambrian Shields* (pp. 117–171). Springer, Berlin, Heidelberg.

Naumov, M. V. (2005). Principal features of impact-generated hydrothermal circulation systems: Mineralogical and geochemical evidence. *Geofluids*, *5*, 165–184. https://doi.org/10.1111/j.1468-8123.2005.00092.x

Norman, D. I., & Blamey, N. J. F. (2001). Quantitative analysis of fluid inclusion volatiles by a two quadrupole mass spectrometer system. *16th ECROFI: European Current Research on Fluid Inclusions*.

Norman, D. I., Blamey, N. J. F., & Moore, J. N. (2002). Interpreting geothermal processes and fluid sources from fluid inclusion organic compounds and $CO_2/N_2$ ratios. *27th Workshop on Geothermal Reservoir Engineering*.

Norman, D. I., & Moore, J. N. (1997). Gaseous species in fluid inclusions: A fluid tracer and indicator of fluid processes. *14th ECROFI: European Current Research on Fluid Inclusions*.

Norman, D. I., & Sawkins, F. J. (1987). Analysis of volatiles in fluid inclusions by mass spectrometry. *Chemical Geology*, *61*(1–4), 1–10. https://doi.org/10.1016/0009-2541(87)90020-9

Norman, D. I., Ting, W., Putnam III, B. R., & Smith, R. W. (1985). Mineralization of the Hansonburg Mississippi-Valley-type deposit, New Mexico: Insight from composition of gases in fluid inclusions. *Canadian Mineralogist*, *23*, 353–368.

Norton, D. L. (1984). Theory of hydrothermal systems. *Annual Review of Earth and Planetary Sciences*, *12*, 155–177.

Osinski, G. R., Brunner, A., Collins, G. S., Cohen, B. A., Coulter, A., Elphic, R., Grieve, R. A. F., Hodges, K., Horne, A., Kerrigan, M. C., Lim, D. S. S., Misener, R., Morgan, J. V., Rae, A. S. P., Saint-Jacques, D., Skok, J. R., Squyres, S., Tornabene, L. L., Wilks, R., & Young, K. (2015). Revisiting the West Clearwater Lake structure, Canada. *46th Lunar and Planetary Science Conference*.

Osinski, G. R., Cockell, C. S., Pontefract, A., & Sapers, H. M. (2020). The role of meteorite impacts in the origin of life. *Astrobiology*, *20*(9), 1121–1149. https://doi.org/10.1089/ast.2019.2203

Osinski, G. R., Grieve, R. A. F., Bleacher, J. E., Neish, C. D., Pilles, E. A., & Tornabene, L. L. (2018). Igneous rocks formed by hypervelocity impact. *Journal of Volcanology and Geothermal Research*, *353*, 25–54. https://doi.org/10.1016/j.jvolgeores.2018.01.015

Osinski, G. R., Grieve, R. A. F., Ferrière, L., Losiak, A., Pickersgill, A. E., Cavosie, A. J., Hibbard, S. M., Hill, P. J. A., Jaimes Bermudez, J., Marion, C. L., Newman, J. D., & Simpson, S. L. (2022). Impact Earth: A review of the terrestrial impact record. *Earth-Science Reviews*, *232*, E01008. https://doi.org/10.1016/j.earscirev.2022.104112

Osinski, G. R., Grieve, R. A. F., & Tornabene, L. L. (2012). Excavation and impact ejecta emplacement. In G. R. Osinski & E. Pierazzo (Eds.), *Impact Cratering: Processes and Products* (pp. 43–59). Wiley-Blackwell. https://doi.org/10.1002/9781118447307.ch4

Osinski, G. R., Lee, P., Parnell, J., Spray, J. G., & Baron, M. (2005). A case study of impact-induced hydrothermal activity: The Haughton impact structure, Devon Island, Canadian High Arctic. *Meteoritics and Planetary Science*, *40*(12), 1859–1877. https://doi.org/10.1111/j.1945-5100.2005.tb00150.x

Osinski, G. R., & Pierazzo, E. (2012). Impact cratering: Processes and products. In G. R. Osinski & E. Pierazzo (Eds.), *Impact Cratering: Processes and Products* (pp. 43–59). Wiley-Blackwell. https://doi.org/10.1002/9781118447307.ch1

Osinski, G. R., Spray, J. G., & Lee, P. (2001). Impact-induced hydrothermal activity within the Haughton impact structure, arctic Canada: Generation of a transient, warm, wet oasis. *Meteoritics and Planetary Science*, *36*(5), 731–745. https://doi.org/10.1111/j.1945-5100.2001.tb01910.x

Osinski, G. R., Tornabene, L. L., Banerjee, N. R., Cockell, C. S., Flemming, R. L., Izawa, M. R. M., McCutcheon, J., Parnell, J., Preston, L. J., Pickersgill, A. E., Pontefract, A., Sapers, H. M., & Southam, G. (2013). Impact-generated hydrothermal systems on Earth and Mars. *Icarus*, *224*(2), 347–363. https://doi.org/10.1016/j.icarus.2012.08.030

Osinski, G. R., Tornabene, L. L., Banerjee, N. R., Cockell, C. S., Flemming, R. L., Izawa, M. R. M., McCutcheon, J., Pontefract, A., Parnell, J., Sapers, H. M., & Southam, G. (2012). Impact craters as habitats for life on early Mars. *3rd Conference on Early Mars*, Contribution No. 7068. https://doi.org/10.1016/j.gca.2006.06.175

Osinski, G. R., Tornabene, L. L., & Grieve, R. A. F. (2011). Impact ejecta emplacement on terrestrial planets. *Earth and Planetary Science Letters*, *310*(3–4), 167–181. https://doi.org/10.1016/j.epsl.2011.08.012

Parnell, J., Taylor, C. W., Thackrey, S., Osinski, G. R., & Lee, P. (2010). Permeability data for impact breccias imply focussed hydrothermal fluid flow. *Journal of Geochemical Exploration*, *106*(1–3), 171–175. https://doi.org/10.1016/j.gexplo.2009.12.002

Parry, W. T., & Blamey, N. J. F. (2010). Fault fluid composition from fluid inclusion measurements, Laramide age Uinta thrust fault, Utah. *Chemical Geology*, *278*(1–2), 105–119. https://doi.org/10.1016/j.chemgeo.2010.09.005

Phinney, W. C., Simonds, C. H., Cochran, A., McGee, P. E., Simonds, C. H., Cochran, A., & McGee, P. E. (1978). West Clearwater, Quebec impact structure, Part II: Petrology. *9th Lunar and Planetary Science Conference*, *2*, 2659–2694.

Pickersgill, A. E., Chris-Tou, E., Mark, D. F., Lee, M. R., Tremblay, M. M., Rasmussen, C., Morgan, J. V., Gulick, S. P. S., Schmieder, M., Bach, W., Osinski, G. R., Simpson, S. L., Kring, D. A., Cockell, C. S., Collins, G. S., Christeson, G., Tikoo, S., Stockli, D., Ross, C., … Expedition 364 Scientists. (2019). Six million years of hydrothermal activity at Chicxulub? *6th Large Meteorite Impacts and Planetary Evolution Conference*, Contribution No. 2136.

Pilkington, M., & Grieve, R. A. F. (1992). The geophysical signature of terrestrial impact craters. *Reviews of Geophysics*, *30*(2), 161–181. https://doi.org/10.1029/92rg00192

Pirajno, F. (2009). Hydrothermal processes associated with meteorite impacts. In F. Pirajno (Ed.), *Hydrothermal Processes and Mineral Systems* (pp. 1097–1130). Springer, Dordrecht. https://doi.org/10.1007/978-1-4020-8613-7_11

Pontefract, A., Osinski, G. R., Cockell, C. S., Moore, C. A., Moores, J. E., & Southam, G. (2014). Impact-generated endolithic habitat within crystalline rocks of the Haughton impact structure, Devon Island, Canada. *Astrobiology*, *14*(6), 522–533. https://doi.org/10.1089/ast.2013.1100

Pontefract, A., Osinski, G. R., Cockell, C. S., Southam, G., McCausland, P. J. A., Umoh, J., & Holdsworth, D. W. (2016). Microbial diversity of impact-generated habitats. *Astrobiology*, *16*(10), 775–786. https://doi.org/10.1089/ast.2015.1393

Reed, S. J. B. (2005a). Introduction. In S. J. B. Reed (Ed.), *Electron Microprobe Analysis and Scanning Electron Microscopy in Geology* (2nd ed., pp. 1–6). Cambridge University Press. https://doi.org/10.1017/cbo9780511610561.002

Reed, S. J. B. (2005b). X-ray spectrometers. In S. J. B. Reed (Ed.), *Electron Microprobe Analysis and Scanning Electron Microscopy in Geology* (2nd ed., pp. 76–96). Cambridge University Press. https://doi.org/10.1017/cbo9780511610561.005

Robertson, P. B., Dence, M. R., & Vos, M. A. (1968). Deformation in rock-forming minerals from Canadian craters. *Contributions from the Dominion Astrophysical Observatory in Victoria*, *8*(23), 20.

Roedder, E. (1984). Fluid inclusions. *Mineralogical Society of America: Reviews in Mineralogy*, *12*, 644 pages. https://doi.org/10.1515/9781501508271

Rosa, D. F. (2011). *The sheet of impact melt at West Clearwater Lake, Northern Quebec*. McGill University.

Schmieder, M., & Jourdan, F. (2013). The Lappajärvi impact structure (Finland): Age, duration of crater cooling, and implications for early life. *Geochimica et Cosmochimica Acta*, *112*, 321–339. https://doi.org/10.1016/j.gca.2013.02.015

Schmieder, M., Schwarz, W. H., Trieloff, M., Tohver, E., Buchner, E., Hopp, J., & Osinski, G. R. (2015). New 40Ar/39Ar dating of the Clearwater Lake impact structures (Québec, Canada) – Not the binary asteroid impact it seems? *Geochimica et Cosmochimica Acta*, *148*, 304–324. https://doi.org/10.1016/j.gca.2014.09.037

Shoemaker, E. M. (1960). Penetration mechanics of high velocity meteorites: Illustrated by Meteor Crater, Arizona. *21st International Geological Congress*, 418–434.

Simard, M., Labbé, J. Y., Lacoste, P., Leclerc, A., & Boily, M. (2008). Synthèse du nord-est de la province du Supérieur [Synthesis of the northeast of the Superior Province]. *Ministère Des Ressources Naturelles, Québec*, 199 pages.

Simard, M., Parent, M., Thériault, R., David, J., Lacoste, P., & Sharma, K. N. M. (2004). Géologie de la région du lac à l'Eau Claire (34B et 34C) [Geology of the Clearwater Lake area (34B and 34C)]. *Ministère Des Ressources Naturelles, Québec*, 48 pages.

Simonds, C. H., Phinney, W. C., McGee, P. E., & Cochran, A. (1978). West Clearwater, Quebec impact structure, Part I : Field geology, structure and bulk chemistry. *9th Lunar and Planetary Science Conference*, 2633–2658.

Simpson, S. L. (2020). *Clay mineral characterization and production in impact settings: A case study on the Chicxulub impact strcutre, Mexico*. University of Western Ontario.

Singleton, A. C., Osinski, G. R., McCausland, P. J. A., & Moser, D. E. (2011). Shock-induced changes in density and porosity in shock-metamorphosed crystalline rocks, Haughton impact structure, Canada. *Meteoritics and Planetary Science*, *46*(11), 1774–1786. https://doi.org/10.1111/j.1945-5100.2011.01290.x

Stetter, K. O. (2007). Hyperthermophiles in the history of life. In G. R. Bock & J. A. Goode (Eds.), *Ciba Foundation Symposium 202 - Evolution of Hydrothermal Ecosystems on Earth (and Mars?)* (pp. 1–23). John Wiley & Sons, Ltd. https://doi.org/10.1002/9780470514986.ch1

Versh, E., Kirsimäe, K., & Jõeleht, A. (2006). Development of potential ecological niches in impact-induced hydrothermal systems: The small-to-medium size impacts. *Planetary and Space Science*, *54*(15), 1567–1574. https://doi.org/10.1016/i.pss.2005.12.022

Wang, Q., Cen, Z., & Zhao, J. (2015). The survival mechanisms of thermophiles at high temperatures: An angle of omics. *Physiology*, *30*(2), 97–106. https://doi.org/10.1152/physiol.00066.2013

# Chapter 2

# 2 Fluid and Thermal Evolution of the Clearwater West Impact-Generated Hydrothermal System

## 2.1 Introduction

Hypervelocity impact cratering is a high-speed collision between a projectile, such as an asteroid or comet, and a planetary surface, and occurs across all solid surfaces of planets and moons within our solar system (e.g., Cockell, 2006; French, 1998; Osinski et al., 2013, 2020). Impact events into target rocks covered by, or containing $H_2O$, such as seas and lakes, groundwater, or permafrost/ice, have the ability to induce hydrothermal activity, despite their initial devastating effects (Kirsimäe & Osinski, 2012; Osinski et al., 2013; Pierazzo & Melosh, 2012). A hydrothermal system refers to the movement of mass and energy through thermal, chemical, and mechanical processes, driven by the circulation of fluids and molecular diffusion (Norton, 1984). Their formation depends on the presence of sufficient heat from uplifted geothermal gradients and/or impact melt-bearing rocks, sustained permeability for fluid circulation, and a supply of volatiles such as liquid water, water derived from melting ice, or water released by the dehydration and degassing of minerals (Abramov & Kring, 2004, 2007; Naumov, 2005; Osinski et al., 2013; Parnell et al., 2010). In addition, the type of hydrothermal alteration that develops depends on several factors including the type of crater (continental or marine), the source of circulating fluids (meteoric water, seawater, basinal brines, or mineral-bound water), duration of the hydrothermal activity, and system cooling rates (Osinski et al., 2013).

Impact-generated hydrothermal deposits can offer transient habitats suitable for microbial life and provide reactive surfaces where prebiotic chemistry can concentrate (Cockell, 2006; Naumov, 2005; Parnell et al., 2004; Pontefract et al., 2014; Sleep, 2018). Initially, temperatures are too elevated to foster life, but after the dissipation of impact-generated heat, surface temperatures gradually return to pre-impact values (Cockell & Lee, 2002). Cooling hydrothermal systems can support autotrophic thermo- and hyperthermophilic microorganisms (extremophiles with optimum growth temperatures between 45 - 80°C and 80 - 120°C, respectively) (Stetter, 2007; Wang et al., 2015), since all components

necessary for biotic reactions, including liquid water, energy, and dissolved chemicals and nutrients, are present in porous rocks within these systems for an extended period of time (Abramov & Mojzsis, 2009; Cockell, 2006; Cockell et al., 2005; Merino et al., 2019; Osinski et al., 2013; Versh et al., 2006). Hence, impact-generated hydrothermal systems expand the potential for any terrestrial planetary body (e.g., Mars, Europa, and Titan) with the essential ingredients for life (which could also be delivered by the impact) to be at least temporarily habitable (Osinski et al., 2020). On Earth, these systems have been generated in impact craters with diameters over a few kilometers (Kirsimäe & Osinski, 2012; Naumov, 2005; Osinski, Tornabene, et al., 2012), and often create diverse ecological niches, both during and long after their activity (Cockell et al., 2005; Cockell & Lee, 2002; Osinski et al., 2020). 188 hypervelocity impact craters have been documented on Earth to date, with 70 of them containing evidence of hydrothermal circulation (Naumov, 2002, 2005; Osinski et al., 2013, 2022). However, detailed studies of impact-generated hydrothermal systems on Earth remain limited due to their preservation and accessibility challenges.

Although Earth's impact-generated hydrothermal systems are difficult to study due to the modification of crater surface expressions from erosion, subduction, and/or burying, investigating such systems on other planetary surfaces poses an even greater challenge. Consequently, scientific investigation is only currently possible by utilizing such systems on Earth as analogues for extraterrestrial surfaces, such as Mars. However, there is exciting progress on the horizon with the upcoming NASA and ESA Mars sample return mission from Jezero Crater, expected to return to Earth in 2033 (Dirri et al., 2021; Meyer et al., 2022). This mission, and the many that will likely follow, hold the potential to significantly advance our understanding of impact-generated hydrothermal processes and their generated transient habitable conditions on other planetary bodies. Impact-generated hydrothermal deposits may provide some of the best and most numerous opportunities for uncovering preserved evidence for life on Mars, since they can offer abundant energy for cellular metabolism (Osinski et al., 2020; Osinski, Tornabene, et al., 2012; Parnell et al., 2010; Pontefract et al., 2014). In addition, such deposits have been shown to preserve microbial fossils and organic biomarkers on Earth (Parnell et al., 2004; Sapers et al., 2015).

In an effort to contribute to the understanding of the formation and evolution, and the astrobiological implications of impact-generated hydrothermal systems on other planetary bodies, including Mars, this thesis focuses on the characterization of a terrestrial analogue: the Clearwater West impact structure, located in northern Quebec, Canada. This impact structure stands as one of the most well-preserved large complex impact structures on Earth (Osinski et al., 2015). By examining the geochemistry and alteration mineralization of impactite-hosted quartz vugs, this thesis aims to constrain the fluid and thermal evolution of the associated hydrothermal system. The findings and implications of this study are primarily focused on Mars but are also relevant to other terrestrial planetary bodies containing past or present water sources. The overall goal is to provide valuable insights into the potential for habitability beyond our own planet.

## 2.2 Geological Setting & Previous Work

The Clearwater West impact structure is one of two circular structures that form the Clearwater Lakes, located in northern Quebec, Canada, (Figure 2.1) approximately 125 km East of Hudson Bay at 56°08′N 74°18′W (Dence et al., 1965; Simonds et al., 1978). In 1963, Krank and Sinclair from the Geological Survey of Canada studied the Clearwater West impact structure and originally concluded that the structure had a volcanic origin due to their main observations of “red breccia” and “grey dacite”. This conclusion was also reached by Bostock, who conducted a more in-depth study of the structure involving geologic mapping, petrographic observations, and bulk chemical analysis (Bostock, 1969). At around the same time, evidence supporting an impact origin was found, including shock-induced mineral phases (such as lechatelierite and maskelynite), shatter cones, allochthonous breccias, and thin veinlets of melt rock (Beals et al., 1956; Dence, 1964; Dence et al., 1965). This hypothesis of an impact-related origin was further supported by subsequent observations of impact-induced shock metamorphism (Bunch, 1968; McIntyre, 1968; Robertson et al., 1968). Ten years later, the hypothesis was further corroborated by petrographic and chemical examination of the impact and target lithologies and analysis of the field geology and structural relations (Phinney et al., 1978; Simonds et al., 1978).

The structure was originally thought to be part of a binary impact scenario, given its close proximity to the Clearwater East impact structure, with only a 30 km distance from the centre of each structure (Dence et al., 1965). However, $^{40}Ar/^{39}Ar$ dating of melt rocks has shown that the Clearwater East impact structure is much older, dating back to 460-470 million years ago during the Middle Ordovician, while the Clearwater West impact structure is approximately 286 ± 2.2 million years old, forming during the Early Permian (Schmieder et al., 2015). These findings, paired with paleographic reconstructions, confirm that the Clearwater West impact structure was formed in the single continent of Pangea.

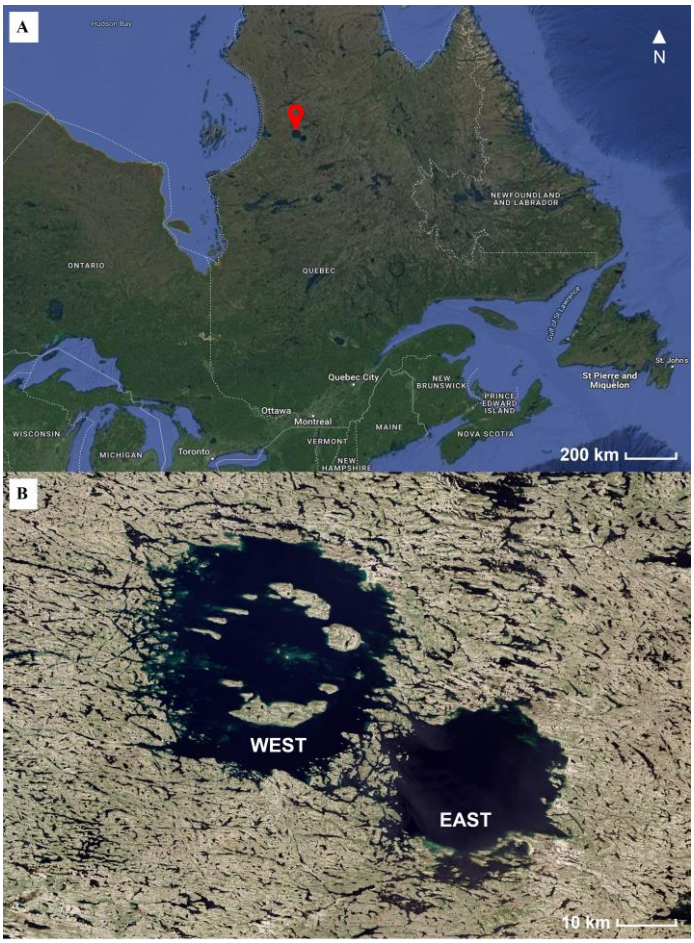


**Figure 2.1 Satellite images showing the localization of the Clearwater West impact structure. A) Regional geographic context of the Clearwater West impact structure (depicted with a red pin). B) Topography of Clearwater East and West impact structures. Source: Landsat 8 Operational Land Imager (OLI).**

With a diameter of around 36 km, the Clearwater West impact structure is approximately 10 km larger than the older Clearwater East impact structure (Figure 2.1B) (Grieve, 2006). The Clearwater East impact structure remains relatively unstudied since the majority of its features are submerged in the overlying lake, resulting in limited surface exposure (Dence, 1964; Dence et al., 1965; Grieve, 2006). The majority of data derived from geophysical studies and two drilled cores obtained in the 1960s (Dence, 1964; Dence et al., 1965). In contrast, the Clearwater West impact structure exhibits a higher degree of preservation and is characterized by a ring of islands of around 16 km in diameter within the approximately 30 km-diameter lake (Osinski et al., 2015). These islands are part of the impact structure's central uplift and a group of small islands (less than 100 m across) located in its center are part of the central peak (Figure 2.1B) (Grieve, 2006). The structure has two troughs, one with depths exceeding 100 m between the shoreline and the peak ring, and the other with a maximum depth of 50 m between the peak ring and central peak. The hypervelocity impact that formed the Clearwater West impact structure occurred in the northern section of the Bienville Domain of the Minto Subprovince within the Canadian Shield's Superior Province (Simard et al., 2004, 2008). This area is characterized by local Archean plutonic rocks, mainly including granodiorite, quartz monzonite, granite, and amphibolite rocks, and are intruded by Proterozoic age diabase dikes (Bostock, 1969; Schmieder et al., 2015). The impact melt rocks contain limestone clasts from the Ordovician age, suggesting a thin cover of sedimentary rocks present at the time of impact (Hische, 1995; Simonds et al., 1978).

### 2.2.1 Impactites

Allochthonous impactites, ranging from intact to highly brecciated, overly the fractured uplifted basement rocks of the structure, with shatter cones commonly present, yet poorly developed, on the central islands (Osinski et al., 2015). Impact melt rock veins have been identified and represent injected shock melt, not in-situ pseudotachylite, as previously thought (Wilks, 2016). Overlying the fractured basement is a largely monomict lithic breccia that is melt-free, which has been documented on several islands with a reddish hue and thicknesses ranging from 0 to 20 m (Bostock, 1969; Phinney et al., 1978; Simonds et al., 1978). Above this layer is a distinctive impact melt-bearing lithic breccia

which contains a range of various quantities of oxidized red impact melt particles within a clastic matrix (Osinski et al., 2015). This impactite has formed cliffs exceeding 40 m in height in some areas, while being absent in others, resulting in a direct overlay of clast-rich impact melt rocks on the fractured basement rocks. Melt particles that are aligned parallel to the upper melt rock contact have been documented in several locations within the impact structure, along with melt-rimmed lithic clasts (Osinski et al., 2015). The presence of melt-rimmed lithic clasts is often associated with an airborne mode of transportation (Stöffler, 1977). In this case however, these impactites could not have been airborne as they are located below the impact melt sheet. Overlaying this unit are impact melt rocks, that plot predominantly within the field of trachyandesites with a few andesite outliers (Rosa, 2011; Tolometti et al., 2018). These impact melt rocks are characterized by a more coherent structure than the underlying breccia, a lower clast content, and a variation in colour from red to greyish purple (Phinney et al., 1978; Simonds et al., 1978). The base of the impact melt rock sequence begins with a clast-rich fine-grained impact melt rock that has formed cliffs up to 35 m thick in certain regions (Osinski et al., 2015). The transition upwards from the clast-rich impact melt rock leads to the clast-poor variety of fine-grained impact melt rock with contact between the two units varying from gradual to abruptly gradational. The uppermost impactite layer comprises the clast-poor medium- to course-grained impact melt rock, which is located on the most elevated points of the majority of the ring islands and can be up to 85 m thick (Osinski et al., 2015; Simonds et al., 1978).

### 2.2.2 Hydrothermal Alteration

The presence of hydrothermal alteration has been acknowledged by prior research at the Clearwater West impact structure, with quartz being the most common hydrothermal deposits (Bostock, 1969; Jaimes Bermudez, 2023; Kerrigan & Osinski, 2015; Osinski et al., 2015; Phinney et al., 1978; Rosa, 2011). Glasses and pyroxenes replaced by various clays were documented, along with abundant hematite, indicating the occurrence of hydrothermal processes within the impact breccias and impact melt rocks (Bostock, 1969). The clays identified in the matrix of melt-bearing breccias throughout the impactite sequence were characterized as magnesium-rich, calcium-, aluminium- and

potassium-poor saponites, formed through the alteration of sub-micron glass clasts (Allen et al., 1982; Phinney et al., 1978). Eberl et al., (1978) showed that these types of clays can start combining with talc to create mixed layers when temperatures reach around 500°C, thus providing an approximation of the highest temperature at which these clays can form. Furthermore, micrometer-sized hematite associated with hydrothermal alteration have been observed in the matrix of fine-grained impact melt rocks, contributing to the red hue of the rocks (Allen et al., 1982; Phinney et al., 1978). Other alterations involving hematite and ilmenite, displaying diverse textures, have been associated with sub-solidus oxidation processes of primary titanomagnetite (Rosa, 2011). Additionally, fractures filled with titanium-free hematite have also been reported. Investigations have revealed the presence of quartz-filled vugs (up to around 20 cm in diameter) and amygdaloidal structures filled with quartz and clays (between 1 mm and 5 cm in diameter), with quartz crystals growing from the rims to the center of these cavities (Jaimes Bermudez, 2023; Kerrigan & Osinski, 2015). A distinctive outcrop within the central islands with approximately 1 mm-sized pyrite-filled cavities and a yellow fibrous iron-oxide covering the surface of the basement rocks were also documented (Kerrigan & Osinski, 2015).

More recently, hematite was observed as a replacement of titanomagnetite, as pervasive acicular crystals, as crystals growing within amygdules, and as colloform bands in veins associated with goethite and quartz (Jaimes Bermudez, 2023). Talc and saponite were primarily found within amygdules containing hematite and quartz crystals, as well as in reaction rims surrounding quartz vugs. Jaimes Bermudez (2023) concluded that there were three distinct alteration stages: 1) a high-temperature alteration stage (over 500°C) characterized by the oxidation of primary igneous titanomagnetite and the precipitation of pervasive acicular hematite crystals in the fine-grained impact melt rocks; 2) a main alteration stage (300°C to 100°C) where amygdules containing talc, saponite, quartz, and hematite formed, colloform bands of hematite and quartz developed within veins, and the precipitation of pervasive acicular hematite crystals continued; and 3) a late alteration stage (below 100°C) where more quartz and goethite precipitated. Although addressed in previous studies, details regarding hydrothermal alteration at the Clearwater West impact structure remains an area of limited knowledge and requires further exploration. A

comprehensive investigation surrounding the textural and geochemical data is still lacking, leaving gaps in the understanding of the extent, distribution, and evolution of the hydrothermal system. Research carrying out fluid inclusion microthermometry and gas analysis in quartz vugs is therefore necessary to further constrain the temperatures of formations and salinities, and confirm previous results (Jaimes Bermudez, 2023).

## 2.3 Methods

All samples in this study were collected by Mary Kerrigan and Dr. Gordon Osinski on the 2014 joint Canadian-US-UK expedition at the Clearwater West impact structure (WCIS-14-#). This collaborative expedition was conducted as part of the Field Investigations to Enable Solar System Science Exploration (FINESSE) project, affiliated with NASA's Solar System Exploration Research Virtual Institute (SSERVI). Out of the 300+ samples collected during this exhibition, 11 hand samples with large impactite-hosted quartz vugs were chosen to be analyzed. Quartz vugs with fluid inclusions, associated with hydrothermal systems, were the primary targets of this study. All 11 samples were collected from the interior ring of islands. More specifically, this study focuses on quartz vugs from the Lepage, Kamiskutanikaw, and Tadpole islands. Thick sections (≥100 μm) and thin sections (~30 μm) from all 11 hand samples were prepared (cut and doubly polished) in the Thin Section Lab at the Department of Earth Sciences at Western University. Descriptions of each sample can be found in Appendix A. All samples were found within fine-grained impact melt rocks and clast-rich melt rocks described by Bostock (1969), Kerrigan & Osinski (2015), Phinney et al. (1978), Rosa (2011), Simonds et al. (1978), and Tolometti et al. (2018).

**Table 2.1 Clearwater West impact structure sample descriptions.**

| Sample # | Locality | Northing | Easting | Lithology |
|---|---|---|---|---|
| WCIS-14-**MK-029A** | Kamiskutanikaw | 539194 | 623288 | Clast-rich melt rock |
| WCIS-14-**MK-029B** | Kamiskutanikaw | 539194 | 623288 | Clast-rich melt rock |
| WCIS-14-**MK-033** | Kamiskutanikaw | 540242 | 623225 | Fine-grained melt rock |
| WCIS-14-**MK-035A** | Kamiskutanikaw | 540017 | 623229 | Fine-grained melt rock |
| WCIS-14-**MK-036A** | Kamiskutanikaw | 539985 | 623228 | Fine-grained melt rock |
| WCIS-14-**MK-036B** | Kamiskutanikaw | 539985 | 623228 | Fine-grained melt rock |
| WCIS-14-**MK-046** | South East Island | 537656 | 622552 | Clast-rich melt rock |
| WCIS-14-**MK-053** | South East Island | 536545 | 622476 | Fine-grained melt rock |
| WCIS-14-**MK-070** | Lepage | 535311 | 623676 | Clast-rich melt rock |
| WCIS-14-**OZ-008** | Tadpole Islands | 523700 | 623356 | Clast-rich melt rock |
| WCIS-14-**OZ-020** | Lepage | 535732 | 623586 | Clast-rich melt rock |

### 2.3.1 Optical Microscopy

Doubly polished thick sections from all 11 hand samples were used for optical microscopy. They were analyzed under reflected and transmitted light using a Nikon Eclipse LV100POL compound petrographic microscope equipped with a 12 Mpx Nikon DS-Ri1 digital camera at the Department of Earth Sciences' Optical Microscopy Laboratory at the University of Western Ontario.

### 2.3.2 Electron Microprobe Analysis

Polished thick and thin sections were carbon-coated and inserted into the state-of-the-art JEOL JXA-8530F hyperprobe field-emission electron microprobe analyzer (EMPA) at the Earth and Planetary Materials Analysis (EPMA) Laboratory at the University of Western Ontario for cathodoluminescence imaging. Qualitative assessments were made using backscattered electron (BSE), secondary electron (SE), and cathodoluminescence (CL) imaging analysis techniques to investigate micro-textures, as well an energy dispersive (EDS) and wavelength dispersive (WDS) spectroscopy to determine alteration phases. CL maps were obtained under a current of 100 nA and a step size of 30 μm. The analytical conditions for spot analysis of quartz is summarized in Table 2.2. Electron

microprobe spot analyses operated under a current of 50 nA, an accelerating voltage of 20 kV, and a beam size of 20 μm.

**Table 2.2 Electron microprobe spot analyses operating conditions for quartz**

| Element | Standard | Crystal | Detection Limit (ppm) | Peak counting time (s) |
|---|---|---|---|---|
| Si | quartz | TAP | 147 | 20 |
| Al | corundum | TAP | 79 | 50 |
| Na | albite | TAP | 77 | 50 |
| Ti | rutile | PETJ<br>PETH<br>PETL | 52 | 200 |

### 2.3.3 Fluid Inclusion Microthermometry

A Linkham THMSG600 heating-freezing stage (with a temperature range of -195°C to 600°C) mounted on an Olympus BX53F petrographic microscope was used for fluid inclusion microthermometry analysis at the Magmatic-Hydrothermal Laboratory at the University of Western Ontario. All carbon-coated doubly polished thick sections were floated using an acetone bath then separated from the slides and inserted (in small pieces) into plastic bags with the use of tweezers. With the use of tweezers, the small pieces (≤1cm) were then placed on the sapphire slide inside the stage. The heating-freezing stage was calibrated by measuring the ice melting temperature of synthetic inclusions of pure $H_2O$ ($T_{m(ice)} = 0°C$) and $H_2O$–$CO_2$ inclusions ($T_{m(CO_2)} = -56.6°C$) entrapped in quartz, with an error of +/- 0.1°C. Two-phase (liquid-vapour) fluid inclusions from each sample were located, then heated to find homogenization temperatures ($T_h$), cooled to find freezing temperatures ($T_f$), and reheated again to find melting temperatures ($T_m$). A 1°C/min heating rate was applied to all heating and cooling experiments for observation precision. Salinity (wt% $NaCl_{eq}$) of the fluid inclusions were calculated using the $T_m$ and the equation (1) after Bodnar, 1993, where $\theta$ is the $T_m$ in degrees Celsius:

$$\text{Salinity} = 1.78\theta - 0.0442\theta^2 + 0.000557\theta^3 \quad (1)$$

### 2.3.4 Mass Spectrometry

A residual-gas quadrupole mass spectrometer system (QMS), custom built by Dr. Blamey, from the Fluid Inclusion Gas Laboratory at the University of Western Ontario was used to quantitively analyze the composition of the gases trapped within the fluid inclusions of the 11 samples. To reduce surface organic contamination, small pieces (under 5 mm in diameter and ranging from milligram to gram scale) of quartz from each hand sample were soaked in 3% hydrogen peroxide for 10 minutes, rinsed with deionized water, and then left to dry at room temperature. The crush-fast scan (CFS) method, described by Norman & Moore (1997), Norman et al. (2002), Norman & Blamey (2001), and Parry & Blamey (2010), was applied for the extraction and analysis of volatiles, allowing for detection of trace amounts with high sensitivity (Blamey, 2012; Blamey et al., 2012). The dried samples were placed into a crushing chamber and subjected to vacuum conditions (approximately $10^{-8}$ Torr) and the main chamber was heated for 72 hours. The crushing process occurred incrementally, releasing bursts of mixed volatiles that were individually detected by the mass spectrometer. Each burst of volatiles originated from a typical sample size of approximately 150 ml (consisting of a few quartz grains) and amounted to 4 to 10 bursts, releasing up to $2 \times 10^{-11}$ mol of non-aqueous volatiles. These volatiles remained in the vacuum chamber for 8 to 10 scans conducted by the analyzer before being removed by the vacuum pump. The method utilized does not require the use of a carrier gas, and the volatiles are not isolated from one another, but are instead simultaneously released into the chamber. $H_2$, He, $CH_4$, $N_2$, $O_2$, Ar, and $CO_2$ were the gases analyzed for in each individual crush. This analysis was carried out using a Pfeiffer Prisma residual-gas quadrupole mass spectrometer (QMS) operating in fast-scan, peak-hopping mode at room temperature.

A matrix inversion was used to convert the current detected at each mass into a quantitative analysis (Isenhour & Jurs, 1979; Norman & Sawkins, 1987). This matrix takes into account the sensitivity factors for each gas as measured by Dr. Blamey. The gas to water ratio used for calibration is based on the Hansonburg fluorite standard, HF-1, described by Norman et al. (1985). Although it is typical for geochemists to consider $2\sigma$ as the confidence limit, the detection limit for this study employed a $3\sigma$ value (a quarter

of a ppm), to verify that the gas bursts contained a concentration greater than zero (Blamey et al., 2015). Total errors were calculated using seven components: blank compositions, background instrument noise; error in linear range; uncertainty in gas composition; interferences in measuring gas species; analytical errors in measuring current; and the conversion of the mass spectrometer current into mols which applies only to the summary data tables (Appendix C) (Blamey et al., 2015). Further details of this study's methods for conducting quantitative fluid inclusion gas analysis by mass spectrometry are described in Jones & Kesler (1992), Norman & Blamey (2001), Norman & Sawkins (1987), and Parry & Blamey (2010).

## 2.4 Results

### 2.4.1 Petrography

Various features and textures were observed under polarized light. In addition, fluid inclusion trails and quartz zoning patterns are evident. Planar deformation features (PDFs) are not present, confirming that the quartz mineralization occurred after the initial impact event. This is consistent with all vugs being present in impact-generated melt rocks. Quartz vug growth begins at the outer edges (at contacts with impactites) then grows inwards (Figure 2.2). Images show quartz crystals with angular edges, indicative of authigenic quartz precipitation in the form of individual crystals and secondary overgrowths. Colour and monochrome cathodoluminescence maps show quartz crystals with considerable oscillatory euhedral growth zones and some subhedral growth zones that are not visible in BSE or SE images (Figures 2.3 & 2.4). The thickness of these growth bands varies, with thinner, irregular, and darker bands near the vug walls and thicker, brighter ones towards the vug center (Figure 2.4A). These textures were also seen and described by Jaimes Bermudez (2023). Reverse zoned (bright CL outer rims with dark CL core regions), normal zoned (bright CL core with dark CL rim), and unzoned (lack of distinct zoning pattern with either dark or bright CL intensity) quartz crystals are all present. WDS analysis shows that the main trace elements present in the quartz are sodium (average of 93 ppm) and titanium (average of 76 ppm) (Appendix A). Titanium levels are relatively consistent throughout the samples and correlate with darker CL bands; however, sodium levels tend to increase towards the centres of vug samples (rim

average of 23 ppm, middle average of 44 ppm, centre average of 170 ppm), suggesting that the hydrothermal fluid became progressively enriched in sodium over time.

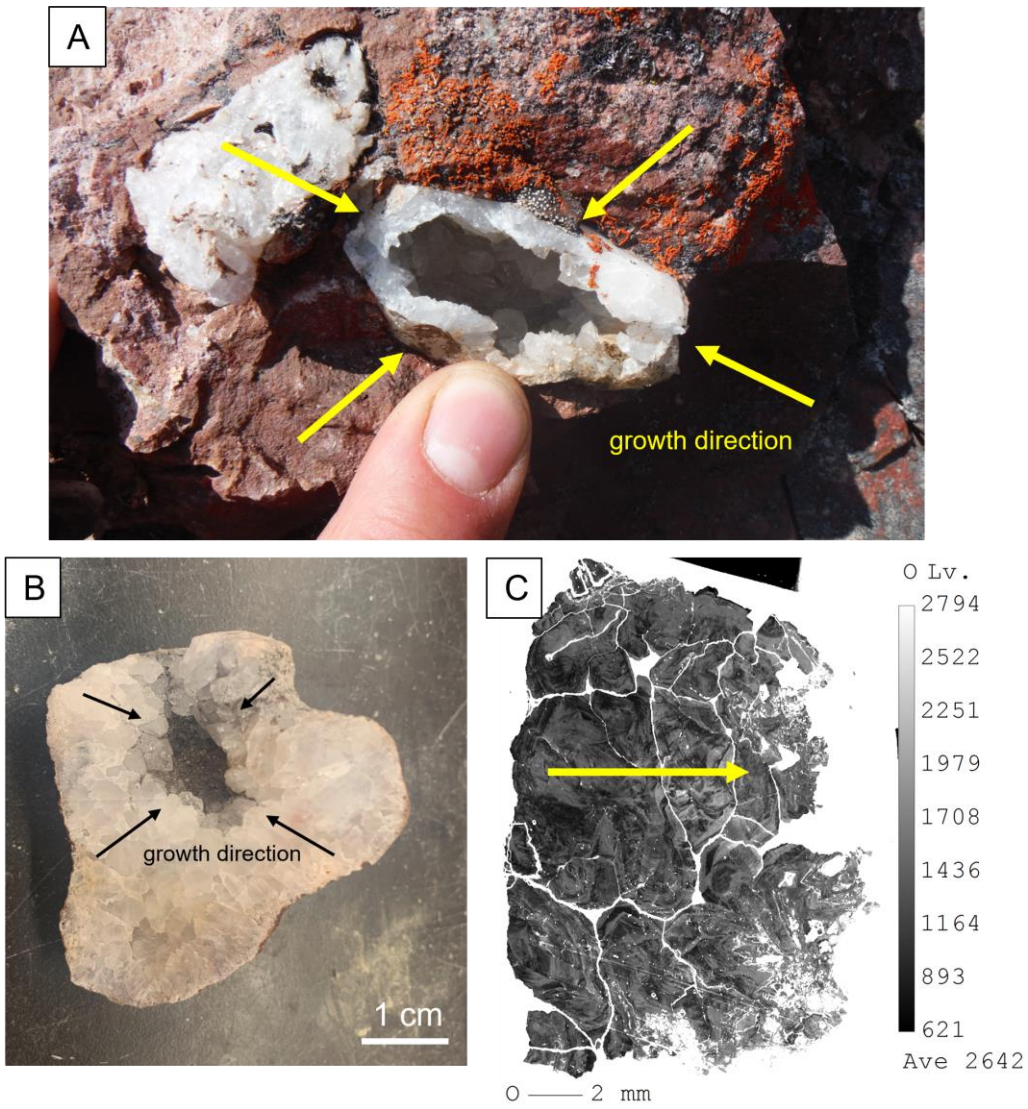


**Figure 2.2 Growth direction of quartz vugs found at the Clearwater West impact structure. A) In-situ quartz vug showing inwards growth direction with thumb for scale. B) Hand sample of WCIS-14-MK-036 vug showing growth direction inwards. C) CL image of WCIS-14-MK-035 vug showing growth direction inwards with the right side being the centre of the vug.**

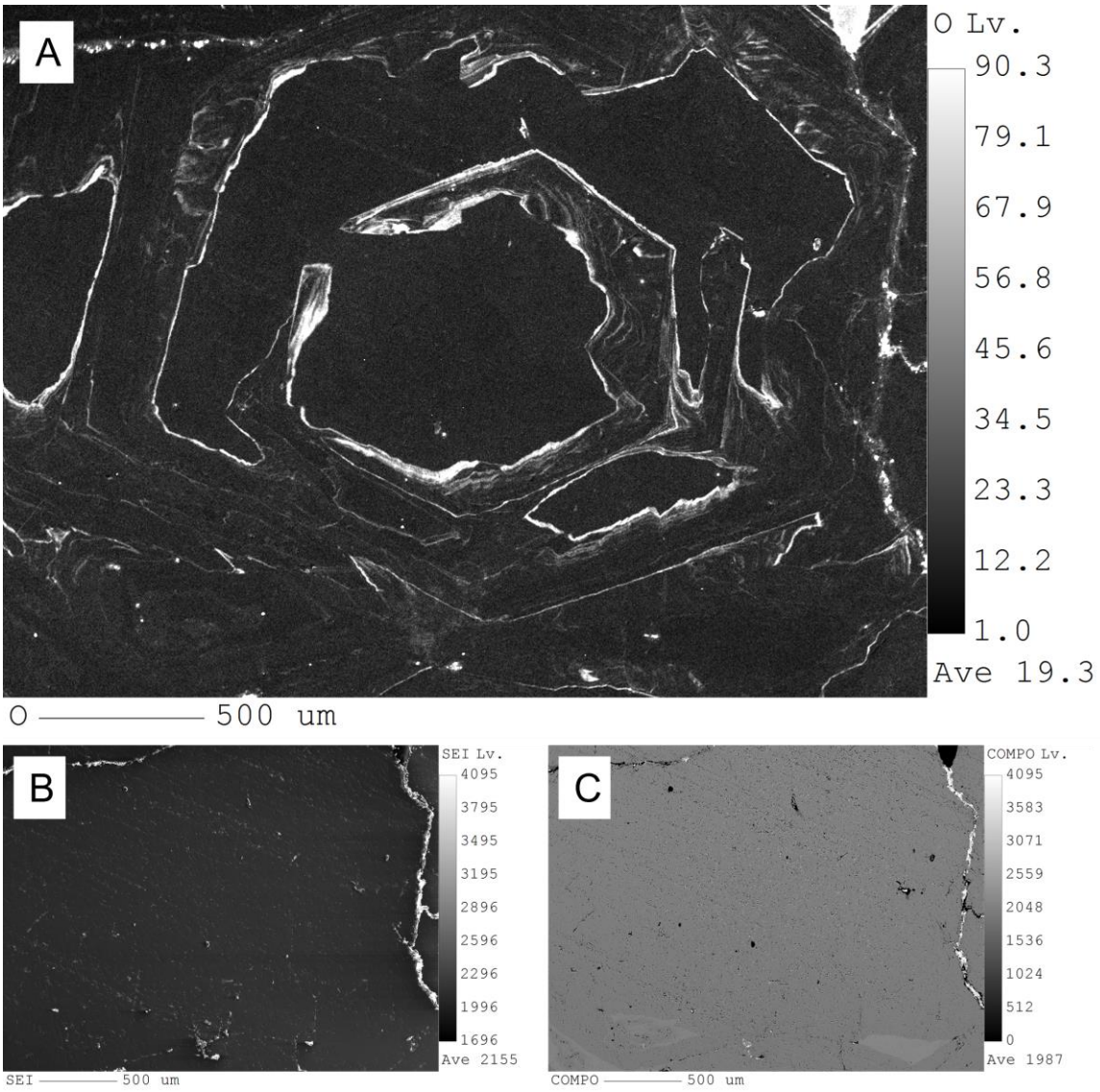


**Figure 2.3 Electron microprobe images of the same spot within quartz vug sample WCIS-14-MK-029A. (A) CL image showing euhedral oscillatory growth zones. (B) and (C) show the same spot in SE and BSE images, respectively. Note the textural features visible in CL and not SE or BSE.**

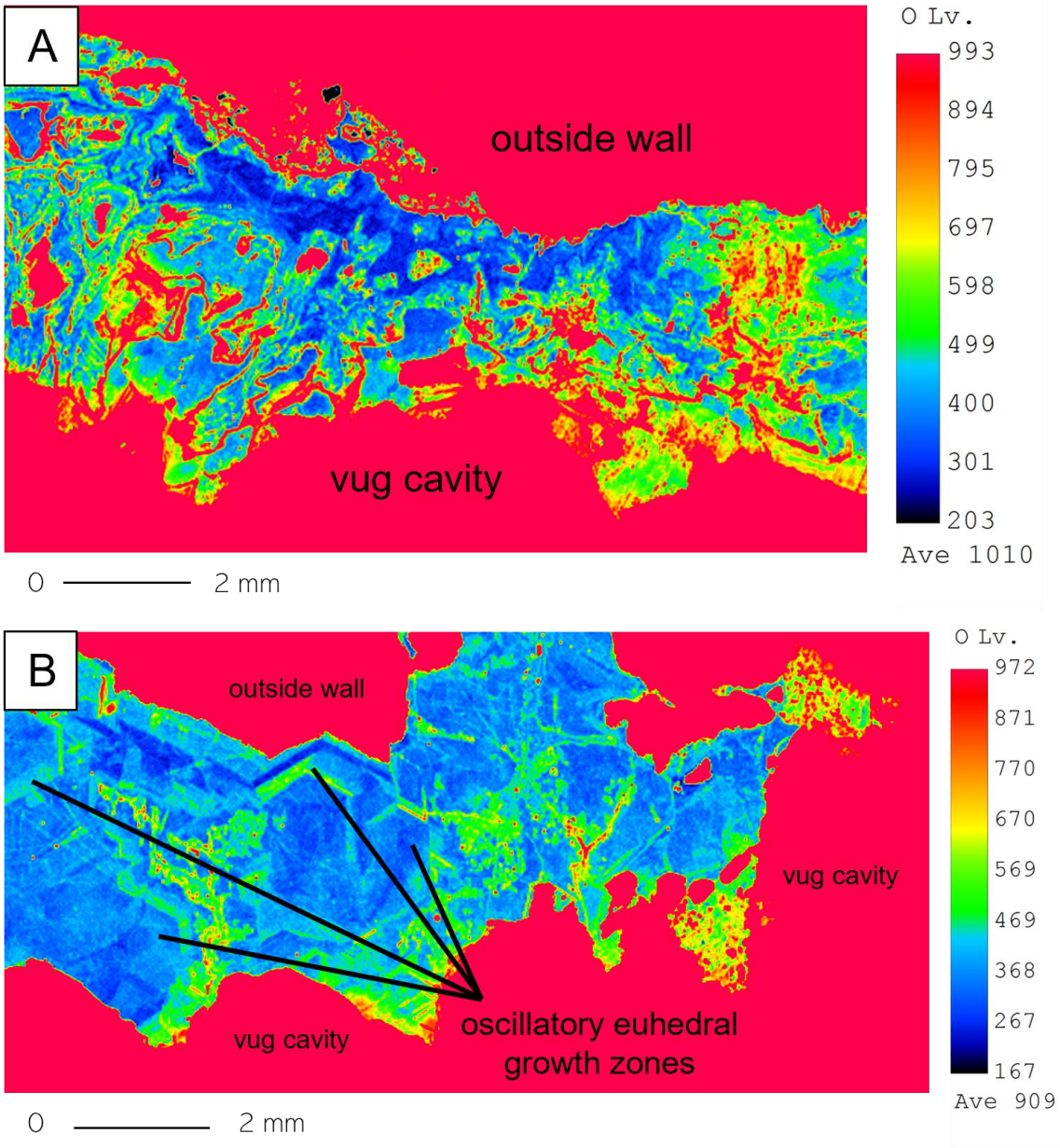


**Figure 2.4 Colour CL images of quartz vugs showing microtextures. A) WCIS-14-MK-029 sample image showing brighter CL intensities towards the vug cavity and darker CL intensities towards the outside wall (contact with host impactite). B) WCIS-14-MK-053C sample image showing oscillatory euhedral growth zones with brighter CL intensities towards the vug cavity.**

### 2.4.2 Fluid Inclusion Microthermometry

Measurements of homogenization ($T_h$), freezing ($T_f$), and final melting ($T_m$) temperatures in °C were made for 80 fluid inclusions in 11 quartz vug surface samples from the West Clearwater impact-generated hydrothermal system (Appendix B). Fluid inclusions were rare in most samples or too small to analyse, however, samples MK-053, OZ-008, and OZ-020 have plentiful fluid inclusions, allowing for more data collection than other samples with fewer fluid inclusions. Fluid inclusions typically ranged from 5 to 20 μm, with few rare inclusions reaching up to 35 μm. During heating runs, many smaller fluid inclusions decrepitated due to the build-up of internal pressure. The composition of the fluid inclusions is predominantly NaCl–$H_2O$ (aqueous), but rare NaCl–$H_2O$–$CO_2$ composition fluids were also found. Fluid inclusions are mostly primary type 1 (L + V) inclusions at room temperature (Figure 2.5), with fluid inclusions becoming more fluid-dominant (L-type) towards the centre of the vugs and more vapour-dominant (V-type) towards the outer wall.

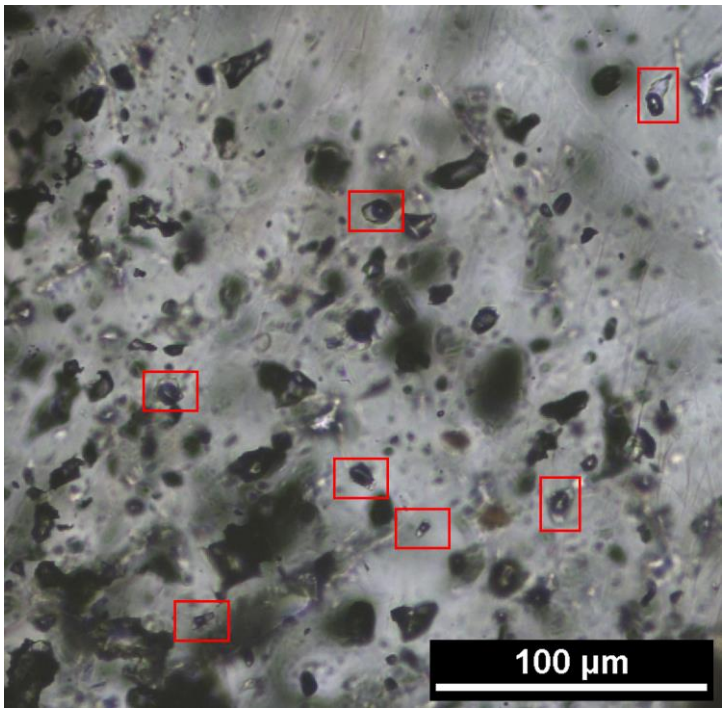


**Figure 2.5 Quartz-hosted fluid inclusions in sample WCIS-14-MK-053 viewed with 40x lens in transmitted light under the microscope. Primary type 1 (liquid + vapour) fluid inclusions used for microthermometry are boxed in red.**

The homogenization temperature ($T_h$) measurement results of aqueous quartz fluid inclusions cover a wide range from approximately 100°C to over 500°C, with 30 of the 80 fluid inclusions homogenizing over 400°C (Figure 2.6) (Appendix B). Fifty fluid inclusions homogenized between 100°C and 400°C (Figure 2.6), with 3 different maximum peaks. The ice melting temperature measurements range from approximately -30°C to -1°C, corresponding to fluid salinities between 2 and 30 wt% $NaCl_{eq}$, with most samples falling between 2 and 14 wt% $NaCl_{eq}$ (Bodnar, 1993). Lastly, the ice freezing temperature measurements range from approximately -70°C to -25°C.

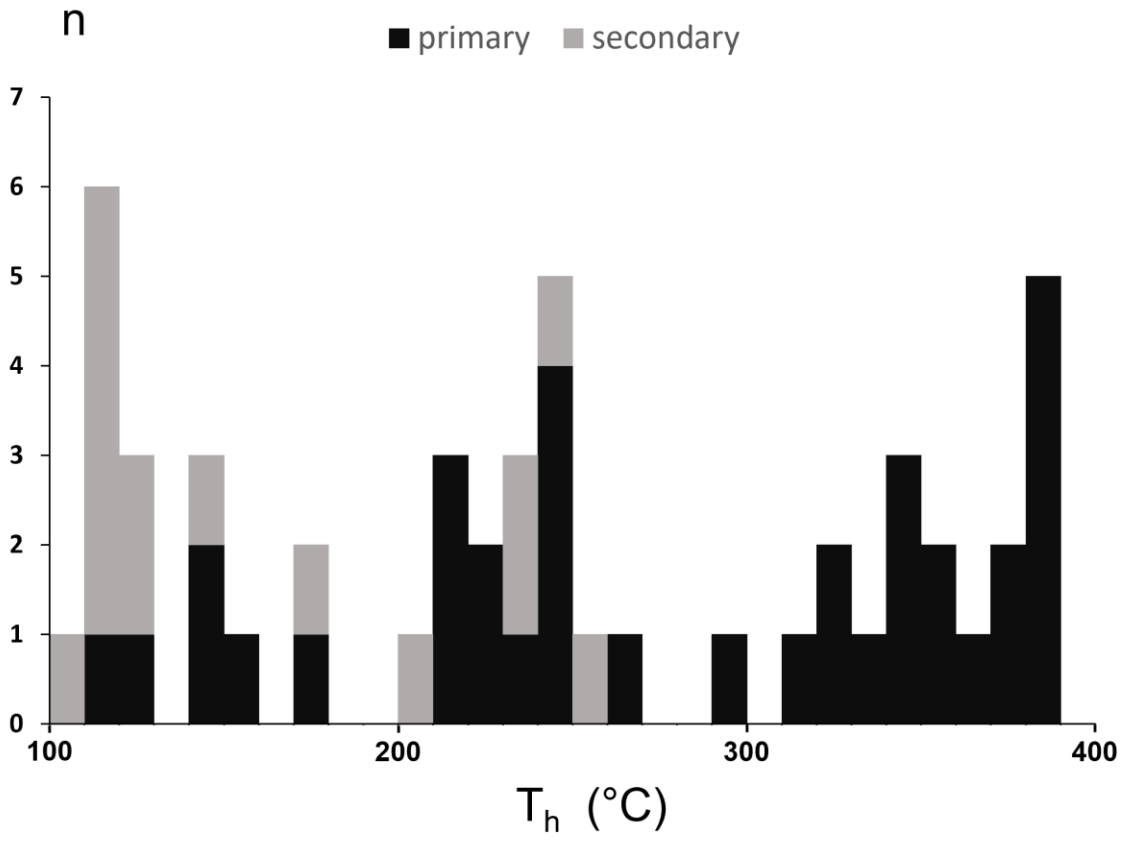


**Figure 2.6 Histogram of the quartz-hosted aqueous ($H_2O$–NaCl) fluid inclusion homogenization temperatures ($T_h$) in the Clearwater West impact structure. Primary fluid inclusions are shown in black while secondary fluid inclusions are shown in grey. Note that there are also 30 primary fluid inclusions with $T_h$ values above 400°C.**

Of the 80 fluid inclusions measured, 15 are secondary, reflecting fluids that circulated within cracks and fractures of post-mineralized quartz. The other 65 fluid inclusions are primary, reflecting fluids that circulated during the quartz mineralization. Within an individual vug, it is notable that the homogenization temperatures of primary inclusions in the exterior of the outer wall regions are all above 384°C, with the majority being above 420°C (Table 2.3). In the middle regions, homogenization temperatures of primary inclusions are between 246 and 382°C, while in the centre region, results are between 120 and 243°C. Secondary inclusions have much lower homogenization temperatures (Figure 2.6): homogenization temperatures in the outer wall region are between 124 and 253°C (9 data points), between 111 and 120°C in the middle region (5 data points), and 105°C (1 data point) in the centre of the vugs. Hence, when moving towards the centre of these features, the homogenization temperature ($T_h$) measurements of primary and secondary fluid inclusions decrease (Figure 2.7).

**Table 2.3 Primary and secondary fluid inclusion microthermometry range results in outer wall, middle, and centre regions of all samples.**

| Inclusion Type | | Primary | | | Secondary | | |
|---|---|---|---|---|---|---|---|
| Location | | Outer Wall | Middle | Centre | Outer Wall | Middle | Centre |
| $T_h$ (°C) | Max | 550+ | 381.8 | 242.5 | 252.9 | 119.5 | 104.5 |
| | Min | 383.6 | 246.1 | 119.5 | 123.5 | 111.1 | 104.5 |
| $T_f$ (°C) | Max | -30.9 | -26.8 | -22.9 | -26.8 | -41.6 | -42.4 |
| | Min | -69.8 | -48.9 | -59.9 | -72.9 | -71.7 | -42.4 |
| $T_m$ (°C) | Max | -1.6 | -2.1 | -15.1 | -30.1 | -30.7 | -22.2 |
| | Min | -32.6 | -10.1 | -4.2 | -6.9 | -11.9 | -22.2 |
| NaCl (wt%) | Max | 30.4 | 14.0 | 18.7 | 28.7 | 29.1 | 23.8 |
| | Min | 2.7 | 3.6 | 6.7 | 10.4 | 15.9 | 23.8 |

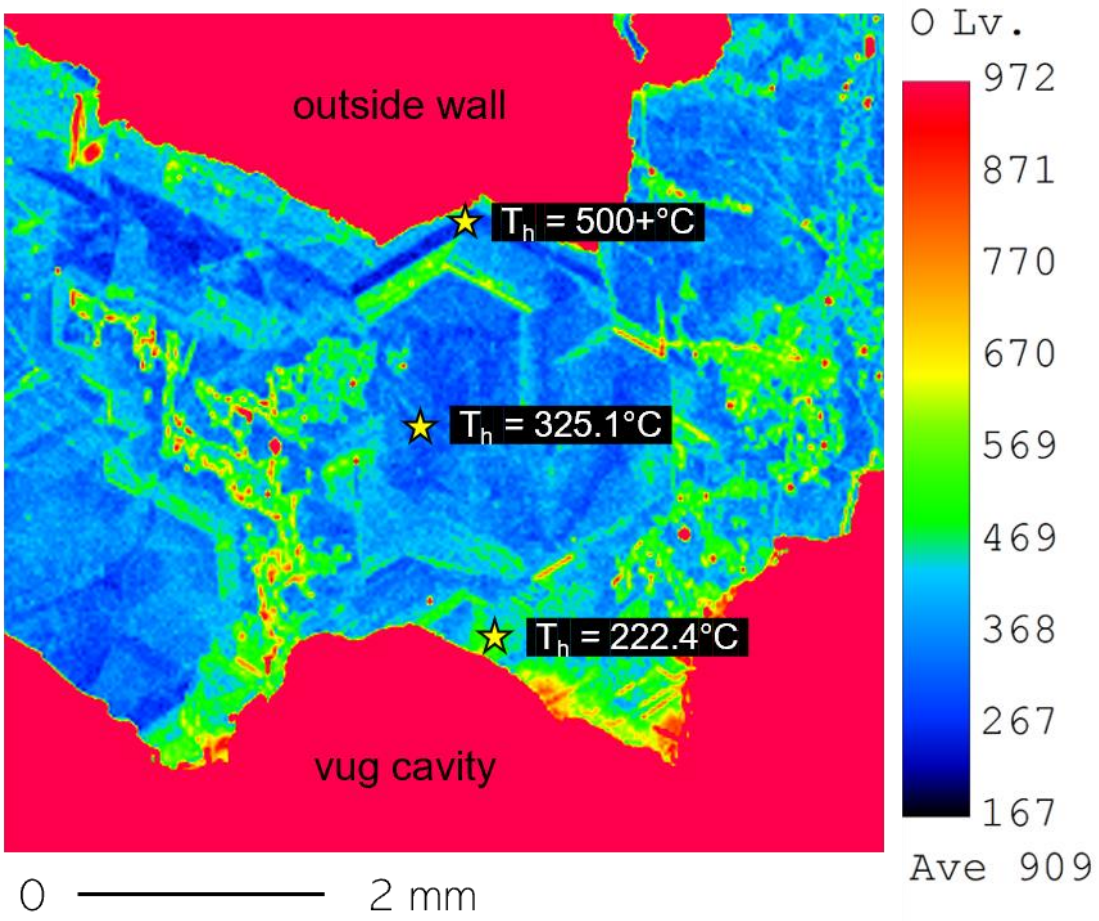


**Figure 2.7 CL image of sample WCIS-14-MK-053 showing three different locations of fluid inclusions (yellow stars) moving from the outside wall (contact with impactite) to the vug cavity. Homogenization temperatures collected during microthermometry are highlighted in black beside the associated fluid inclusion.**

### 2.4.3 Mass Spectrometry

In most gas analyses, water ($H_2O$) makes up between 85-99 mole%; however, this study focused on inorganic species, and thus, the non-aqueous key inorganic species are reported. The primary dissolved gases present are nitrogen ($N_2$), carbon dioxide ($CO_2$), and oxygen ($O_2$), with minor concentrations of methane ($CH_4$), argon (Ar), and other organic compounds. Argon is essentially inert and generally unaffected by biological activity, except under extremely high-pressure conditions (e.g., Abraini et al., 1998). Although argon can be generated by K-bearing minerals above the closure temperature

for argon systematics, gas ratios such as $N_2$/Ar and $O_2$/Ar can still be valuable in identifying variations in gases influenced by biological activity (Blamey et al., 2016). Furthermore, argon can also serve as a normalizing, unreactive gas species for geochemical interactions.

The majority of the samples have oxygen levels that are lower than the atmospheric value, with a few data points (MK-36-B & OZ-020) falling above atmospheric values (Figure 2.8A). There is no obvious correlation between oxygen depletion and $N_2$/Ar levels. Helium levels are around or above atmospheric values with some data points (MK-053 & OZ-008) with very high levels of helium. The highest levels of helium are associated with the highest $N_2$/Ar ratios. Nitrogen levels are similar to atmospheric values, with some data points much higher and others much lower. Argon levels range from around the same values of atmospheric levels to very depleted (Figure 2.8B). Low levels of argon are inversely correlated with helium. Methane levels range from atmospheric values to very elevated levels and are inversely correlated with nitrogen (Figure 2.8C).

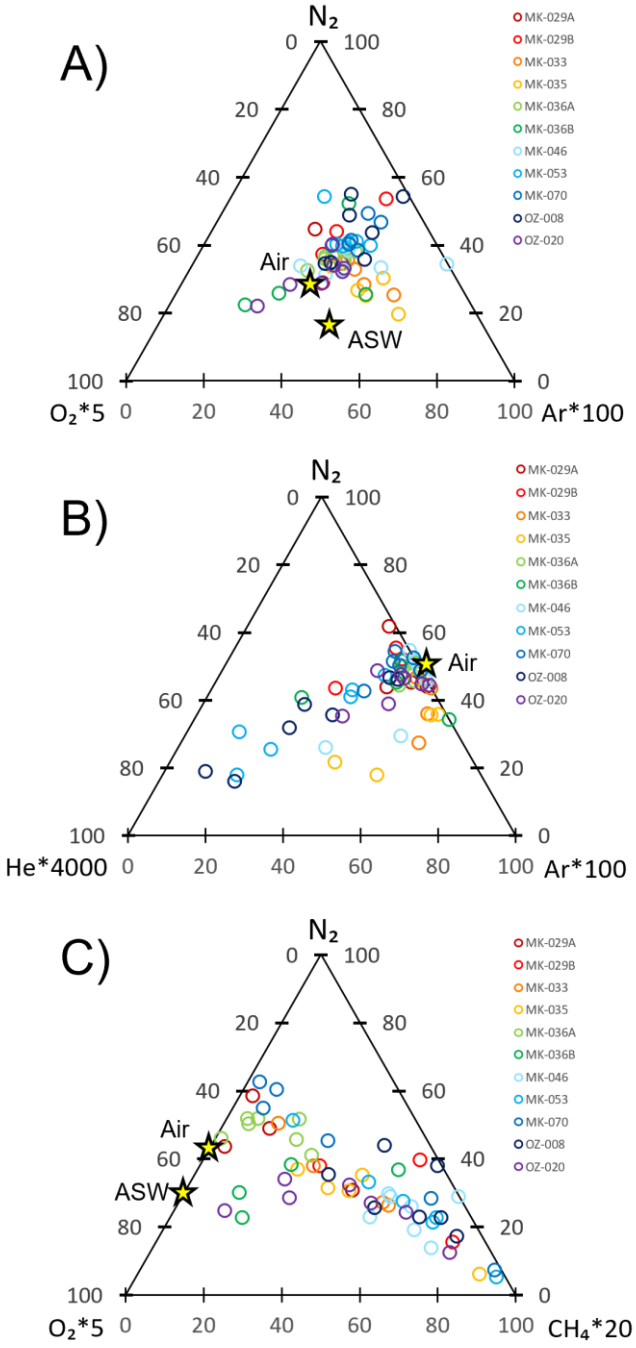


**Figure 2.8 Mass spectrometry gas composition data in ternary diagrams after Blamey et al. (2016). The yellow stars represent the atmospheric and ASW (air-saturated water) gas ratios. A) $O_2$–$N_2$–Ar ternary plot. B) He–$N_2$–Ar ternary plot. C) $O_2$-$N_2$-$CH_4$ ternary plot.**

Mass spectrometry gas analysis data plotted in ternary diagrams following the procedures of Giggenbach (1986) indicate that the fluid inclusion gases most resemble air and air saturated water (ASW) $N_2$–Ar–He and $N_2$–Ar–$CH_4$ levels, with some evolved water (Figure 2.9). Fluid inclusion chemistry is consistent with a hydrothermal system comprising mixed evolved and meteoric waters. However, some $N_2$/Ar values are greater than ASW, indicating a possible mixture with a fluid of magmatic source. These results are further amplified by the plotted data in the meteoric versus magmatic fluid plots after Blamey & Norman, 2002 and Norman & Moore, 1999 (Figure 2.10). Data shows high levels of oxidation and plots within the fields of shallow meteoric, magmatic, and evolved fluids. However, the original plot in Figure 2.10B was set up for geothermal calc-alkaline magmatic environments (Norman & Moore, 1999), which does not exist in the setting of Clearwater West Lake impact structure. Hence, the data points plotting in the calc-alkaline magmatic fluid box are not actually showing calc-alkaline magmatic environments, but instead showing that there is contamination of higher $N_2$/Ar and lower Ar/He ratios in the meteoric water in the fluid inclusions. $N_2$/Ar ratios vary from 12.5 to 336.8, with the majority ranging from 80 to 120, and an average of 108 (Figure 2.11). Meteoric fluids (or ASW) typically have an $N_2$/Ar ratio of around 38, whereas magmatic fluids have $N_2$/Ar ratios that well exceed 100 (Norman & Musgrave, 1994).

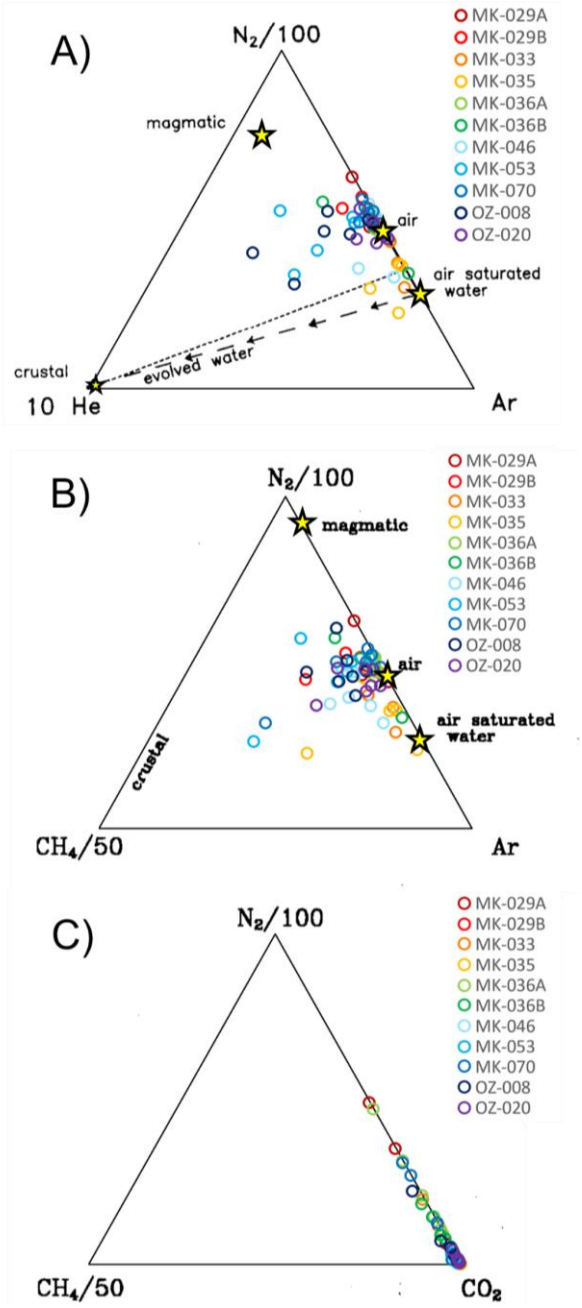


**Figure 2.9 Mass spectrometry gas composition data in a ternary diagrams after Giggenbach (1986). The positions highlighted by stars represent the compositions linked with the principal sources of these elements within geothermal fluids. A) An $N_2$–Ar–He diagram. The dashed line accompanied by arrows depicts the alteration in the composition of meteoric fluids as they amass radiogenic He beneath the Earth's surface and become more evolved fluids. B) An $N_2$–Ar–$CH_4$ diagram. C) An $N_2$–$CO_2$–$CH_4$ diagram.**

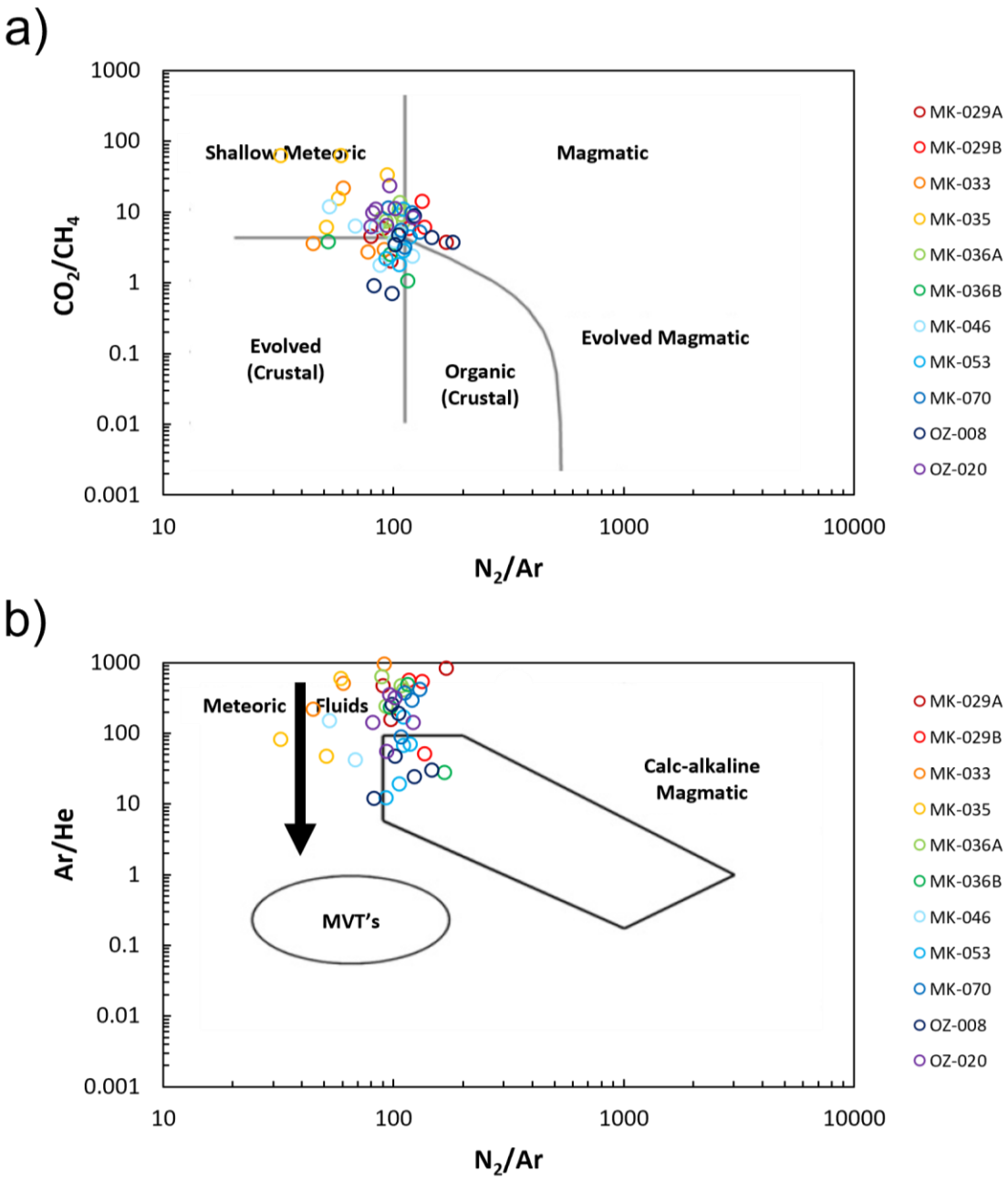


**Figure 2.10 Plots used to discriminate meteoric versus magmatic fluids. a) $CO_2/CH_4$ versus $N_2/Ar$ plot after Norman & Moore (1999). b) $N_2$–Ar–He plot after Blamey & Norman (2002).**

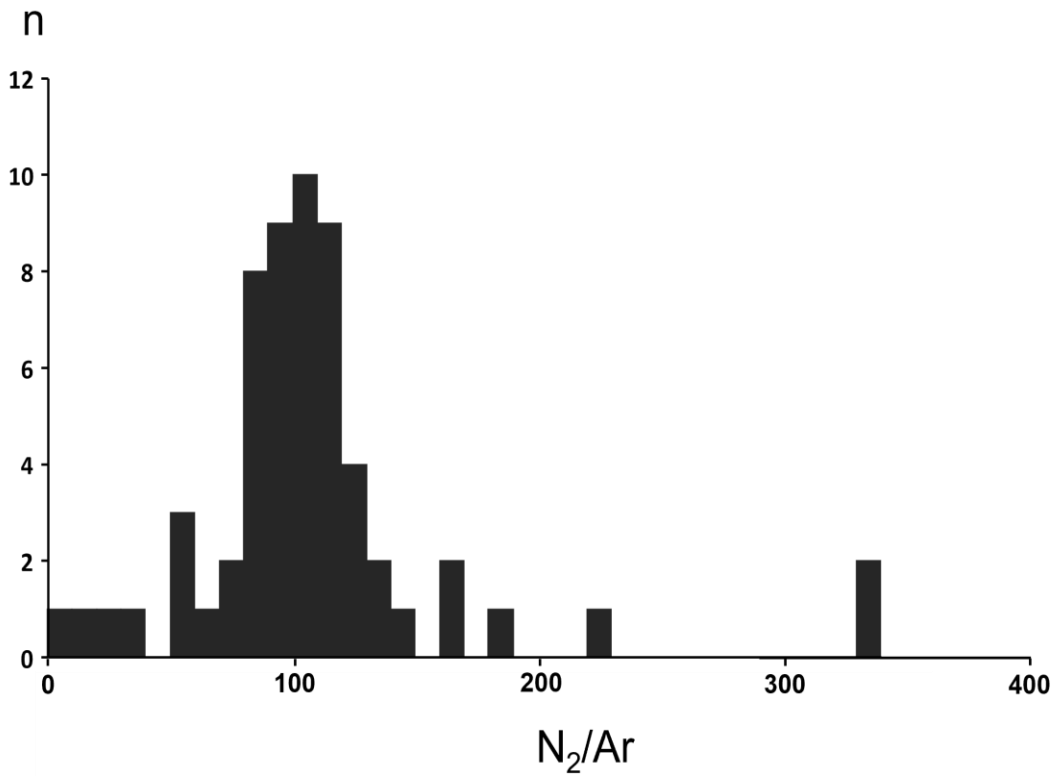


**Figure 2.11 Histogram of the $N_2$/Ar ratios gas analysis results from Clearwater West impact structure samples.**

## 2.5 Discussion

### 2.5.1 Quartz Growth and Thermochronology

Based on optical microscopy and electron microprobe analysis (EMPA), it is clear that quartz mineralization occurred in the impact-generated hydrothermal system at the Clearwater West Lake impact structure. Euhedral quartz crystals, as seen in CL images (Figures 2.3 & 2.4), grow from solutions with gradually evolving conditions (Fournier, 1985), such as hydrothermal systems. During the primary mineralization stages, quartz with titanium concentrations lower than 10 ppm typically indicates mineralization temperatures below 350°C (Sun et al., 2021). Titanium concentrations found in this study average at 76 ppm, suggesting high mineralization temperatures. CL images show evidence of pauses and breaks in the quartz mineralization, indicating that the process of quartz crystal growth was not uniform or continuous throughout the system's history.

Instead, there were periods of steady and slow crystal growth and episodes where growth was interrupted or paused. This pattern of mineralization suggests fluctuations in the hydrothermal conditions within the impact site. The gradual mineralization indicates times when the hydrothermal fluids were relatively stable, allowing for continuous crystal growth. The breaking or pausing mineralization indicates times when the conditions changed, possibly due to shifts in fluid composition, temperature, or pressure. These changes may have temporarily halted or slowed down the crystal growth process.

As part of this thesis, this study was the first to use fluid inclusions to assess the Clearwater West Lake impact structure. Fluid inclusion microthermometry data in this study shows that there were three stages of quartz mineralization, the first above 384°C, the second between 382 and 246°C, and the last between 243 and 120°C (Table 2.3). These homogenization temperature values decline towards the centre of the quartz vugs with the inclusions becoming more fluid-dominant, indicating that the processes of quartz mineralization persisted as the circulating hydrothermal fluid gradually cooled down over time. Jaimes Bermudez (2023) suggested that quartz vugs formed at conditions in the range of 200 to 300°C, however, fluid inclusion microthermometry results in this study show evidence for quartz mineralization at temperatures exceeding 550°C. Furthermore, the microthermometry results of this study suggest that there was no singular maximum peak (Figure 2.6) in the data, there are 3 broad peaks, suggesting 3 main episodes of quartz formation. During these peaks, quartz mineralization was likely gradual, while the transition to the following generations likely resulted in breaks or pauses in the crystal growth.

### 2.5.2 Fluid Sources

It has previously been suggested that the Clearwater West impact structure formed in a continental setting, in the single content of Pangea (Schmieder et al., 2015). This is supported by our mass spectrometry data and salinity data from fluid inclusion microthermometry, which indicate a meteoric fluid source. There is no evidence for any fluid source from marine water. Volatile mixture compositions originating from one source (Figure 2.12) and from two distinct sources (Figure 2.13) are documented by Norman & Musgrave (1994). Based on the ternary diagrams in Figure 2.12, mass

spectrometry analysis of quartz-hosted fluid inclusions from this study suggests heterogenous trapping of a deep-circulating meteoric fluid that had accumulated $CH_4$, $CO_2$, and He (Figure 2.12b) and a shallow meteoric fluid that had a gas chemistry similar to air and ASW (Figure 2.12d). Based on Figure 2.13 ternary diagrams, mass spectrometry analysis resembles magmatic and shallow circulating meteoric fluids (Figure 2.13a) and shallow circulating meteoric fluids and sedimentary brines (Figure 2.13d). We suggest that the resemblance of this study's mass spectrometry results to magmatic fluid values is likely due to a small contribution of fluids from the crystallizing impact melt sheet. The interaction between the circulating hydrothermal fluid and the residual melt from the initial impact event can lead to the incorporation of magmatic elements and volatiles into the hydrothermal system. Our results confirm a progressive change in fluid inclusion gas chemistry over time from low salinity to relatively high salinity levels.

The differences in $N_2$/Ar ratios observed in Figure 2.11 could stem from a combination of several factors: varying levels of small air bubbles getting trapped within fluid inclusions, the release of nitrogen during the decay of nitrogen-rich biomolecules, or potentially non-biological decomposition of nitrate (Blamey et al., 2016). The majority of the samples have oxygen levels that are lower than the atmospheric value (Figure 2.8A), which could be attributed to the breakdown of organics by confined heterotrophic microorganisms through respiratory processes. If the oxygen depletion is a result of biological activity, this could potentially support a biological process to explain the degradation of nitrogen-containing biomolecules (Blamey et al., 2016). Furthermore, the variability in methane content in relation to $N_2$ and $O_2$ might reflect varying quantities of organic material during the entrapment of fluid inclusions; however, enhancements in this line of research is necessary before arriving at any conclusive interpretation. Alternatively, low oxygen levels could be a result of abiotic chemical reactions within the rock that consumed oxygen, such as a chemically reducing environment.

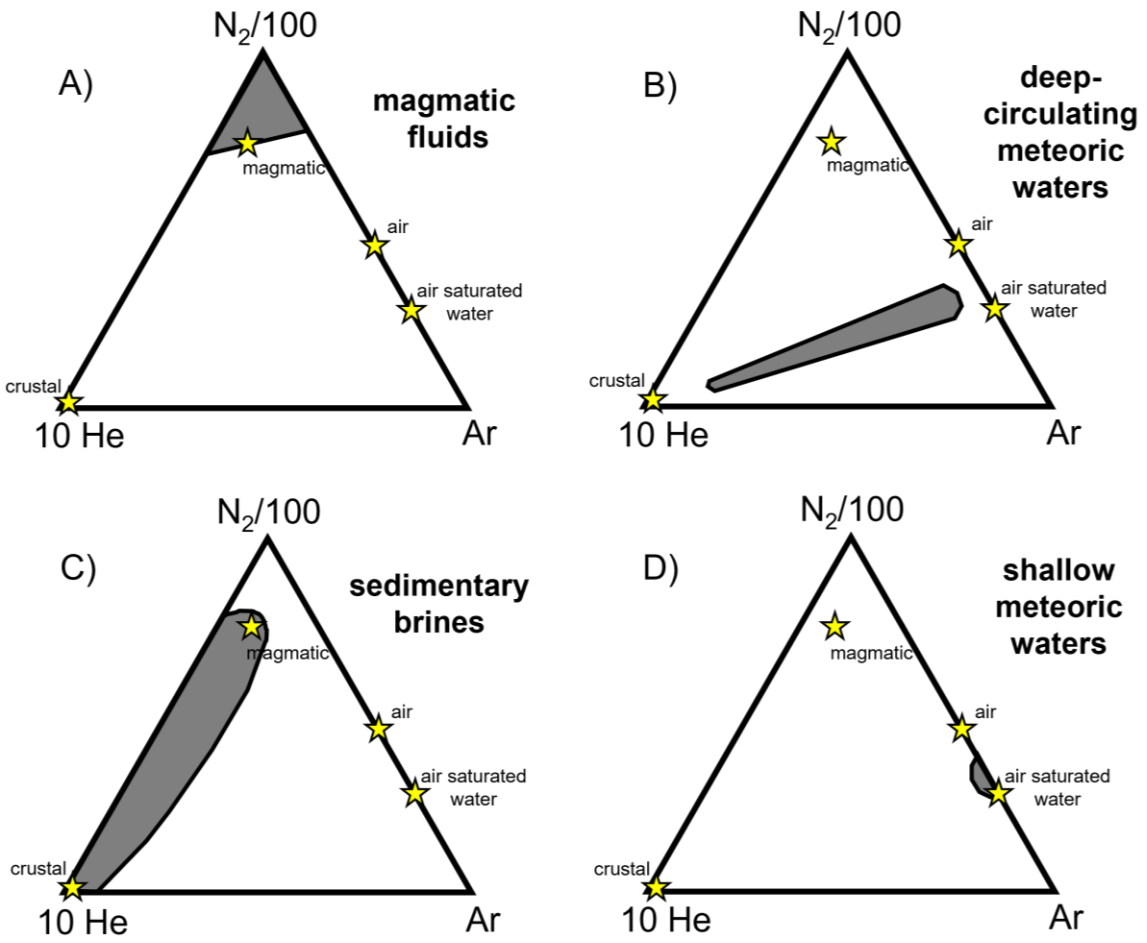


**Figure 2.12 Shaded regions in each ternary diagram represent the compositions associated with various sources: A) magmatic fluids, B) deep circulating fluids, C) sedimentary brines, D) shallow circulating meteoric fluids. Highlighted stars represent the compositions linked with the principal sources of these elements within geothermal fluids. Modified from Norman & Musgrave (1994).**

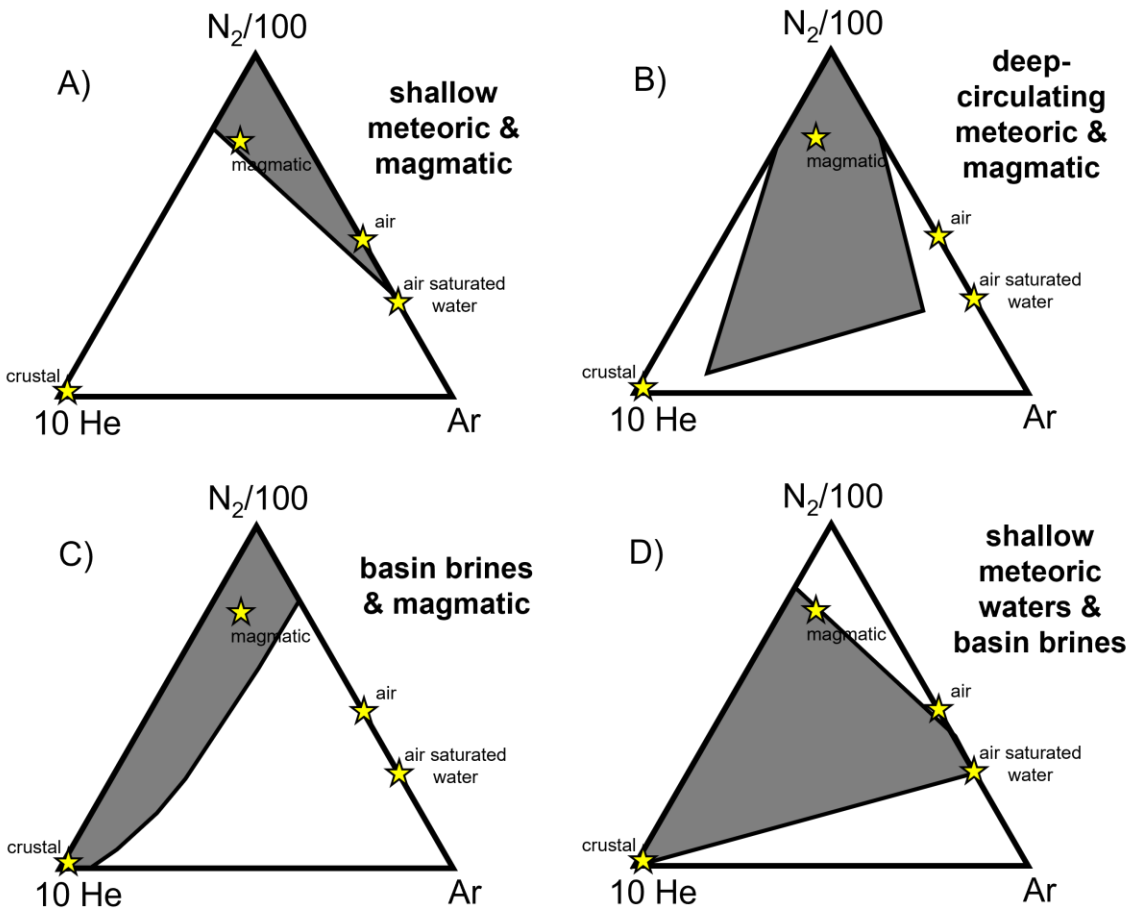


**Figure 2.13 Volatile mixture compositions originating from two distinct sources, as indicated by the shaded regions, based on the endmember compositions outlined in Figure 2.12: A) magmatic and shallow circulating meteoric fluids, B) magmatic and deep circulating meteoric fluids, C) magmatic fluids and sedimentary brines, and D) shallow circulating meteoric fluids and sedimentary brines. Highlighted stars represent the compositions linked with the principal sources of these elements within geothermal fluids. Modified from Norman & Musgrave (1994).**

### 2.5.3 Comparison with Other Impact-Generated Hydrothermal Systems

Quartz is a common hydrothermal mineral that has been documented in impact-generated hydrothermal systems all over the globe (Kirsimäe & Osinski, 2012; Naumov, 2005;

Osinski et al., 2013). There are, however, relatively few detailed studies on impact-generated hydrothermal systems and only a small handful that conducted fluid inclusion analysis. In one study, quartz-hosted fluid inclusions in vugs from the 200 km-diameter Chicxulub impact structure, Mexico, have homogenization temperatures between 200 to 285°C with salinity (wt% NaCl) levels between 14 to 20 (Lüders & Rickers, 2004). Both temperature and salinity ranges are much lower than results from Clearwater West impact structure. The 35-km-diameter Manson impact structure, U.S.A., and the 7.5-km-diameter Lockne impact structure, Sweden, have quartz-hosted fluid inclusions in hydrothermal veins within crater-fill impact melt rocks. These fluid inclusions have homogenization temperatures between 90 to 250°C and 110 to 200°C, respectively, with salinity (wt% NaCl) levels between 0.2 to 12.2 and 1.2 to 10.9, respectively (Boer et al., 1996; Sturkell et al., 1998). The smaller range in homogenization temperatures suggest that conditions were likely more consistent during quartz mineralization in these impact craters. The wide range of homogenization temperatures of quartz-hosted fluid inclusions from the Clearwater West impact-generated hydrothermal system represents variable conditions and a longer cooling time, features that are relatively uncommon.

The unusual composition of fluid inclusions at the smaller Lockne impact-generated hydrothermal system with higher salinity contents are thought to have been shaped by the release of volatiles due to melting and recrystallization of carbonate rocks (Kirsimäe et al., 2002). The same process could be the source of magmatic fluid seen in the Clearwater West impact-generated hydrothermal system. However, the Lockne impact structure formed in a marine environment at a seawater depth of more than 200 m during the Middle Ordovician, which likely resulted in the high salinity observed in the local quartz-hosted fluid inclusions (Sturkell et al., 1998). While the 36-km-diameter Clearwater West impact structure formed in a continental region, far from seawater (Schmieder et al., 2015), its structure is much larger than the 7.5-km-diameter Lockne impact structure. Therefore, it is likely that a greater amount of impact melt contributed to the associated hydrothermal system, resulting in a higher amount of magmatic fluid mixing into the system.

While various studies have previously used mass spectrometry to investigate the isotopic compositions of materials within impact craters (e.g., Debono, 2018; Simpson, 2020), our study marks the first to use quadrupole mass spectrometry (QMS) for analysing volatile contents of fluid inclusions within an impact-generated hydrothermal system. QMS has been used before for constraining fluid sources within geo- and hydrothermal systems (e.g., Blamey, 2012; Norman & Musgrave, 1994), however, has not been used to constrain fluid sources within impact-generated hydrothermal systems. Stable isotope analyses from the 32-km-diameter Rochechouart impact structure, France, and from the 200-km-diameter Sudbury impact structure, Canada, suggest the involvement of magmatic fluids in the formation of hydrothermal mineral deposits, as well as seawater (Campos-Alvarez et al., 2010; Simpson et al., 2017). Hence, while quite rare, magmatic fluids have played a role in shaping several impact-generated hydrothermal systems on Earth.

## 2.6 Conclusions

The Clearwater West impact-generated hydrothermal system has altered the local impactites. This study outlines the characteristics of hydrothermally precipitated quartz to better understand the progression of the impact-generated hydrothermal system. Authigenic quartz vugs and veins precipitated in the form of individual crystals and secondary overgrowths. Intricate grain boundaries and irregularities indicate mineral growth and recrystallization in response to hydrothermal conditions. Primary fluid inclusion microthermometry results show 3 main quartz mineralization stages: the first above 384°C, second between 382 and 246°C, and third between 243 and 120°C. Secondary fluid inclusion microthermometry results show second and third stage fluids flowing within microfractures in the outer wall and middle region of the structures, while a cooler fluid later circulated within microfractures in the central area, after complete quartz mineralization. Quartz crystallized during the early and main stages of mineralization at the Clearwater West impact-generated hydrothermal system, based on the early, main, and late stages described by Jaimes Bermudez (2023). Gas analysis results indicate that volatile sources were likely atmospheric, with a slight mix of local magmatic (from the impact melt sheet) and crustal sources (evolved fluids). Fluid

inclusion gas compositions are not homogenous and as the fluid cooled over time, it became more concentrated in NaCl.

This research reveals the characteristics of impact-generated hydrothermally precipitated quartz using methods previously unexplored at Clearwater West impact structure. These methods illustrate the ability for quartz to preserve unique characteristics, such as water temperature and salinity, making it a valuable tool for investigating past environmental conditions. This practicality extends beyond Earth to other planetary and lunar surfaces, such as impact craters on Mars, where impact-generated hydrothermally precipitated quartz has already been identified (e.g., Marzo et al., 2010; Ramkissoon et al., 2021; Smith & Bandfield, 2012). Furthermore, quartz can be used to consider the habitability of an impact-generated hydrothermal system, and assess its ability to potentially support thermo- and hyperthermophilic microbial life on Mars.

## 2.7 References

Abraini, J. H., Rostain, J. C., & Kriem, B. (1998). Sigmoidal compression rate-dependence of inert gas narcotic potency in rats: Implication for lipid vs protein theories of inert gas action in the central nervous system. *Brain Research*, *808*(2), 300–304. https://doi.org/10.1016/s0006-8993(98)00760-4

Abramov, O., & Kring, D. A. (2004). Numerical modeling of an impact-induced hydrothermal system at the Sudbury crater. *Journal of Geophysical Research*, *109*, E10007. https://doi.org/10.1029/2003je002213

Abramov, O., & Kring, D. A. (2007). Numerical modeling of impact-induced hydrothermal activity at the Chicxulub crater. *Meteoritics and Planetary Science*, *42*, 93–112. https://doi.org/10.1111/j.1945-5100.2007.tb00220.x

Abramov, O., & Mojzsis, S. J. (2009). Microbial habitability of the Hadean Earth during the late heavy bombardment. *Nature*, *459*, 419–422. https://doi.org/10.1038/nature08015

Allen, C. C., Gooding, J. L., & Keil, K. (1982). Hydrothermally altered impact melt rock and breccia: Contributions to the soil of Mars. *Journal of Geophysical Research: Solid Earth*, *87*(B12), 10083–10101. https://doi.org/10.1029/jb087ib12p10083

Beals, C. S., Ferguson, G. M., & Landau, A. (1956). Canadian scientists report (II. A search for analogies between lunar and terrestrial topography on photographs of the Canadian Shield, Part I). *Journal of the Royal Astronomical Society of Canada*, *50*, 203–261.

Blamey, N. J. F. (2012). Composition and evolution of crustal, geothermal and hydrothermal fluids interpreted using quantitative fluid inclusion gas analysis. *Journal of Geochemical Exploration*, *116–117*, 17–27. https://doi.org/10.1016/j.gexpl.2012.03.001

Blamey, N. J. F., Boston, P. J., & Rosales-Lagarde, L. (2016). High-resolution signatures of oxygenation and microbiological activity in speleothem fluid inclusions. *International Journal of Speleology*, *45*(3), 231–241. https://doi.org/10.5038/1827-806x.45.3.1950

Blamey, N. J. F., & Norman, D. I. (2002). New interpretations of geothermal fluid inclusion volatiles: Ar/He and $N_2$/Ar ratios - A better indicator of magmatic volatiles, and equilibrium gas geothermometry. *27th Workshop on Geothermal Reservoir Engineering*.

Blamey, N. J. F., Parnell, J., & Longerich, H. P. (2012). Understanding detection limits in fluid inclusion analysis using an incremental crush fast scan method for planetary science. *43rd Lunar and Planetary Science Conference*, Contribution No. 1035.

Blamey, N. J. F., Parnell, J., McMahon, S., Mark, D. F., Tomkinson, T., Lee, M. R., Shivak, J., Izawa, M. R. M., Banerjee, N. R., & Flemming, R. L. (2015). Evidence for methane in Martian meteorites. *Nature Communications*, *6*(1), 7399. https://doi.org/10.1038/ncomms8399

Bodnar, R. J. (1993). Revised equation and table for determining the freezing point depression of $H_2O$-NaCl solutions. *Geochimica et Cosmochimica Acta*, *57*(3), 683–684. https://doi.org/10.1016/0016-7037(93)90378-a

Boer, R. H., Reimold, W. U., Koeberl, C., & Kesler, S. E. (1996). Fluid inclusion studies on drill core samples from the Manson impact crater: Evidence for post-impact hydrothermal activity. In C. Koeberl & R. R. Anderson (Eds.), *The Manson Impact Structure, Iowa: Anatomy of an Impact Crater* (302nd ed., pp. 377–382). Geological Society of America Special Paper. https://doi.org/10.1130/0-8137-2302-7.377

Bostock, H. H. (1969). The Clearwater Complex, New Quebec. *Geological Survey of Canada*, *178*, 63 pages.

Bunch, T. E. (1968). Some characteristics of selected minerals from craters. In B. M. French & N. M. Short (Eds.), *Shock Metamorphism of Natural Materials* (pp. 413–432). Mono Book Corporation.

Campos-Alvarez, N. O., Samson, I. M., Fryer, B. J., & Ames, D. E. (2010). Fluid sources and hydrothermal architecture of the Sudbury Structure: Constraints from femtosecond LA-MC-ICP-MS Sr isotopic analysis of hydrothermal epidote and calcite. *Chemical Geology*, *278*(3–4), 131–150. https://doi.org/10.1016/j.chemgeo.2010.09.006

Cockell, C. S. (2006). The origin and emergence of life under impact bombardment. *Philosophical Transactions of the Royal Society of London. Series B, Biological Sciences*, *361*(1474), 1845–1856. https://doi.org/10.1098/rstb.2006.1908

Cockell, C. S., & Lee, P. (2002). The biology of impact craters - A review. *Biological Reviews of the Cambridge Philosophical Society*, *77*(3), 279–310. https://doi.org/10.1017/s146479310100584x

Cockell, C. S., Lee, P., Broady, P., Lim, D. S. S., Osinski, G. R., Parnell, J., Koeberl, C., Pesonen, L., & Salminen, J. (2005). Effects of asteroid and comet impacts on habitats for lithophytic organisms—A synthesis. *Meteoritics and Planetary Science*, *40*(12), 1901–1914. https://doi.org/10.1111/j.1945-5100.2005.tb00153.x

Debono, L. E. (2018). *A targeted investigation of the upper contact unit of the Sudbury Igneous Complex in the North Range, Sudbury impact structure, Canada*. The University of Western Ontario.

Dence, M. R. (1964). A comparative structural and petrographic study of probable Canadian meteorite craters. *Metoritics*, *2*(3), 249. https://doi.org/10.1111/j.1945-5100.1964.tb01432.x

Dence, M. R., Innes, M. J. S., & Beals, C. S. (1965). On the probable meteorite origin of the Clearwater Lakes, Quebec. *Journal of the Royal Astronomical Society of Canada*, *59*, 13–22.

Dirri, F., Longobardo, A., Palomba, E., Berthoud, L., Hutzler, A., Smith, C. L., & Russell, S. S. (2021). Recovery and transport of samples. In A. Longobardo (Ed.), *Sample Return Missions: The Last Frontier of Solar System Exploration* (pp. 297–314). Elsevier. https://doi.org/10.1016/b978-0-12-818330-4.00015-x

Fournier, R. O. (1985). The behaviour of silica in hydrothermal solutions. In B. R. Berger & P. M. Bethke (Eds.), *Geology and Geochemistry of Epithermal Systems* (2nd ed., pp. 45–60). Society of Economic Geologists.

French, B. M. (1998). Traces of catastrophe: A handbook of shock-metamorphic effects in terrestrial meteorite impact structures. *29th Lunar and Planetary Science Conference*, Contribution No. 954.

Giggenbach, W. F. (1986). The use of gas chemistry in delineating the origin of fluid discharges over the Taupo Volcanic Zone: A review. *5th International Volcanological Congress*, 47–50.

Grieve, R. A. F. (2006). Impact structures of Canada. *GEOtext 5, Geological Association of Canada*.

Hische, R. (1995). *Geologie der Clearwater-Impaktstruktur / Quebec [Geology of the Clearwater impact structure / Quebec]*. Westfälische Wilhelms-Universität Münster.

Isenhour, T. L., & Jurs, P. C. (1979). *Introduction to computer programming for chemists*. Allyn & Baco.

Jaimes Bermudez, J. (2023). *Investigation of the impact-generated hydrothermal system at the West Clearwater Lake impact structure, Quebec, Canada*. University of Western Ontario.

Jones, H. D., & Kesler, S. E. (1992). Fluid inclusion gas chemistry in east Tennessee Mississippi Valley-type districts: Evidence for immiscibility and implications for depositional mechanisms. *Geochimica et Cosmochimica Acta*, *56*, 137–154.

Kerrigan, M. C., & Osinski, G. R. (2015). Overview of impact-generated hydrothermal activity at the West Clearwater Lake impact structure, Canada. *46th Lunar and Planetary Science Conference*.

Kirsimäe, K., & Osinski, G. R. (2012). Impact-induced hydrothermal activity. In G. R. Osinski & E. Pierazzo (Eds.), *Impact Cratering: Processes and Products* (pp. 76–89). Wiley-Blackwell. https://doi.org/10.1002/9781118447307.ch6

Kirsimäe, K., Suuroja, S., Kirs, J., Kärki, A., Polikarpus, M., Puura, V., & Suuroja, K. (2002). Hornblende alteration and fluid inclusions in Kärdla impact crater, Estonia: An indication for the post-impact hydrothermal activities. *Meteoritics and Planetary Science*, *37*(3), 449–457. https://doi.org/10.1111/j.1945-5100.2002.tb00827.x

Krank, S. H., & Sinclair, G. W. (1963). Clearwater Lake, New Quebec. *Geological Survey of Canada, B. 100*, 25 pages.

Lüders, V., & Rickers, K. (2004). Fluid inclusion evidence for impact-related hydrothermal fluid and hydrocarbon migration in Creataceous sediments of the ICDP-Chicxulub drill core Yaxcopoil-1. *Meteoritics and Planetary Science*, *39*, 1187–1197. https://doi.org/10.1111/j.1945-5100.2004.tb01136.x

Marzo, G. A., Davila, A. F., Tornabene, L. L., Dohm, J. M., Fairén, A. G., Gross, C., Kneissl, T., Bishop, J. L., Roush, T. L., & McKay, C. P. (2010). Evidence for Hesperian impact-induced hydrothermalism on Mars. *Icarus*, *208*(2), 667–683. https://doi.org/10.1016/j.icarus.2010.03.013

McIntyre, D. B. (1968). Impact metamorphism at Clearwater Lake, Quebec. In B. M. French & N. M. Short (Eds.), *Shock Metamorphism of Natural Materials* (pp. 363–366). Mono Book Corporation.

Merino, N., Aronson, H. S., Bojanova, D. P., Feyhl-Buska, J., Wong, M. L., Zhang, S., & Giovannelli, D. (2019). Living at the extremes: Extremophiles and the limits of life in a planetary context. *Frontiers in Microbiology*, *10*, Article 780. https://doi.org/10.3389/fmicb.2019.00780

Meyer, M. A., Kminek, G., Beaty, D. W., Carrier, B. L., Haltigin, T., Hays, L. E., Agree, C. B., Busemann, H., Cavalazzi, B., Cockell, C. S., Debaille, V., Glavin, D. P., Grady, M. M., Hauber, E., Hutzler, A., Marty, B., McCubbin, F. M., Pratt, L. M., Regberg, A. B., … Zorzano, M. P. (2022). Final report of the Mars sample return science planning group 2 (MSPG2). *Astrobiology*, *22*(S1), S5–S26. https://doi.org/10.1089/ast.2021.0121

Naumov, M. V. (2002). Impact-generated hydrothermal systems: Data from Popigai, Kara, and Puchezh-Katunki impact structures. In *Impacts in Precambrian Shields* (pp. 117–171). Springer, Berlin, Heidelberg.

Naumov, M. V. (2005). Principal features of impact-generated hydrothermal circulation systems: Mineralogical and geochemical evidence. *Geofluids*, *5*, 165–184. https://doi.org/10.1111/j.1468-8123.2005.00092.x

Norman, D. I., & Blamey, N. J. F. (2001). Quantitative analysis of fluid inclusion volatiles by a two quadrupole mass spectrometer system. *16th ECROFI: European Current Research on Fluid Inclusions*.

Norman, D. I., Blamey, N. J. F., & Moore, J. N. (2002). Interpreting geothermal processes and fluid sources from fluid inclusion organic compounds and $CO_2/N_2$ ratios. *27th Workshop on Geothermal Reservoir Engineering*.

Norman, D. I., & Moore, J. N. (1997). Gaseous species in fluid inclusions: A fluid tracer and indicator of fluid processes. *14th ECROFI: European Current Research on Fluid Inclusions*.

Norman, D. I., & Moore, J. N. (1999). Methane and excess $N_2$ and Ar in geothermal fluid inclusions. *24th Workshop of Geothermal Reservoir Engineering*, 233–240.

Norman, D. I., & Musgrave, J. A. (1994). $N_2$-Ar-He compositions in fluid inclusions: Indicators of fluid source. *Geochimica et Cosmochimica Acta*, *58*(3), 1119–1131. https://doi.org/10.1016/0016-7037(94)90576-2

Norman, D. I., & Sawkins, F. J. (1987). Analysis of volatiles in fluid inclusions by mass spectrometry. *Chemical Geology*, *61*(1–4), 1–10. https://doi.org/10.1016/0009-2541(87)90020-9

Norman, D. I., Ting, W., Putnam III, B. R., & Smith, R. W. (1985). Mineralization of the Hansonburg Mississippi-Valley-type deposit, New Mexico: Insight from composition of gases in fluid inclusions. *Canadian Mineralogist*, *23*, 353–368.

Norton, D. L. (1984). Theory of hydrothermal systems. *Annual Review of Earth and Planetary Sciences*, *12*, 155–177.

Osinski, G. R., Brunner, A., Collins, G. S., Cohen, B. A., Coulter, A., Elphic, R., Grieve, R. A. F., Hodges, K., Horne, A., Kerrigan, M. C., Lim, D. S. S., Misener, R., Morgan, J. V., Rae, A. S. P., Saint-Jacques, D., Skok, J. R., Squyres, S., Tornabene, L. L., Wilks, R., & Young, K. (2015). Revisiting the West Clearwater Lake structure, Canada. *46th Lunar and Planetary Science Conference*.

Osinski, G. R., Cockell, C. S., Pontefract, A., & Sapers, H. M. (2020). The role of meteorite impacts in the origin of life. *Astrobiology*, *20*(9), 1121–1149. https://doi.org/10.1089/ast.2019.2203

Osinski, G. R., Grieve, R. A. F., Ferrière, L., Losiak, A., Pickersgill, A. E., Cavosie, A. J., Hibbard, S. M., Hill, P. J. A., Jaimes Bermudez, J., Marion, C. L., Newman, J. D., & Simpson, S. L. (2022). Impact Earth: A review of the terrestrial impact record. *Earth-Science Reviews*, *232*, E01008. https://doi.org/10.1016/j.earscirev.2022.104112

Osinski, G. R., Tornabene, L. L., Banerjee, N. R., Cockell, C. S., Flemming, R. L., Izawa, M. R. M., McCutcheon, J., Parnell, J., Preston, L. J., Pickersgill, A. E., Pontefract, A., Sapers, H. M., & Southam, G. (2013). Impact-generated hydrothermal systems on Earth and Mars. *Icarus*, *224*(2), 347–363. https://doi.org/10.1016/j.icarus.2012.08.030

Osinski, G. R., Tornabene, L. L., Banerjee, N. R., Cockell, C. S., Flemming, R. L., Izawa, M. R. M., McCutcheon, J., Pontefract, A., Parnell, J., Sapers, H. M., & Southam, G. (2012). Impact craters as habitats for life on early Mars. *3rd Conference on Early Mars*, Contribution No. 7068. https://doi.org/10.1016/j.gca.2006.06.175

Parnell, J., Lee, P., Cockell, C. S., & Osinski, G. R. (2004). Microbial colonization in impact-generated hydrothermal sulphate deposits, Haughton impact structure, and implications for sulphates on Mars. *International Journal of Astrobiology*, *3*, 247–256. https://doi.org/10.1017/s1473550404001995

Parnell, J., Taylor, C. W., Thackrey, S., Osinski, G. R., & Lee, P. (2010). Permeability data for impact breccias imply focussed hydrothermal fluid flow. *Journal of Geochemical Exploration*, *106*(1–3), 171–175. https://doi.org/10.1016/j.gexplo.2009.12.002

Parry, W. T., & Blamey, N. J. F. (2010). Fault fluid composition from fluid inclusion measurements, Laramide age Uinta thrust fault, Utah. *Chemical Geology*, *278*(1–2), 105–119. https://doi.org/10.1016/j.chemgeo.2010.09.005

Phinney, W. C., Simonds, C. H., Cochran, A., McGee, P. E., Simonds, C. H., Cochran, A., & McGee, P. E. (1978). West Clearwater, Quebec impact structure, Part II: Petrology. *9th Lunar and Planetary Science Conference*, *2*, 2659–2694.

Pierazzo, E., & Melosh, H. J. (2012). Environmental effects of impact events. In G. R. Osinski & E. Pierazzo (Eds.), *Impact Cratering: Processes and Products* (pp. 146–154). Wiley-Blackwell. https://doi.org/10.1002/9781118447307.ch10

Pontefract, A., Osinski, G. R., Cockell, C. S., Moore, C. A., Moores, J. E., & Southam, G. (2014). Impact-generated endolithic habitat within crystalline rocks of the Haughton impact structure, Devon Island, Canada. *Astrobiology*, *14*(6), 522–533. https://doi.org/10.1089/ast.2013.1100

Ramkissoon, N. K., Turner, S. M. R., Macey, M. C., Schwenzer, S. P., Reed, M. H., Pearson, V. K., & Olsson-Francis, K. (2021). Exploring the environments of Martian impact-generated hydrothermal systems and their potential to support life. *Meteoritics and Planetary Science*, *56*(7), 1350–1368.

Robertson, P. B., Dence, M. R., & Vos, M. A. (1968). Deformation in rock-forming minerals from Canadian craters. *Contributions from the Dominion Astrophysical Observatory in Victoria*, *8*(23), 20.

Rosa, D. F. (2011). *The sheet of impact melt at West Clearwater Lake, Northern Quebec*. McGill University.

Sapers, H. M., Banerjee, N. R., & Osinski, G. R. (2015). Potential for impact glass to preserve microbial metabolism. *Earth and Planetary Science Letters*, *430*, 95–104. https://doi.org/10.1016/j.epsl.2015.08.011

Schmieder, M., Schwarz, W. H., Trieloff, M., Tohver, E., Buchner, E., Hopp, J., & Osinski, G. R. (2015). New 40Ar/39Ar dating of the Clearwater Lake impact structures (Québec, Canada) – Not the binary asteroid impact it seems? *Geochimica et Cosmochimica Acta*, *148*, 304–324. https://doi.org/10.1016/j.gca.2014.09.037

Simard, M., Labbé, J. Y., Lacoste, P., Leclerc, A., & Boily, M. (2008). Synthèse du nord-est de la province du Supérieur [Synthesis of the northeast of the Superior Province]. *Ministère Des Ressources Naturelles, Québec*, 199 pages.

Simard, M., Parent, M., Thériault, R., David, J., Lacoste, P., & Sharma, K. N. M. (2004). Géologie de la région du lac à l'Eau Claire (34B et 34C) [Geology of the Clearwater Lake area (34B and 34C)]. *Ministère Des Ressources Naturelles, Québec*, 48 pages.

Simonds, C. H., Phinney, W. C., McGee, P. E., & Cochran, A. (1978). West Clearwater, Quebec impact structure, Part I : Field geology, structure and bulk chemistry. *9th Lunar and Planetary Science Conference*, 2633–2658.

Simpson, S. L. (2020). *Clay mineral characterization and production in impact settings: A case study on the Chicxulub impact strcutre, Mexico*. University of Western Ontario.

Simpson, S. L., Boyce, A. J., Lambert, P., Lindgren, P., & Lee, M. R. (2017). Evidence for an impact-induced biosphere from the δ34S signature of sulphides in the Rochechouart impact structure, France. *Earth and Planetary Science Letters*, *460*, 192–200. https://doi.org/10.1016/j.epsl.2016.12.023

Sleep, N. H. (2018). Geological and geochemical constraints on the origin and evolution of life. *Astrobiology*, *18*(9), 1199–1219. https://doi.org/10.1089/ast.2017.1778

Smith, M. R., & Bandfield, J. L. (2012). Geology of quartz and hydrated silica-bearing deposits near Antoniadi Crater, Mars. *Journal of Geophysical Research: Planets*, *117*, E06007. https://doi.org/10.1029/2011je004038

Stetter, K. O. (2007). Hyperthermophiles in the history of life. In G. R. Bock & J. A. Goode (Eds.), *Ciba Foundation Symposium 202 - Evolution of Hydrothermal Ecosystems on Earth (and Mars?)* (pp. 1–23). John Wiley & Sons, Ltd. https://doi.org/10.1002/9780470514986.ch1

Stöffler, D. (1977). Research drilling Nördlingen 1973: Polymict breccias, crater basement, and cratering model of the Ries impact structure. *Geologica Bavarica*, *75*, 443–458.

Sturkell, E. F. F., Broman, G., Forsberg, P., & Torrsander, P. (1998). Impact-related hydrothermal activity in the Lockne impact structure, Jämtland, Sweden. *European Journal of Mineralogy*, *10*(3), 589–606. https://doi.org/10.1127/ejm/10/3/0589

Sun, Z., Wang, J., Wang, Y., Zhang, Y., & Zhao, L. (2021). Multistage hydrothermal quartz veins record the ore-forming fluid evolution in the Meiling Cu–Zn (Au) deposit, NW China. *Ore Geology Reviews*, *131*, 104002. https://doi.org/10.1016/j.oregeorev.2021.104002

Tolometti, G., Osinski, G. R., & Neish, C. D. (2018). The impact melt sheet at West Clearwater impact structure: A petrographic and geochemical analysis. *49th Lunar and Planetary Science Conference*, Contribution No. 2083.

Versh, E., Kirsimäe, K., & Jõeleht, A. (2006). Development of potential ecological niches in impact-induced hydrothermal systems: The small-to-medium size impacts. *Planetary and Space Science*, *54*(15), 1567–1574. https://doi.org/10.1016/i.pss.2005.12.022

Wang, Q., Cen, Z., & Zhao, J. (2015). The survival mechanisms of thermophiles at high temperatures: An angle of omics. *Physiology*, *30*(2), 97–106. https://doi.org/10.1152/physiol.00066.2013

Wilks, R. (2016). *Geochemical and petrographic study of melt veins at the West Clearwater Lake impact structure, Canada*. University of Western Ontario.

# 3 Summary and Conclusion

## 3.1 Summary

The objective of this thesis was to further constrain the thermal and fluid evolution of the impact-generated hydrothermal system at the Clearwater West Lake impact structure. Samples of hydrothermally precipitated quartz vugs hosted in crater-fill impactites were analyzed using optical microscopy, electron microprobe analysis (EMPA), mass spectrometry, and fluid inclusion microthermometry. Mass spectrometry and fluid inclusion microthermometry are methods previously unexplored within the context of the Clearwater West impact structure. EMPA data showed euhedral quartz crystals with evidence of pauses and breaks, the result of ununiform quartz crystal growth in solutions with gradually evolving conditions. There were likely periods of steady and slow crystal growth and episodes where growth was interrupted, suggesting fluctuations in hydrothermal conditions within the impact site. Three main quartz mineralization stages were interpreted from primary fluid inclusion microthermometry data: the first above 384°C, second between 382 and 246°C, and third between 243 and 120°C. Fluid sources were identified through quadrupole mass spectrometry (QMS) data to be mostly meteoric, with minor mixing of local magmatic (from the impact melt sheet) and crustal sources. Fluid inclusion gas compositions are not homogenous and as the fluid cooled over time, it became more concentrated in NaCl.

## 3.2 Implications for the Study of Rocky Bodies

The Clearwater West impact structure can be thought of as an analogue for other impact-generated hydrothermal systems in our solar system. Earth's impact cratering record suggests that hydrothermal activity is a common geologic formation following large impacts into planetary surfaces abundant in $H_2O$ (e.g., ice deposits or flowing groundwater) (Cockell et al., 2003; Osinski et al., 2013, 2020). Impacts could expand the potential for any planetary body with the necessary ingredients for life (including those delivered by the projectile) to be habitable, even if only temporarily (Osinski et al., 2020). Impacts provide a significant heat source in cold extraterrestrial environments, such as Mars, Europa, or Titan. Therefore, it is not unreasonable to assume that these

environments could produce life-favouring conditions on other planetary bodies. This thesis highlights the potential of transient impact-generated hydrothermal systems in hosting endolithic organisms after sufficient cooling.

Mars has been suggested as the most likely site for preserved evidence of impact-generated hydrothermal systems as impact craters may have had interactions with liquid water that once flowed on its surface (Abramov & Kring, 2005; Cannon et al., 2017). Past and current Mars exploration missions have identified morphological, chemical, and mineralogical evidence supporting the existence of stable liquid water present on the surface during the earliest period of Martian geological history, the Noachian period, from 4.1 to 3.7 Ga (Carr & Head III, 2010; Ehlmann et al., 2013; Marzo et al., 2010). Studies suggest that large impact craters on Mars (over 65 km in diameter) could have supported ice-covered lakes for thousands of years (Newsom et al., 1996). In addition, a significant volume of subsurface ground ice in northern latitudes was discovered, implying that there is a likely occurrence of impact-generated hydrothermal activity following impact events on present-day Mars (Marzo et al., 2010).

The search for life on Mars has been ongoing for decades, yet the exploration of extant and extinct lifeforms remains a priority for rover missions as we continue our search for definitive proof. Hydrothermal alteration was thought to be possible on Mars from observations taken by the early Viking landers (Newsom & Hagerty, 1997). The Mars Science Laboratory (MSL) *Curiosity* rover mission later found evidence of impact-generated hydrothermal systems on the Martian surface, including clay (Bristow et al., 2018; Cannon et al., 2017; Jébrak, 2015). Most of these clay detections were found in the strongly bombarded Martian southern highlands and inside other impact craters on the Martian surface (Osinski et al., 2020). Impact craters can provide episodic habitable surface conditions, protective endolithic environments (from UV and cosmic radiation), and access to subsurface environments—the biggest and longest-lived habitable environments on Mars (Osinski et al., 2020). Therefore, if life once existed on Mars, the ideal place to quest for potential biosignatures would be lithic habitats (e.g., the interior of shocked lithologies or substrates generated in impact hydrothermal systems).

Impact-generated hydrothermal deposits may provide some of the most favourable and abundant opportunities for preserving evidence for life on Mars (Osinski, Tornabene, et al., 2012; Osinski et al., 2020). Precipitated minerals from hydrothermal fluids offer energy for cellular metabolism, and have been shown to preserve microbial fossils and organic biomarkers on Earth (Parnell et al., 2004, 2010). This thesis showed that the exceptional capacity of quartz to encapsulate the characteristics of ancient fluids adds significant value to its potential as a tool for deciphering paleoenvironments of water-bearing rocky environments, such as Mars. This is particularly relevant due to the discovery of quartz in Martian impact craters (e.g., Marzo et al., 2010; Ramkissoon et al., 2021; Smith & Bandfield, 2012). In addition, this research extends to the consideration of the role of quartz in assessing the viability of impact-generated hydrothermal systems as plausible habitats for sustaining thermos- and hyperthermophilic microbial life on Mars. A large volume of precipitated minerals can be found in fracture networks within impact structures (Parnell et al., 2010), so these environments should be targets for future exploration of life on Mars. Hence, Martian impact craters with evidence of hydrothermal alteration are strong candidates for future landing sites as they are high-quality environments that may preserve extinct, and possibly even extant, extraterrestrial life.

## 3.3 Future Work

Several intriguing avenues for future exploration emerge from the findings of this thesis. Expanding the analysis to encompass a wider range of impact-generated hydrothermal systems could provide a broader understanding of their formation and evolution, as well as their mineralogical complexities. Additionally, conducting comparative studies with other planetary bodies, particularly Mars, could provide further understanding of the potential habitability of impact-generated hydrothermal systems beyond Earth. Investigating the impact of various variables, such as impact energy and target composition, on the mineralogical outcomes of these hydrothermal systems could lead to insights into the underlying mechanisms. Future work on the Clearwater West impact-generated hydrothermal system that could help further constrain its formation and evolution include: 1) using other analytical tools, such as Raman spectroscopy and stable isotope analysis, on quartz-hosted fluid inclusions from quartz vugs and amygdules to

confirm temperature range and salinity results shown in this thesis; 2) LA-ICP-MS of quartz to quantify titanium content and apply the Ti-in-quartz geothermometer; and 3) U-Pb or (U-Th)-Ne dating of hematite to establish a timeframe for the activity and duration of the hydrothermal system. The duration of the system plays a crucial role in the potential for and extent of microbial colonization. Furthermore, further work should be performed to confirm the impact-generated hydrothermal fluid sources, as this is a new territory that has not yet been investigated and needs to be further constrained. A study investigating volatiles within impact melt sheets should also be prioritized, to aid in constraining the movement of volatiles during the formation of impact-generated hydrothermal systems. Overall, these future endeavours have the potential to deepen our understanding of the impact-generated hydrothermal processes and their implications for the broader fields of astrobiology and planetary geology.

## 3.4 References

Abramov, O., & Kring, D. A. (2005). Impact-induced hydrothermal activity on early Mars. *Journal of Geophysical Research, 110*, E12S09. https://doi.org/10.1029/2005je002453

Bristow, T. F., Rampe, E. B., Achilles, C. N., Blake, D. F., Chipera, S. J., Craig, P., Crisp, J. A., Des Marais, D. J., Downs, R. T., Gellert, R., Grotzinger, J. P., Gupta, S., Hazen, R. M., Horgan, B., Hogancamp, J. V., Mangold, N., Mahaffy, P. R., McAdam, A. C., Ming, D. W., … Yen, A. S. (2018). Clay mineral diversity and abundance in sedimentary rocks of Gale crater, Mars. *Science Advances*, *4*(6), eaar3330. https://doi.org/10.1126/sciadv.aar3330

Cannon, K. M., Parman, S. W., & Mustard, J. F. (2017). Primordial clays on Mars formed beneath a steam or supercritical atmosphere. *Nature*, *552*(7683), 88–91. https://doi.org/10.1038/nature24657

Carr, M. H., & Head III, J. W. (2010). Geologic history of Mars. *Earth and Planetary Science Letters*, *294*(3–4), 185–203. https://doi.org/10.1016/j.epsl.2009.06.042

Cockell, C. S., Osinski, G. R., & Lee, P. (2003). The impact crater as a habitat: Effects of impact processing of target materials. *Astrobiology*, *3*(1), 181–191. https://doi.org/10.1089/153110703321632507

Ehlmann, B. L., Berger, G., Mangold, N., Michalski, J. R., Catling, D. C., Ruff, S. W., Chassefière, E., Niles, P. B., Chevrier, V., & Poulet, F. (2013). Geochemical consequences of widespread clay mineral formation in Mars' ancient crust. *Space Science Reviews*, *174*(1–4), 329–364. https://doi.org/10.1007/s11214-012-9930-0

Jébrak, M. (2015). Hydrothermal Alteration. In M. Gargaud, W. M. Irvine, R. Amils, H. J. Cleaves, D. L. Pinti, J. C. Quintanilla, D. Rouan, T. Spohn, S. Tirard, & M. Viso (Eds.), *Encyclopedia of Astrobiology* (pp. 1156–1157). Springer, Berlin, Heidelberg. https://doi.org/10.1007/978-3-662-44185-5_5150

Marzo, G. A., Davila, A. F., Tornabene, L. L., Dohm, J. M., Fairén, A. G., Gross, C., Kneissl, T., Bishop, J. L., Roush, T. L., & McKay, C. P. (2010). Evidence for Hesperian impact-induced hydrothermalism on Mars. *Icarus*, *208*(2), 667–683. https://doi.org/10.1016/j.icarus.2010.03.013

Newsom, H. E., Brittelle, G. E., Hibbitts, C. A., Crossey, L. J., & Kudo, A. M. (1996). Impact crater lakes on Mars. *Journal of Geophysical Research: Atmospheres*, *101*(E6), 14951–14955. https://doi.org/10.1029/96je01139

Newsom, H. E., & Hagerty, J. J. (1997). Chemical components of the Martian soil: Melt degassing, hydrothermal alteration, and chondritic debris. *Journal of Geophysical Research: Planets*, *102*(E8), 19345–19355. https://doi.org/10.1029/97je01687

Osinski, G. R., Cockell, C. S., Pontefract, A., & Sapers, H. M. (2020). The role of meteorite impacts in the origin of life. *Astrobiology*, *20*(9), 1121–1149. https://doi.org/10.1089/ast.2019.2203

Osinski, G. R., Tornabene, L. L., Banerjee, N. R., Cockell, C. S., Flemming, R. L., Izawa, M. R. M., McCutcheon, J., Parnell, J., Preston, L. J., Pickersgill, A. E., Pontefract, A., Sapers, H. M., & Southam, G. (2013). Impact-generated hydrothermal systems on Earth and Mars. *Icarus*, *224*(2), 347–363. https://doi.org/10.1016/j.icarus.2012.08.030

Osinski, G. R., Tornabene, L. L., Banerjee, N. R., Cockell, C. S., Flemming, R. L., Izawa, M. R. M., McCutcheon, J., Pontefract, A., Parnell, J., Sapers, H. M., & Southam, G. (2012). Impact craters as habitats for life on early Mars. *3rd Conference on Early Mars*, Contribution No. 7068. https://doi.org/10.1016/j.gca.2006.06.175

Parnell, J., Lee, P., Cockell, C. S., & Osinski, G. R. (2004). Microbial colonization in impact-generated hydrothermal sulphate deposits, Haughton impact structure, and implications for sulphates on Mars. *International Journal of Astrobiology*, *3*, 247–256. https://doi.org/10.1017/s1473550404001995

Parnell, J., Taylor, C. W., Thackrey, S., Osinski, G. R., & Lee, P. (2010). Permeability data for impact breccias imply focussed hydrothermal fluid flow. *Journal of Geochemical Exploration*, *106*(1–3), 171–175. https://doi.org/10.1016/j.gexplo.2009.12.002

Ramkissoon, N. K., Turner, S. M. R., Macey, M. C., Schwenzer, S. P., Reed, M. H., Pearson, V. K., & Olsson-Francis, K. (2021). Exploring the environments of Martian impact-generated hydrothermal systems and their potential to support life. *Meteoritics and Planetary Science*, *56*(7), 1350–1368.

Smith, M. R., & Bandfield, J. L. (2012). Geology of quartz and hydrated silica-bearing deposits near Antoniadi Crater, Mars. *Journal of Geophysical Research: Planets*, *117*, E06007. https://doi.org/10.1029/2011je004038

# Appendices

## Appendix A. WDS spot analyses (wt% & ppm) on 5 quartz vug samples.

| Sample # | Point | CL intensity colour | $SiO_2$ (Mass %) | $Na_2O$ (Mass %) | $TiO_2$ (Mass %) | Total (Mass %) | Na ppm | Ti ppm |
|---|---|---|---|---|---|---|---|---|
| MK-029 | 1 | Dark blue | 96.698 | 0.044 | 0.014 | 96.756 | 326 | 84 |
| | 2 | | 96.916 | 0.05 | 0.012 | 96.978 | 371 | 72 |
| | 3 | | 97.555 | 0.052 | 0.02 | 97.627 | 386 | 120 |
| | 4 | Green (inside edge) | 98.853 | 0.005 | 0.013 | 98.871 | 37 | 78 |
| | 5 | | 98.797 | 0.001 | 0.009 | 98.807 | 7 | 54 |
| | 6 | | 98.872 | 0.007 | 0.019 | 98.898 | 52 | 114 |
| | 7 | Medium blue | 98.453 | nd | 0.017 | 98.47 | nd | 102 |
| | 8 | | 99.057 | nd | 0.015 | 99.072 | nd | 90 |
| | 9 | | 98.411 | nd | 0.013 | 98.424 | nd | 78 |
| MK-036 | 1 | Dark blue (beside crack) | 98.905 | 0.003 | 0.01 | 98.918 | 22 | 60 |
| | 2 | | 98.764 | 0.000 | 0.015 | 98.779 | 0 | 90 |
| | 3 | | 98.467 | 0.01 | 0.009 | 98.486 | 74 | 54 |
| | 4 | Light blue | 98.329 | nd | 0.013 | 98.342 | nd | 78 |
| | 5 | | 98.878 | 0.003 | 0.013 | 98.894 | 22 | 78 |
| | 6 | | 98.712 | 0.001 | 0.012 | 98.725 | 7 | 72 |
| | 7 | Green | 99.061 | 0.004 | 0.016 | 99.081 | 30 | 96 |
| | 8 | | 98.905 | 0.002 | 0.011 | 98.918 | 15 | 66 |
| | 9 | | 98.411 | 0.005 | 0.016 | 98.432 | 37 | 96 |
| MK-070 | 1 | Dark blue | 98.248 | 0.011 | 0.017 | 98.276 | 82 | 102 |
| | 2 | | 98.011 | 0.029 | 0.011 | 98.051 | 215 | 66 |
| | 3 | | 97.703 | 0.045 | 0.015 | 97.764 | 334 | 90 |
| | 4 | Light blue | 98.270 | 0.007 | 0.010 | 98.287 | 52 | 60 |
| | 5 | | 98.881 | 0.011 | 0.009 | 98.901 | 82 | 54 |
| | 6 | | 98.419 | 0.003 | 0.016 | 98.438 | 22 | 96 |
| | 7 | Green (inside edge) | 98.572 | 0.012 | 0.011 | 98.595 | 89 | 66 |
| | 8 | | 98.487 | 0.002 | 0.011 | 98.500 | 15 | 66 |
| | 9 | | 98.217 | 0.006 | 0.011 | 98.234 | 45 | 66 |
| MK-053C | 1 | Medium blue | 98.543 | 0.015 | 0.012 | 98.570 | 111 | 72 |
| | 2 | | 98.439 | 0.005 | 0.011 | 98.455 | 37 | 66 |
| | 3 | | 98.185 | 0.005 | 0.008 | 98.198 | 37 | 48 |
| | 4 | Dark blue (inside edge) | 97.687 | 0.030 | 0.011 | 97.728 | 223 | 66 |
| | 5 | | 98.548 | 0.025 | 0.009 | 98.582 | 185 | 54 |
| | 6 | | 97.973 | 0.025 | 0.011 | 98.009 | 185 | 66 |
| | 7 | Green | 98.249 | 0.005 | 0.009 | 98.263 | 37 | 54 |
| | 8 | | 98.305 | 0.002 | 0.015 | 98.322 | 15 | 90 |
| | 9 | | 98.289 | 0.003 | 0.010 | 98.302 | 22 | 60 |

| | | | | | | | | |
|---|---|---|---|---|---|---|---|---|
| OZ-008 | 1 | Dark blue (beside crack) | 98.126 | 0.006 | 0.012 | 98.144 | 45 | 72 |
| | 2 | | 98.032 | 0.005 | 0.011 | 98.051 | 37 | 66 |
| | 3 | | 97.814 | 0.009 | 0.011 | 97.834 | 67 | 66 |
| | 4 | Medium blue | 98.335 | nd | 0.012 | 98.347 | nd | 72 |
| | 5 | | 98.434 | nd | 0.022 | 98.456 | nd | 132 |
| | 6 | | 98.444 | 0.000 | 0.014 | 98.458 | 0 | 84 |
| | 7 | Green | 98.394 | nd | 0.013 | 98.407 | nd | 78 |
| | 8 | | 98.344 | 0.002 | 0.008 | 98.354 | 15 | 48 |
| | 9 | | 98.162 | 0.001 | 0.016 | 98.179 | 7 | 96 |

## Appendix B. Fluid inclusion data.

| Sample | Location | Inclusion type | $T_h$ (°C) | $T_f$ (°C) | $T_m$ (°C) | Salinity (wt%) | Notes |
|---|---|---|---|---|---|---|---|
| MK-029A | Outer Wall | Primary | 480+ | - | -32.6 | 30.35 | Mostly vapour |
| | Middle | Primary | 341.8 | - | - | - | Half vapour half liquid |
| | Middle | Primary | 337.8 | - | - | - | Half vapour half liquid |
| | Middle | Primary | 325.7 | - | - | - | Half vapour half liquid |
| | Centre | Primary | 218.7 | -32.5 | -8.7 | 12.51 | Mostly liquid |
| MK-029B | Outer Wall | Primary | 420+ | - | - | - | Mostly vapour |
| | Outer Wall | Primary | 550+ | - | - | - | Mostly vapour |
| MK-033 | Outer Wall | Primary | 420+ | - | - | - | Mostly vapour |
| | Outer Wall | Primary | 480+ | - | - | - | Mostly vapour |
| MK-035A | Outer Wall | Primary | 485+ | - | - | - | Mostly vapour |
| | Outer Wall | Primary | 420+ | - | - | - | Mostly vapour |
| | Outer Wall | Primary | 420+ | - | - | - | Mostly vapour |
| | Middle | Primary | 374.2 | - | - | - | Half vapour half liquid |
| | Middle | Primary | 356.4 | - | - | - | Half vapour half liquid |
| | Middle | Primary | 349.2 | - | - | - | Half vapour half liquid |
| | Middle | Primary | 315.1 | - | - | - | Half vapour half liquid |
| | Outer Wall | Secondary | 208.7 | - | -7.1 | 10.61 | Mostly liquid |
| MK-036A | Outer Wall | Primary | 520+ | - | - | - | Mostly vapour |
| MK-036B | Outer Wall | Primary | 480+ | - | - | - | Mostly vapour |
| MK-046 | Outer Wall | Primary | 450+ | - | - | - | Mostly vapour |
| | Outer Wall | Primary | 420+ | - | - | - | Mostly vapour |
| MK-053C | Outer Wall | Primary | 520+ | - | - | - | Mostly vapour |
| | Outer Wall | Primary | 500+ | - | - | - | Mostly vapour |
| | Outer Wall | Primary | 460+ | - | - | - | Mostly vapour |
| | Outer Wall | Primary | 450+ | -42.5 | -5.9 | 9.08 | Mostly vapour |
| | Outer Wall | Primary | 450+ | -30.9 | - | - | Mostly vapour |
| | Outer Wall | Primary | 440+ | - | - | - | Mostly vapour |
| | Outer Wall | Primary | 425+ | - | - | - | Mostly vapour |
| | Outer Wall | Primary | 420+ | -40.3 | -9.9 | 13.83 | Mostly vapour |
| | Outer Wall | Primary | 420+ | - | - | - | Mostly vapour |
| | Outer Wall | Primary | 387.3 | -34.6 | -1.6 | 2.74 | Half vapour half liquid |
| | Middle | Primary | 355.8 | -34.7 | -2.2 | 3.71 | Half vapour half liquid |
| | Middle | Primary | 325.1 | - | - | - | Half vapour half liquid |
| | Middle | Primary | 248.1 | - | -2.9 | 4.80 | Mostly liquid |
| | Middle | Primary | 248.2 | - | - | - | Mostly liquid |
| | Middle | Primary | 246.1 | - | - | - | Mostly liquid |
| | Centre | Primary | 239.3 | - | - | - | Mostly liquid |
| | Centre | Primary | 222.4 | - | - | - | Mostly liquid |
| | Centre | Primary | 211.8 | - | - | - | Mostly liquid |
| | Outer Wall | Secondary | 252.9 | - | - | - | Mostly liquid |
| | Outer Wall | Secondary | 249.2 | - | - | - | Mostly liquid |

| | | | | | | | |
|---|---|---|---|---|---|---|---|
| | Outer Wall | Secondary | 234.1 | -26.8 | -6.9 | 10.36 | Mostly liquid |
| | Outer Wall | Secondary | 232.6 | - | - | - | Mostly liquid |
| | Middle | Secondary | 111.1 | -47.6 | -11.9 | 15.86 | Mostly liquid |
| | Outer Wall | Primary | 480+ | - | - | - | Mostly vapour |
| MK-070 | Outer Wall | Primary | 450+ | - | - | - | Mostly vapour |
| | Outer Wall | Primary | 420+ | - | - | - | Mostly vapour |
| | Outer Wall | Primary | 425+ | -69.8 | -22.9 | 24.27 | Mostly vapour |
| | Outer Wall | Primary | 420+ | -64.1 | -18.6 | 21.40 | Mostly vapour |
| | Outer Wall | Primary | 420+ | - | - | - | Mostly vapour |
| | Outer Wall | Primary | 389.1 | - | - | - | Half vapour half liquid |
| | Outer Wall | Primary | 388.4 | -60.3 | -21.1 | 23.11 | Half vapour half liquid |
| | Middle | Primary | 381.8 | - | - | - | Half vapour half liquid |
| | Middle | Primary | 379.8 | - | - | - | Half vapour half liquid |
| | Middle | Primary | 265.8 | -48.9 | -10.1 | 14.04 | Mostly liquid |
| OZ-008 | Centre | Primary | 221.9 | - | - | - | Mostly liquid |
| | Centre | Primary | 173.1 | - | - | - | Mostly liquid |
| | Centre | Primary | 151.8 | - | - | - | Mostly liquid |
| | Centre | Primary | 148.1 | - | - | - | Mostly liquid |
| | Centre | Primary | 124.9 | -44.8 | -9.4 | 13.29 | Mostly liquid |
| | Centre | Primary | 119.5 | -48.3 | -4.8 | 7.59 | Mostly liquid |
| | Outer Wall | Secondary | 125.7 | - | - | - | Mostly liquid |
| | Outer Wall | Secondary | 123.5 | -39.3 | - | - | Mostly liquid |
| | Middle | Secondary | 119.2 | -41.6 | - | - | Mostly liquid |
| | Middle | Secondary | 114.7 | -71.7 | - | - | Mostly liquid |
| | Outer Wall | Primary | 550+ | - | - | - | Mostly vapour |
| | Outer Wall | Primary | 450+ | - | - | - | Mostly vapour |
| | Outer Wall | Primary | 420+ | - | - | - | Mostly vapour |
| | Outer Wall | Primary | 383.6 | - | - | - | Half vapour half liquid |
| | Middle | Primary | 367.9 | - | - | - | Half vapour half liquid |
| | Middle | Primary | 348.2 | -39.9 | -3.8 | 6.16 | Half vapour half liquid |
| | Middle | Primary | 298.1 | -26.8 | -2.1 | 3.55 | Mostly liquid |
| OZ-020 | Centre | Primary | 242.5 | -30.3 | -5.5 | 8.55 | Mostly liquid |
| | Centre | Primary | 212.6 | -22.9 | -4.2 | 6.74 | Mostly liquid |
| | Centre | Primary | 145.3 | -59.9 | -15.1 | 18.72 | Mostly liquid |
| | Outer Wall | Secondary | 177.2 | - | - | - | Mostly liquid |
| | Outer Wall | Secondary | 142.2 | -72.9 | -30.1 | 28.72 | Mostly liquid |
| | Middle | Secondary | 119.5 | - | - | - | Mostly liquid |
| | Middle | Secondary | 116.1 | -56.4 | -30.7 | 29.10 | Mostly liquid |
| | Centre | Secondary | 104.5 | -42.4 | -22.2 | 23.83 | Mostly liquid |

## Appendix C. Quadrupole mass spectrometry raw data.

| Sample | Location | Crush | $H_2$ | He | $CH_4$ | $H_2O$ | $N_2$ | $O_2$ | Ar | $CO_2$ | Mols Gas |
|---|---|---|---|---|---|---|---|---|---|---|---|
| WCIS-14-MK-029A | Kamiskutanikaw | 1 | 0.00 | 1.68E-04 | 0.09 | 91.07 | 7.11 | 1.12 | 0.08 | 0.53 | 3.43E-11 |
| | | 2 | 0.00 | 3.85E-05 | 0.03 | 90.51 | 7.43 | 1.80 | 0.09 | 0.14 | 1.02E-10 |
| | | 3 | 0.00 | 3.08E-04 | 0.33 | 93.38 | 4.75 | 0.82 | 0.05 | 0.68 | 3.14E-11 |
| | | 4 | 0.00 | 5.56E-05 | 0.02 | 91.09 | 7.75 | 1.01 | 0.05 | 0.08 | 7.51E-11 |
| WCIS-14-MK-029B | Kamiskutanikaw | 1 | 0.00 | 1.39E-04 | 0.37 | 86.88 | 9.03 | 1.49 | 0.08 | 2.15 | 2.01E-10 |
| | | 2 | 0.00 | 5.40E-05 | 0.27 | 91.92 | 3.86 | 0.09 | 0.03 | 3.83 | 5.18E-11 |
| | | 3 | 0.00 | 0.00 | 0.34 | 95.73 | 1.78 | 0.08 | 0.01 | 2.06 | 5.27E-12 |
| | | 4 | 0.00 | 1.95E-04 | 0.34 | 96.08 | 1.37 | 0.15 | 0.01 | 2.05 | 9.32E-12 |
| WCIS-14-MK-033 | Kamiskutanikaw | 1 | 0.20 | 1.77E-04 | 0.21 | 88.47 | 5.46 | 0.95 | 0.09 | 4.61 | 1.63E-12 |
| | | 2 | 0.01 | 6.20E-05 | 0.07 | 93.56 | 5.33 | 0.76 | 0.06 | 0.22 | 2.11E-11 |
| | | 3 | 0.44 | 3.01E-04 | 0.30 | 94.78 | 2.92 | 0.43 | 0.07 | 1.07 | 2.19E-12 |
| | | 4 | 0.57 | 0.00 | 0.27 | 95.17 | 2.80 | 0.43 | 0.04 | 0.73 | 8.01E-12 |
| WCIS-14-MK-035A | Kamiskutanikaw | 1 | 0.05 | 3.16E-05 | 0.08 | 95.88 | 2.26 | 0.46 | 0.04 | 1.24 | 8.78E-12 |
| | | 2 | 0.11 | 2.22E-05 | 0.05 | 95.92 | 0.79 | 0.10 | 0.01 | 3.02 | 5.30E-12 |
| | | 3 | 0.21 | 0.00 | 0.12 | 93.36 | 1.81 | 0.33 | 0.02 | 4.15 | 4.07E-12 |
| | | 4 | 0.13 | 2.21E-04 | 0.03 | 96.97 | 0.59 | 0.12 | 0.02 | 2.14 | 4.94E-12 |
| | | 5 | 0.20 | 1.41E-04 | 0.25 | 97.61 | 0.34 | 0.07 | 0.01 | 1.52 | 3.89E-12 |
| WCIS-14-MK-036A | Kamiskutanikaw | 1 | 0.00 | 4.03E-05 | 0.02 | 91.16 | 8.25 | 0.45 | 0.02 | 0.09 | 1.18E-10 |
| | | 2 | 0.00 | 3.48E-05 | 0.05 | 92.32 | 6.12 | 0.95 | 0.06 | 0.51 | 2.52E-11 |
| | | 3 | 0.00 | 2.35E-05 | 0.01 | 90.77 | 7.32 | 1.67 | 0.07 | 0.16 | 1.30E-10 |
| | | 4 | 0.00 | 1.33E-04 | 0.04 | 91.63 | 6.71 | 1.16 | 0.06 | 0.40 | 5.57E-11 |
| | | 5 | 0.00 | 0.00 | 0.14 | 90.37 | 7.77 | 0.89 | 0.08 | 0.75 | 2.55E-11 |
| | | 6 | 0.00 | 2.70E-04 | 0.14 | 91.88 | 6.01 | 0.88 | 0.06 | 1.02 | 2.27E-11 |
| | | 7 | 0.00 | 1.52E-04 | 0.04 | 91.50 | 6.98 | 1.16 | 0.06 | 0.26 | 6.23E-11 |
| | | 8 | 0.00 | 9.57E-05 | 0.18 | 92.17 | 5.33 | 0.83 | 0.06 | 1.44 | 1.52E-11 |

| | | | | | | | | | | | |
|---|---|---|---|---|---|---|---|---|---|---|---|
| WCIS-14-MK-036B | Kamiskutanikaw | 1 | 0.00 | 0.00 | 0.39 | 82.70 | 12.65 | 2.55 | 0.24 | 1.48 | 1.27E-11 |
| | | 2 | 0.00 | 2.35E-03 | 0.77 | 86.36 | 10.99 | 0.70 | 0.07 | 1.11 | 3.15E-12 |
| | | 3 | 0.00 | 3.86E-04 | 0.20 | 87.27 | 8.70 | 3.23 | 0.09 | 0.51 | 1.09E-11 |
| | | 4 | 0.00 | 8.82E-05 | 0.20 | 91.95 | 4.99 | 2.60 | 0.04 | 0.22 | 4.77E-11 |
| WCIS-14-MK-046 | South East Island | 1 | 0.00 | 6.04E-04 | 0.58 | 87.65 | 4.75 | 0.01 | 0.09 | 6.92 | 2.60E-12 |
| | | 2 | 0.00 | 0.00 | 0.55 | 89.64 | 6.23 | 0.74 | 0.06 | 2.79 | 5.08E-12 |
| | | 3 | 0.00 | 1.91E-03 | 0.64 | 89.11 | 5.52 | 0.59 | 0.08 | 4.06 | 3.14E-12 |
| | | 4 | 0.00 | 0.00 | 0.52 | 91.14 | 5.60 | 0.69 | 0.06 | 2.00 | 2.04E-12 |
| | | 5 | 0.00 | 0.00 | 0.77 | 88.98 | 4.59 | 0.79 | 0.05 | 4.82 | 7.30E-12 |
| | | 6 | 0.00 | 0.00 | 1.53 | 88.45 | 5.97 | 1.26 | 0.07 | 2.71 | 2.05E-12 |
| | | 7 | 0.00 | 0.00 | 0.97 | 85.94 | 8.73 | 1.97 | 0.07 | 2.32 | 5.80E-12 |
| WCIS-14-MK-053C | South East Island | 1 | 0.00 | 1.69E-03 | 0.55 | 94.68 | 3.42 | 0.34 | 0.03 | 0.98 | 1.14E-11 |
| | | 2 | 0.00 | 6.58E-04 | 0.38 | 91.73 | 5.47 | 0.70 | 0.05 | 1.67 | 9.71E-12 |
| | | 3 | 0.00 | 2.95E-04 | 0.09 | 92.58 | 5.57 | 0.68 | 0.05 | 1.03 | 2.63E-11 |
| | | 4 | 0.00 | 2.01E-03 | 0.66 | 92.71 | 4.38 | 0.35 | 0.02 | 1.87 | 7.18E-12 |
| | | 5 | 0.00 | 9.60E-04 | 0.94 | 95.82 | 1.09 | 0.09 | 0.01 | 2.05 | 9.85E-12 |
| | | 6 | 0.00 | 2.96E-04 | 0.23 | 96.67 | 2.20 | 0.24 | 0.02 | 0.65 | 5.02E-12 |
| WCIS-14-MK-070 | Lepage | 1 | 0.00 | 2.07E-04 | 0.05 | 91.02 | 7.36 | 1.00 | 0.06 | 0.51 | 1.05E-10 |
| | | 2 | 0.00 | 5.91E-04 | 0.18 | 92.40 | 5.71 | 0.64 | 0.05 | 1.02 | 9.09E-12 |
| | | 3 | 0.00 | 1.75E-04 | 0.05 | 91.65 | 7.31 | 0.75 | 0.07 | 0.16 | 5.53E-11 |
| | | 4 | 0.00 | 5.94E-06 | 0.02 | 91.43 | 7.46 | 0.82 | 0.08 | 0.20 | 5.55E-11 |
| | | 5 | 0.00 | 1.08E-04 | 0.66 | 89.66 | 5.89 | 0.31 | 0.05 | 3.43 | 1.82E-11 |
| | | 6 | 0.00 | 7.75E-04 | 1.46 | 87.58 | 6.03 | 0.16 | 0.00 | 4.77 | 1.48E-12 |
| | | 7 | 0.00 | 0.00 | 3.14 | 88.22 | 5.05 | 0.24 | 0.05 | 3.31 | 5.20E-12 |

| | | | | | | | | | | |
|---|---|---|---|---|---|---|---|---|---|---|
| | | 1 | 0.00 | 1.09E-03 | 0.52 | 91.37 | 5.27 | 0.96 | 0.05 | 1.81 | 3.26E-12 |
| | | 2 | 0.00 | 7.67E-04 | 0.75 | 92.34 | 3.39 | 0.25 | 0.02 | 3.25 | 2.39E-12 |
| | | 3 | 0.00 | 3.53E-04 | 1.09 | 86.04 | 7.14 | 0.49 | 0.07 | 5.18 | 5.49E-12 |
| WCIS-14-OZ-008 | Tadpole | 4 | 0.00 | 4.66E-04 | 0.57 | 85.08 | 11.79 | 2.03 | 0.12 | 0.40 | 1.15E-11 |
| | | 5 | 0.00 | 6.86E-03 | 0.37 | 90.43 | 7.37 | 0.39 | 0.04 | 1.38 | 3.59E-12 |
| | | 6 | 0.00 | 7.22E-02 | 9.99 | 0.00 | 71.76 | 8.29 | 0.87 | 9.01 | 5.69E-12 |
| | | 7 | 0.00 | 1.29E-03 | 0.31 | 93.03 | 3.85 | 0.02 | 0.03 | 2.75 | 1.65E-12 |
| | | 1 | 0.00 | 0.00 | 0.06 | 97.57 | 1.61 | 0.40 | 0.02 | 0.35 | 1.85E-11 |
| | | 2 | 0.00 | 2.15E-05 | 0.14 | 95.74 | 2.20 | 0.36 | 0.03 | 1.53 | 2.71E-11 |
| | | 3 | 0.00 | 4.39E-05 | 0.07 | 97.31 | 1.41 | 0.43 | 0.01 | 0.76 | 2.23E-11 |
| WCIS-14-OZ-020 | Lepage | 4 | 0.00 | 3.67E-05 | 0.03 | 97.31 | 1.24 | 0.63 | 0.01 | 0.78 | 3.54E-11 |
| | | 5 | 0.00 | 7.09E-05 | 0.08 | 98.20 | 0.83 | 0.15 | 0.01 | 0.74 | 1.72E-11 |
| | | 6 | 0.00 | 6.22E-05 | 0.13 | 97.55 | 1.07 | 0.14 | 0.01 | 1.10 | 3.61E-11 |
| | | 7 | 0.00 | 2.15E-04 | 0.35 | 96.05 | 1.12 | 0.20 | 0.01 | 2.27 | 5.44E-12 |

## Appendix D. Mass spectrometry ratios.

| Sample | Location | Crush | $N_2$/Ar | $N_2/O_2$ | $O_2$/Ar | $CO_2/CH_4$ | Ar/He |
|---|---|---|---|---|---|---|---|
| WCIS-14-MK-029A | Kamiskutanikaw | 1 | 89.75 | 6.34 | 14.16 | 5.81 | 472.75 |
| | | 2 | 79.72 | 4.13 | 19.31 | 4.50 | 2419.57 |
| | | 3 | 97.61 | 5.82 | 16.78 | 2.05 | 158.02 |
| | | 4 | 169.04 | 7.66 | 22.08 | 3.70 | 824.80 |
| WCIS-14-MK-029B | Kamiskutanikaw | 1 | 116.29 | 6.06 | 19.19 | 5.88 | 558.89 |
| | | 2 | 133.03 | 42.56 | 3.13 | 14.13 | 536.91 |
| | | 3 | 331.06 | 21.64 | 15.30 | 6.07 | - |
| | | 4 | 136.38 | 9.21 | 14.81 | 6.09 | 51.45 |
| WCIS-14-MK-033 | Kamiskutanikaw | 1 | 60.35 | 5.76 | 10.47 | 21.98 | 510.36 |
| | | 2 | 90.89 | 7.06 | 12.88 | 2.93 | 945.73 |
| | | 3 | 44.72 | 6.79 | 6.59 | 3.55 | 217.13 |
| | | 4 | 77.22 | 6.59 | 11.72 | 2.70 | - |
| WCIS-14-MK-035A | Kamiskutanikaw | 1 | 57.58 | 4.91 | 11.73 | 15.73 | 1240.41 |
| | | 2 | 58.98 | 8.08 | 7.29 | 62.80 | 601.41 |
| | | 3 | 93.79 | 5.56 | 16.86 | 33.28 | - |
| | | 4 | 32.36 | 4.82 | 6.71 | 63.22 | 82.14 |
| | | 5 | 51.07 | 4.89 | 10.44 | 6.10 | 47.72 |
| WCIS-14-MK-036A | Kamiskutanikaw | 1 | 336.83 | 18.29 | 18.42 | 4.73 | 608.13 |
| | | 2 | 105.96 | 6.45 | 16.43 | 10.84 | 1660.77 |
| | | 3 | 106.60 | 4.39 | 24.30 | 13.62 | 2917.93 |
| | | 4 | 107.79 | 5.80 | 18.57 | 9.16 | 468.28 |
| | | 5 | 95.46 | 8.71 | 10.96 | 5.30 | - |
| | | 6 | 92.69 | 6.83 | 13.58 | 7.43 | 240.20 |
| | | 7 | 110.63 | 6.02 | 18.39 | 7.40 | 414.50 |
| | | 8 | 88.86 | 6.44 | 13.79 | 8.14 | 626.89 |
| WCIS-14-MK-036B | Kamiskutanikaw | 1 | 51.89 | 4.96 | 10.45 | 3.83 | - |
| | | 2 | 166.88 | 15.68 | 10.64 | 1.45 | 28.07 |
| | | 3 | 97.01 | 2.70 | 35.99 | 2.51 | 232.13 |
| | | 4 | 115.36 | 1.92 | 60.11 | 1.07 | 490.36 |
| WCIS-14-MK-046 | South East Island | 1 | 52.54 | 676.96 | 0.08 | 11.84 | 149.84 |
| | | 2 | 106.22 | 8.39 | 12.66 | 5.08 | - |
| | | 3 | 68.11 | 9.40 | 7.24 | 6.33 | 42.34 |
| | | 4 | 101.02 | 8.15 | 12.39 | 3.86 | - |
| | | 5 | 83.68 | 5.82 | 14.37 | 6.24 | - |
| | | 6 | 87.12 | 4.73 | 18.44 | 1.77 | - |
| | | 7 | 120.61 | 4.44 | 27.19 | 2.39 | - |

| | | | | | | | |
|---|---|---|---|---|---|---|---|
| WCIS-14-MK-053C | South East Island | 1 | 105.59 | 10.18 | 10.37 | 1.80 | 19.19 |
| | | 2 | 117.80 | 7.83 | 15.05 | 4.44 | 70.55 |
| | | 3 | 110.50 | 8.14 | 13.58 | 10.97 | 170.84 |
| | | 4 | 225.58 | 12.44 | 18.14 | 2.84 | 9.68 |
| | | 5 | 92.56 | 11.63 | 7.96 | 2.18 | 12.23 |
| | | 6 | 110.15 | 9.11 | 12.09 | 2.84 | 67.27 |
| WCIS-14-MK-070 | Lepage | 1 | 120.33 | 7.38 | 16.30 | 9.68 | 295.89 |
| | | 2 | 107.87 | 8.89 | 12.13 | 5.53 | 89.50 |
| | | 3 | 111.59 | 9.68 | 11.52 | 3.18 | 375.42 |
| | | 4 | 95.31 | 9.11 | 10.46 | 11.32 | 13170.33 |
| | | 5 | 130.20 | 18.86 | 6.90 | 5.16 | 418.36 |
| | | 6 | - | 37.92 | - | 3.27 | 0.00 |
| | | 7 | 110.44 | 21.01 | 5.26 | 1.05 | - |
| WCIS-14-OZ-008 | Tadpole | 1 | 101.59 | 5.47 | 18.57 | 3.45 | 47.75 |
| | | 2 | 146.93 | 13.41 | 10.95 | 4.35 | 30.04 |
| | | 3 | 104.99 | 14.62 | 7.18 | 4.74 | 192.65 |
| | | 4 | 98.70 | 5.80 | 17.02 | 0.70 | 256.37 |
| | | 5 | 180.59 | 18.75 | 9.63 | 3.71 | 5.95 |
| | | 6 | 82.19 | 8.65 | 9.50 | 0.90 | 12.09 |
| | | 7 | 123.13 | 165.10 | 0.75 | 8.88 | 24.26 |
| WCIS-14-OZ-020 | Lepage | 1 | 79.79 | 4.04 | 19.75 | 6.19 | - |
| | | 2 | 83.56 | 6.09 | 13.73 | 10.89 | 1226.60 |
| | | 3 | 101.58 | 3.26 | 31.16 | 11.08 | 317.03 |
| | | 4 | 96.33 | 1.98 | 48.57 | 23.61 | 351.57 |
| | | 5 | 81.15 | 5.68 | 14.29 | 9.78 | 143.65 |
| | | 6 | 121.55 | 7.53 | 16.14 | 8.30 | 141.70 |
| | | 7 | 93.45 | 5.76 | 16.22 | 6.51 | 55.92 |

# Curriculum Vitae

**Name:** Daliah Raquel Bibas

**Post-secondary Education and Degrees:**

M.Sc. Geology & Planetary Sciences
The University of Western Ontario
London, Ontario, Canada
2021-2023

B.Sc. Medical Sciences & Biology
The University of Western Ontario
London, Ontario, Canada
2017-2021

**Honours and Awards:**

David J. Stenason Global Opportunities Award
The University of Western Ontario
2022

Graduate Fellowship
The University of Western Ontario
2021-2023

Western Graduate Research Scholarship
Earth Sciences / Faculty of Science, UWO
2021-2023

FAST ISXRD Summer Scholarship
Canadian Space Agency
2021

**Related Work Experience**

Teaching Assistant
The University of Western Ontario
2021-2023

Research Intern
Institute for Earth and Space Exploration, UWO
2021

**Publications:**

Flemming, R., L., Sabarinathan, J., Pilles, E. A., Veinberg, S. L., McCausland, P. J. A., McIsaac, K. A., Osinski, G. R., Tornabene, L. L., Schmidt, M. E., Gellert, R., McCraig, M. A., Armstrong, D. O. B., Beaton, D. M., **Bibas, D. R.**, Cao, F., Li, Y., Ryan, C. H., Svensson, M. J. O., & Schmidt, G. (2021). In Situ X-ray Diffraction (ISXRD) for Exploring Mineralogy and Geology on Mars. Geological Association of Canada – Mineralogical Association of Canada, Abstract Volume, v. 44, p. 93